

Chemical Waves in Modified Membranes

Dissertation

zur Erlangung des Doktorgrades
der Naturwissenschaften
(Dr. rer. nat.)

dem
Fachbereich Physikalische Chemie
der Philipps-Universität Marburg
vorgelegt von

Attila Lázár
aus Győr, Ungarn

Marburg/Lahn 1997

Vom Fachbereich Physikalische Chemie der Philipps-Universität Marburg

als Dissertation am

02.05.1997 angenommen.

Erstgutachter:

Prof. Dr. H.-D. Försterling

Zweitgutachter:

Prof. Dr. A. Schweig

Tag der mündlichen Prüfung am:

27.05.1997

Contents

CONTENTS	1
1. INTRODUCTION	3
2. OSCILLATIONS AND CHEMICAL WAVES	4
2.1. Equilibrium and steady state	4
2.2. The first oscillating model.....	5
2.3. The Brusselator model [21].....	6
2.4. The Belousov-Zhabotinsky reaction and the Oregonator model	6
2.5. Steady states, oscillations and excitability	8
2.6. Excitable medium and chemical waves.....	10
2.7. Properties of chemical waves	11
2.8. Reactor types.....	13
2.9. Turing patterns	13
3. SHORT HISTORY OF CHEMICAL WAVE EXPERIMENTS	15
4. EXPERIMENTAL	17
4.1. Immobilization of catalysts on membrane surfaces.....	17
4.1.1. Fixation of ferroin on cellulose nitrate membranes	17
4.1.2. Fixation of bathoferroin on polysulfone membranes	17
4.2. Creating different geometries.....	18
4.2.1. Cutting the membranes	18
4.2.2. Catalyst patterns painted on polysulfon membranes	18
4.3. Preparation of the BZ solution.....	18
4.4. Gelation of membranes and filter papers.....	19
4.5. Creating membrane zones with reduced wave velocity.....	19
4.6. Reactors.....	20
4.6.1. The Petri dish reactor.....	20
4.6.2. A real continuously fed membrane reactor	21
4.7. The experimental setup.....	22
4.8. Starting an experiment	23
4.8.1. Starting chemical waves.....	23
4.8.2. Creating a chemical pinwheel	23
4.8.3. Loading the reactor.....	23
5. RESULTS AND DISCUSSION	25
5.1. Composition of the BZ solution.....	25
5.2. Comparison of different catalyst-membrane systems	27
5.3. The geometry of chemical waves in homogeneous medium.....	28
5.3.1. A simple model of wave propagation	28
5.3.2. A special case: involute of a circle.....	29
5.3.3. Results.....	31
5.4. Refraction of chemical waves.....	32

5.4.1.	Comparing two methods leading to local inhomogeneities	33
5.4.2.	Wave refraction with BaSO ₄ precipitate	34
5.4.3.	Refraction of waves with a plastic foil barrier.....	35
5.4.4.	Considerations and observations suggesting that KTTC is an intermediate	36
5.4.5.	Acceleration of waves due to water evaporation	37
5.4.6.	Refraction with Nuclepore barrier membranes	37
5.4.7.	Wave refraction in an oxygen-free environment.....	38
5.4.8.	Studies on chemical lenses.....	39
5.5.	The geometry of chemical waves in nonuniform membrane rings	44
5.5.1.	Generalization of the Wiener-Rosenblueth theory	44
	Homogeneous case	44
	Inhomogeneous case, $\omega_1 < \omega_2$ ($v_1 \ll v_2$)	45
	Inhomogeneous case, $\omega_1 > \omega_2$ ($v_1 < v_2$)	46
5.5.2.	Experimental verification of the generalized Wiener-Rosenblueth theory	47
5.5.3.	Connection between front shape and wave velocity	51
6.	RECONSTRUCTING THE VELOCITY MAP	53
6.1.	Capturing images	54
6.2.	Subtraction and contrast enhancement of images.....	54
6.3.	Wave front determination.....	55
6.3.1.	Calculation of graylevels for points with floating point coordinates.....	55
6.3.2.	Preliminary conditions of wave front calculation.....	56
6.3.3.	Describing the wave front	56
6.4.	Calculation of the velocity	59
6.4.1.	The distance based method	59
6.4.2.	The geometry based method.....	59
6.5.	Visualization of the velocity map	60
6.6.	A simple method to enhance the resolution of the velocity maps.....	61
7.	SIMULATION OF CHEMICAL WAVES	62
7.1.	Why cellular automaton model?	63
7.2.	Calculating the reaction term	63
7.3.	Calculating the diffusion term	63
7.4.	Borders and walls.....	67
7.5.	Results	67
SUMMARY		72
ZUSAMMENFASSUNG		74
APPENDIX		76
Appendix A.	Program Reference Pages of WANA.....	76
Appendix B.	Program Reference Pages of WASI.....	79
Appendix C.	Phase-plane model used in the simulations.....	81
Appendix D.	The C-shell script used for capturing images.....	82
BIBLIOGRAPHY		84
Own Publications.....		87
ACKNOWLEDGMENTS		88

1. Introduction

Pattern formation became one of the most extensively studied phenomena within the field of nonlinear dynamics in the last decades. Different levels of spatial self organization can be observed in biology [1,2] and chemistry [3,4,5]. These include aggregating cells in the slime mold *Dictyostelium discoideum* [6,7], spreading of calcium waves in the cytoplasm of *Xenopus* oocytes frog embryo [8], spreading depression in chicken retina [9] or circular and spiral waves appearing in the heart muscle [10]. There are also many chemical reactions showing similar phenomena. These reactions can be investigated easier than their biological counterparts, and can play the role of a general model for describing the pattern formation.

Homogeneous asymptotic states of exotic reactions have been studied in open tank reactors (CSTR, Continuously fed Stirred Tank Reactor). No spatial patterns can be observed in CSTRs, however. To study heterogeneous asymptotic states open spatial reactors, so called CFURs (Continuously Fed Unstirred Reactor [11,12,13]) should be applied. Recently, membrane techniques were introduced. The main advantages of the these techniques are: (a) disturbing effects (convection and bubble formation that were an every day problem in early experiments) can be avoided; (b) the consumption of reagents is very small, this increases the lifetime of wave experiments significantly. (c) furthermore, membranes are very suitable for creating different geometries of excitable media.

One of the most studied and best understood oscillating reactions is the Belousov-Zhabotinsky reaction [3,14,15], that was used as a model reaction in all our experiments. Not only the chemical reaction but also the transport properties of the oscillating medium can influence the shape of the developing structures. Most of the excitable media are not uniform. For example, in recent models of atrial flutter [16,17] it is assumed that the obstacle is a “combined functional-anatomical conduction block” which is surrounded by a region where the wave propagation is slower than in other parts of the atrium. We tried to build a corresponding chemical “conduction block” for modeling the heart.

The experiments were carried out by using a computer-video system to record the patterns, to evaluate the data and to calculate a velocity map describing the propagation properties of the medium. A generalized mathematical theory was developed to predict the shape of wave fronts.

2. Oscillations and Chemical Waves

2.1. *Equilibrium and steady state*

It is known that in a process leading to equilibrium the concentrations of the initial components (reactants) is decreasing, and the concentration of products is increasing until they reach a well defined state: the equilibrium. This process is followed by a decrease of the free enthalpy at constant pressure and temperature, until it reaches a minimum in the equilibrium. Because of the Second Law of Thermodynamics it isn't possible to imagine oscillations around the equilibrium, so a cyclic process like "reactants → products → reactants" does not exist¹. The symmetry of such a system is very high, as in asymptotic state all variables have a constant value independent of time and space (Figure 1).

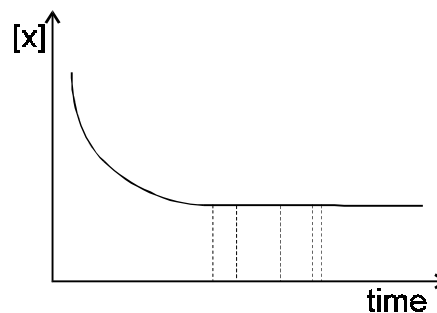


Figure 1. Equilibrium

When the asymptotic state is an equilibrium there is no change in $[x]$ if the time is shifted by an arbitrary value.

The steady state is somewhat different. Maintaining the concentrations of reactants and products on a steady level it is possible to prevent the system reaching the equilibrium. Normally this is done by supplying fresh reactants and removing the products. In the respect of mass transport this system is open. In most cases the system achieves a stable state, and the concentrations of all intermediates tend to an appropriate steady value by monotone changes or through some monotone decreasing amplitudes.

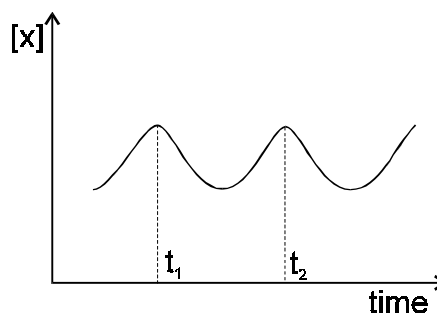


Figure 2. Oscillations in an unstable steady state

When the asymptotic state is an oscillation, there is a periodic change in $[x]$, the time can be only shifted with the periodic time ($t_2 - t_1$) to reach the same value of $[x]$. $[x]$ refers to any periodically changing properties of the system: concentrations, temperature, pressure, redox potential, etc.

However, this behavior is not the only possible one. If the steady state is unstable, there may be also explosive or oscillating reactions. In the first case the concentration of one or more products increases very rapidly and tends to infinity. In the case of oscillations the

¹ "In the early 1950s B.P. Belousov, a Soviet biophysicist, was searching for an inorganic analogue of the biochemical Krebs cycle when he noticed that the color of a mixture consisting of bromate and cerium ions with citric acid in sulfuric acid oscillated back and forth, between colorless and pale yellow. Belousov carefully characterized the phenomenon and submitted his results, with recipes included, to a number of journals. All journals rejected his paper on the grounds that such a thing could not occur. The vast majority of chemists felt that chemical oscillation constituted a violation of the Second Law of Thermodynamics, a sort of perpetual motion machine in a beaker." [18,19] (It might be also noted that chemical engineers and combustion scientists who didn't know that chemists 'knew' that oscillations were impossible had been happily making considerable progress in this area since 1945.) [4]

concentration of a component reaches the same value from time to time. This is a symmetry breaking in time compared to the time independent homogeneous steady state (Figure 2).

2.2. The first oscillating model

What can cause instability in a chemical system? It can be a positive feedback for instance. This positive feedback can be, for example, an autocatalytic reaction. However, autocatalysis can lead to explosion, so an inhibition step is also necessary. If the autocatalysis and the inhibition appear at the same time, the steady state can be stabilized. Oscillations can only appear if the inhibition step is somehow delayed.

The first mathematical model of chemical oscillations was created by Lotka, an American chemist-mathematician in 1920 [20] and, independently, by Volterra, an Italian mathematician (1932). Lotka made a model for chemical reactions, but Volterra made a model for phenomena found in population dynamics². As an example, the Lotka-Volterra model describes the population changes of foxes and rabbits:



The ‘concentration’ A refers to the grass, X refers to the rabbits, Y refers to the foxes and B refers to the dead foxes. This simple model is based on two autocatalytic steps. The Lotka-

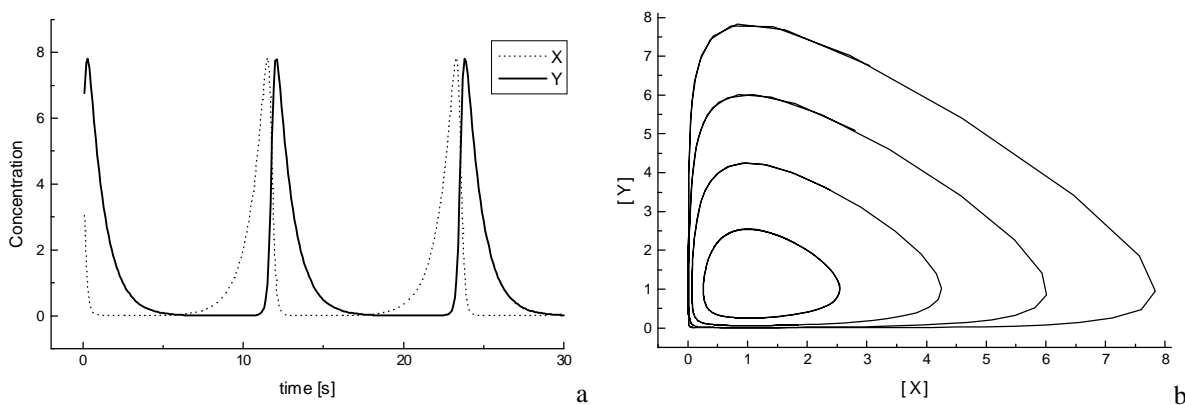


Figure 3. The Lotka-Volterra model³

Plots (a) concentrations against time; (b) one concentration against the other.

Volterra equations can be solved numerically, and the results can be depicted in two ways (Figure 3). One way is to plot $[X]$ and $[Y]$ versus time or by plotting one concentration versus the other one (phase-plane representation). The system describes closed orbits in the Lotka-Volterra model. Different orbits are obtained with different starting conditions. It is also to be noted here, that until now there is no chemical reaction which can be described by the Lotka-Volterra model.

² Volterra’s father-in-law was a marine-biologist, who noticed a periodical change in the populations of small and big fishes in the Adriatic Sea.

³ Curves were calculated by András Volford with the initial values of $A=1$; $k=1$.

2.3. The Brusselator model [21]

Another interesting set of equations is called the Brusselator⁴:



Because the reactants (A and B) are maintained at constant concentrations, the two variables are the concentrations of X and Y . These two concentrations can be calculated by solving the rate equations numerically. Figure 4 shows the phase-plane of this model. The interesting feature is that, whatever the initial concentrations of X and Y are, the system settles down into the same periodic variation of concentrations. The common trajectory to which the system migrates is called a limit cycle.

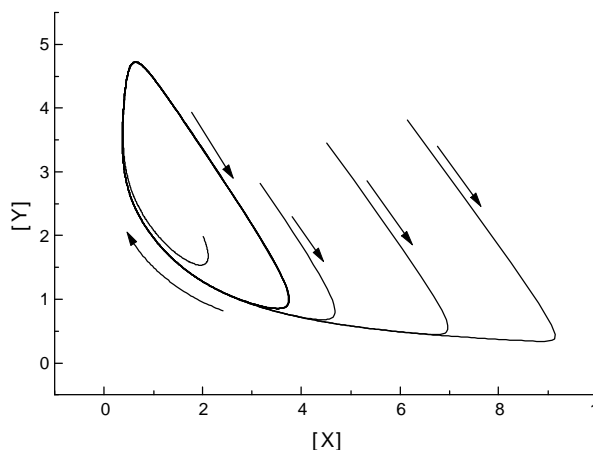
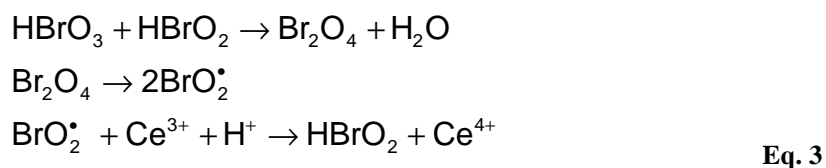


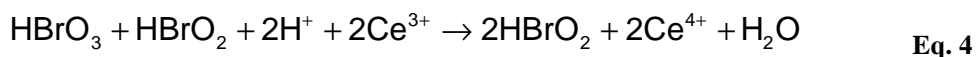
Figure 4. The limit cycle of the Brusselator⁵

2.4. The Belousov-Zhabotinsky reaction and the Oregonator model

Probably the Belousov-Zhabotinsky⁶ (BZ) reaction [3,14,15] is the most studied oscillation reaction, however, not all the reaction details are known yet. The mechanism consists of two feedback loops. The positive feedback loop (autocatalytic cycle) is already known:



So, one HBrO_2 forms two BrO_2^\bullet radicals. If each of these produce an HBrO_2 molecule we have the overall stoichiometry:

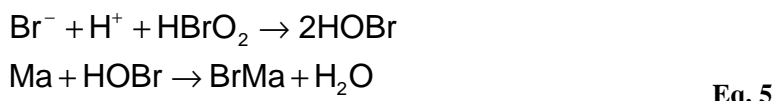


The negative feedback loop is not so well known, there are still discussions about its mechanism. First it was thought that the only controlling intermediate is the bromide ion:

⁴ Because it is an oscillator proposed by Ilya Prigogine's group in Brussels. The name was given by J.J. Tyson.

⁵ Curves were calculated by András Volford with the initial values of $A=1$; $B=3$; $k=1$.

⁶ "Belousov's recipes circulated among Moscow laboratories, and a young graduate student, Anatol Zhabotinsky, began to study and refine the reaction. Zhabotinsky modified the reagents, discovering that malonic acid could replace citric acid and that the redox indicator ferroin gave a more dramatic red-blue color change than the cerous-ceric couple." [18]



where Ma is malonic acid, and BrMa is bromomalonic acid. The



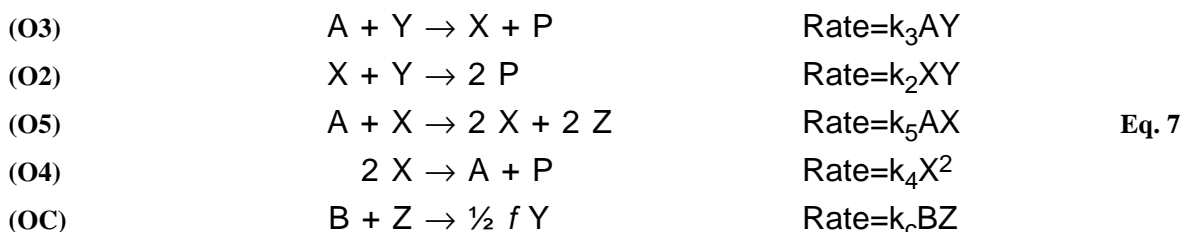
reaction was considered as a source for the bromide ion, but even the mechanism of this step is still not clear. However, there is also another inhibition step. The BrO_2^\bullet formed in the autocatalytic step can react with any organic radical compound, with the malonyl radical R^\bullet for instance, which forms in the following reaction:



All that means, that there are two different negative feedback loops:

- through bromide ion: OREGONATOR model [22],
- through a radical intermediate: RADICALATOR model [23,24].

The Oregonator model is a skeletonned version of the so called Field Körös Noyes (FKN) [25] mechanism of the BZ-reaction created by Field and Noyes at the University of Oregon. It contains an autocatalytic process, a negative feedback step and three intermediate species (the notation of [4] is used):



where $A=\text{BrO}_3^-$, $Y=\text{Br}^-$, $X=\text{HBrO}_2$, $Z=\text{Ce}^{4+}$, $P=\text{HOBr}$, B =all oxidizable organic species, and f is a stoichiometric factor. The reaction rate equations for the intermediate species X, Y, Z are:

$$\begin{aligned} \frac{dX}{dt} &= k_3AY - k_2XY + k_5AX - 2k_4X^2 \\ \frac{dY}{dt} &= -k_3AY - k_2XY + \frac{1}{2}fk_cBZ \\ \frac{dZ}{dt} &= 2k_5AX - k_cBZ \end{aligned} \quad \text{Eq. 8}$$

Let's transform the concentrations X, Y, Z to dimensionless variables by defining x, y, z and τ as:

$$x = 2k_4X/k_5A, \quad y = k_2Y/k_5A, \quad z = k_c k_4 BZ / (k_5A)^2 \quad \text{and} \quad \tau = k_c B t \quad \text{Eq. 9}$$

The advantage of this substitution is that the rate equations now become the form:

$$\frac{dx}{d\tau} = \frac{qy - xy + x(1-x)}{\varepsilon} \quad \text{Eq. 10}$$

$$\frac{dy}{d\tau} = \frac{-qy - xy + fx}{\varepsilon'} \quad \text{Eq. 11}$$

$$\frac{dz}{d\tau} = x - z \quad \text{Eq. 12}$$

where the dimensionless parameters are:

$$\varepsilon = k_c B / k_5 A, \quad \varepsilon' = 2k_c k_4 B / k_2 k_5 A, \quad \text{and} \quad q = 2k_3 k_4 / k_2 k_5 \quad \text{Eq. 13}$$

For typical values of $A=0.06\text{M}$ and $B=0.02\text{M}$, we have

$$\varepsilon = 10^{-2}, \quad \varepsilon' = 2.5 \times 10^{-5}, \quad q = 9 \times 10^{-5}$$

Because ε' is so small, the concentration of bromide ion y will change quickly in time ($dy/d\tau$ will be large) unless the numerator in Eq. 11 is also small. This argument is a mathematically-based statement of the classical steady-state approximation. Thus we now assume:

$$y = \frac{fz}{q + x} \quad \text{Eq. 14}$$

at all times: the bromide concentration is in a dynamic steady state relative to the HBrO_2 concentration. Substituting this result into the reaction rate equations, we have

$$\varepsilon \frac{dx}{d\tau} = x(1-x) - \frac{(x-q)fz}{q+x} \quad \text{Eq. 15}$$

$$\frac{dz}{d\tau} = x - z \quad \text{Eq. 16}$$

The two terms in Eq. 15 represent Process B (Eq. 7-O4,O5 autocatalysis, limited by the disproportionation step) and Process A (Eq. 7-O2,O3 production and removal of HBrO_2) respectively, while the two terms in Eq. 16 describe the production of Ce^{4+} in Process B and its reduction in Process C (Eq. 7-OC).

2.5. *Steady states, oscillations and excitability*

Eq. 15 and Eq. 16 can be integrated numerically for any given value of f . A more pictorial method is to solve these equations graphically using the phase plane of the system. There are two special curves on the phase plane as shown in Figure 5. These are the nullclines that connect x, z pairs for which $dx/d\tau = 0$ (the x -nullcline) or $dz/d\tau = 0$ (the z -nullcline). From Eq. 16 it follows that the z -nullcline is a straight line $x=z$ starting from the origin with unit slope. Any trajectory crossing this line has a maximum or minimum in z at that point. According to Eq. 15 the x -nullcline is more complex:

$$z = \frac{(1-x)(q+x)x}{f(x-q)} \quad \text{Eq. 17}$$

The intersection of the two nullclines is the steady state of the system. The two nullclines divide the phase plane into four regions in which $dx/d\tau$ and $dz/d\tau$ change their sign,

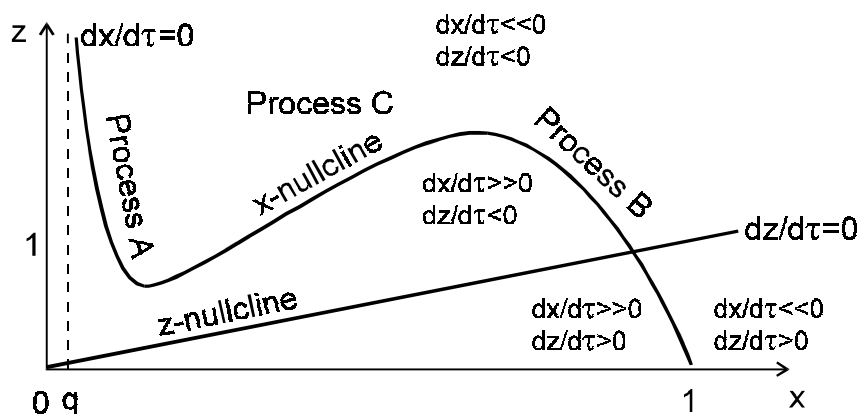


Figure 5. Phase plane of the Oregonator. $f=1/4$

indicating the slope of the trajectory in that region. Starting from an arbitrary initial point of (x_0, z_0) the subsequent evolution can be predicted by the following arguments:

- The point doesn't lie on the x -nullcline, the right-hand side of Eq. 15 will be nonzero.
 - If the point is below the x -nullcline, $dx/d\tau$ will be positive, and because of the small value of ε , it will be large in magnitude. This gives a rapid horizontal movement to the right until it reaches the x -nullcline.
 - If the point is above the x -nullcline, $dx/d\tau$ will be negative, and gives a rapid horizontal movement to the left until it reaches the x -nullcline.
- The point lies on the x -nullcline, then $dz/d\tau$ is nonzero.
 - If the point lies below the z -nullcline, $dz/d\tau$ is positive, the trajectory goes along the x -nullcline until it approaches the steady state intersection or - if there was no intersection - the maximum of the nullcline. In the maximum of the nullcline the trajectory must leave the nullcline, because $dz/d\tau$ is still positive, and jumps to the left, as it has been already described.
 - If the point lies above the z -nullcline, $dz/d\tau$ is negative, the trajectory goes along the x -nullcline until it approaches the steady state intersection or - if there was no intersection - the minimum of the nullcline. In the minimum of the nullcline the trajectory must leave the nullcline, because $dz/d\tau$ is still negative, and jumps to the right, as it has been already described above.

Figure 6 shows the three different behaviors of the BZ-reaction with respect to the above considerations. Figure 6a represents a system with one stable steady state. Starting from an arbitrary initial point, the system reaches the steady state within a short time, and remains in this point forever.

According to Figure 6b it is possible that the steady state is unstable, the intersection lies in the central branch of the x -nullcline. Starting from an arbitrary point the trajectory forms a limit cycle around the unstable steady state, which will be never reached. The system oscillates with a given amplitude and period. If the system receives some perturbation later on, it will return to

the same limit cycle and hence to oscillations of the same amplitude and period similarly to Figure 4.

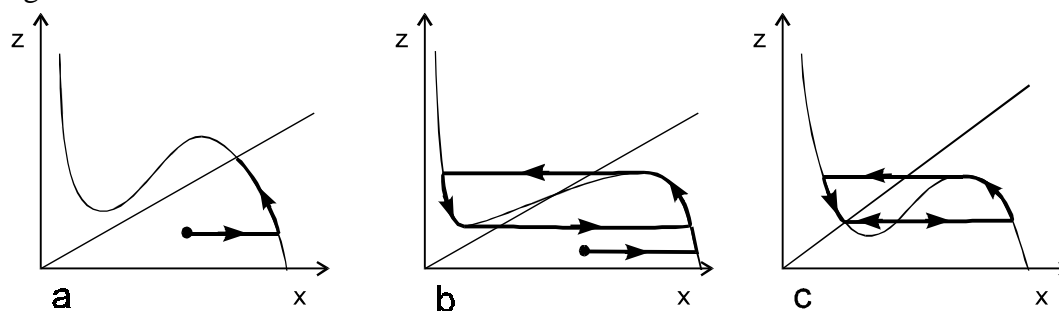


Figure 6. Steady state, oscillation and excitability in the BZ-reaction.

The Oregonator model calculated with different f parameters: (a) $f=1/4$; (b) $f=1$; (c) $f=3$

An excitable system (Figure 6c) is characterized by having a stable steady state and thus it is not spontaneously oscillatory. Small perturbations disturb the system from this state transiently, but it returns quickly. With slightly larger perturbations, the system is stimulated into a single excursion, with a color change forth and back, and a single large peak in the intermediate concentrations, similar to a single oscillation, before returning to the original steady state. The system responds in a qualitatively different way to perturbations that are below and above some critical or threshold value. In Figure 6c the steady state intersection lies slightly to the left of the x -nullcline. If the concentration of x is increased by some perturbation to some value, that remains to the left of the central branch of the x -nullcline, the system simply returns to the steady state. If the perturbation brings the system across the x -nullcline it jumps to the left-hand branch and starts a long excursion until it reaches the steady state again. While the system is moving along the left-hand branch of the x -nullcline, it is less sensitive for further perturbations, and is called refractory. As the system approaches the steady state the perturbation threshold decreases. Finally it reaches the steady state with the original excitable properties.

2.6. Excitable medium and chemical waves

Let's suppose a cell as the excitable system. Connecting the cells subsequently a one-dimensional (1D) medium is obtained. Connecting one-dimensional media subsequently a two-dimensional (2D) medium is formed. It is also possible to build 3D media in such a way, but in our case the 2D medium has priority. The connection type of the cells can be various:

- There is no transport between two cells, they are isolated from each other. Exciting the cells subsequently a pseudo wavetrain forms which is called a phase wave.
- There is diffusion between the cells. Exciting only one cell, the autocatalyst diffuses with a short delay into the neighbor cells which will be also excited, if the concentration of the autocatalyst is able to reach the threshold perturbation limit. This wave is called a trigger wave.
- A combination of the two possibilities is called a phase-diffusion wave.

In the following we will always discuss trigger waves. A pictorial example for a trigger wave is burning, in the 1D case the ignition cord for instance. Exciting the cord with a threshold above perturbation (let it catch fire) the cord burns to the end. The autocatalyst is heat, that is spreading over by heat transport and exciting the neighboring regions. This is a nice example, unfortunately not exactly true in our case, because there is no regeneration after burn out, thus it

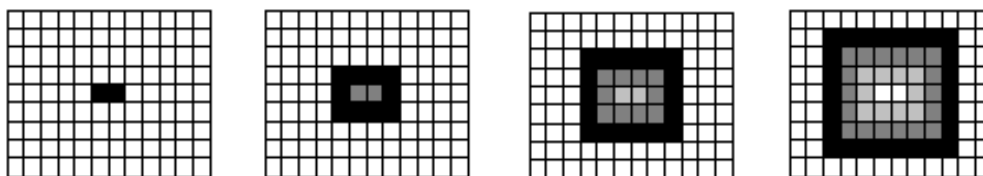


Figure 7. The cellular model of spreading out of chemical waves

□: Cell in steady state; ■: cell in excited state; gray cells are in different levels of regeneration. A small region was excited on the first picture, because of diffusion it spreads out for all cells, without any further outer influence.

is impossible to fire the cord again. A better example for the 2D case is the prairie fire. Starting from a point on the prairie the fire spreads out forming a circle with increasing radius. Next year there is grass again on the prairie (the medium has regenerated) and can be burnt again. Figure 7 and Figure 8 show chemical waves in a cellular model and in the BZ-reaction.

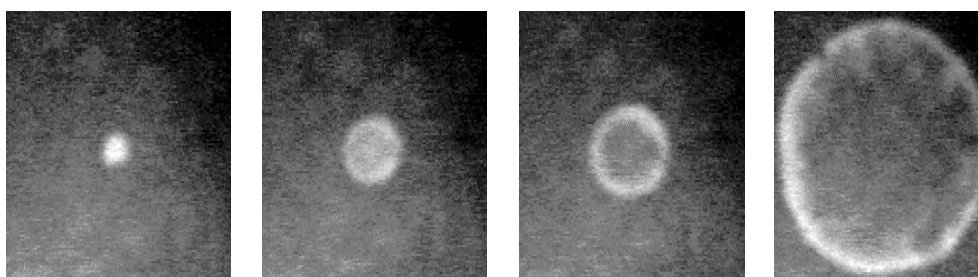


Figure 8. Chemical waves in the BZ-reaction. Digitized images

2.7. Properties of chemical waves

Trigger waves are formed by coupling of nonlinear chemical reactions and diffusion. The waves can be considered as spreading of concentration gradients in an excitable medium (Figure 9). The part of the wave in the direction of propagation is called the wave front (F) which is followed by the back (B) of the wave. In the BZ wave front the autocatalytic production of HBrO_2 and the oxidation of the catalyst takes place while the inhibitory bromide is consumed in the wave back. A new wave can only be initiated if the inhibitor

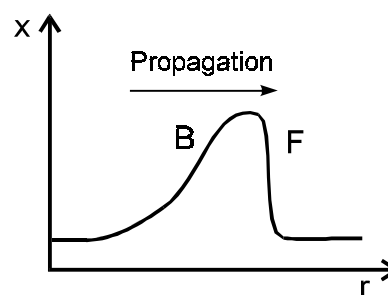


Figure 9. Propagating wave front

x is the concentration of autocatalyst, B denotes wave back, F is the wave front, and r is a local coordinate.

concentration has already decreased below a given threshold. The properties of chemical waves can be characterized using the above considerations:

- Opposite to physical (mechanical, sound) waves, there is no reflection or interference.
- Chemical waves are propagating with a constant velocity in a homogeneous medium. The speed of the propagation in the case of a first order autocatalytic reaction in a medium free of inhibitor is

$$v_o = 2 \cdot \sqrt{D \cdot k}$$

where D is the diffusion coefficient of the autocatalytic species and k is the rate constant for the first order autocatalytic reaction.

- The velocity of chemical waves depends on the frequency of initiating, and thus on the distance between two subsequent waves. If the wave is forced to propagate in a region which is not completely regenerated, the autocatalyst first reacts with the rest of the inhibitor, thus the speed is decreasing. The smaller the distance between the waves, the smaller the velocity. This effect is called dispersion.
- The velocity of chemical waves depends on the curvature of the wave. It was shown theoretically [26], that the velocity in the case of the curvature effect is

$$v = v_o - QD$$

where D is the diffusion coefficient of the autocatalyst, Q is the wave curvature (Figure 10) and

$$Q = 1/R$$

where R is the radius of the curve in the point P . However, curvature effect plays an important role only in experiments, where the radius R is in the order of μm .

- The wave front can be broken up either mechanically or chemically; then it forms free wave ends. The development of these free wave ends depends on the excitability of the medium. In a system with high excitability the wave ends form stable spirals (Figure 11, Figure 12), in a low excitable system the wave fronts shrink and disappear finally. The dynamics of spiral waves is one of the most studied phenomenon within the research on nonlinear dynamics.

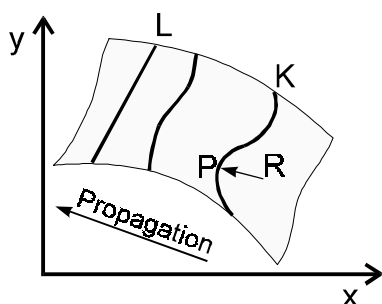


Figure 10. Curvature effect

x and y are the two local coordinates, L denotes a planar wave front, K is a curved wave, R is the radius of the wave in the point P .

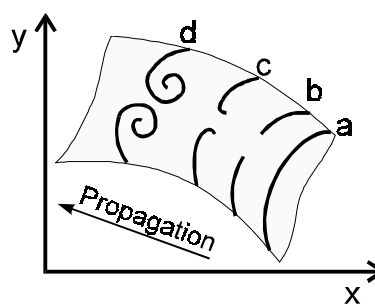


Figure 11. Spiral development

The continuous wave (a) was broken up (b) and the free wave ends form a double spiral (d).

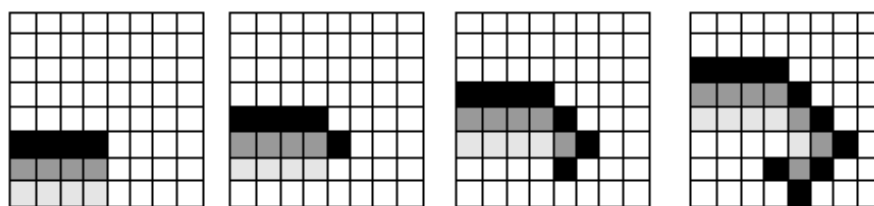


Figure 12. A cellular model of spiral development

2.8. Reactor types

First the exotic reactions were studied in open tank reactors (Continuously fed Stirred Tank Reactor, CSTR). CSTRs are very suitable keeping a chemical system far from equilibrium. Time-dependent periodic phenomena, reactions breaking symmetry in time can be observed in such reactors. A stirred system far from equilibrium is able to produce time-dependent self-organization. Writing the transport processes in the mass balance equations for such flow reactors results in systems of Ordinary Differential Equation (ODE).

Because of stirring in the CSTR there is no possibility of developing stationary structures or chemical waves (no inhomogeneities can exist in a well stirred reactor). Therefore, a new type of reactor, the so called CFUR (Continuously Fed Unstirred Reactor) was developed. Describing the behavior in a CFUR Partial Differential Equations (PDE) must be used. PDEs have the ability to describe temporal-spatial structures. The type of the developing structure depends not only on the reaction kinetics, but also on the transport properties of the medium. There are two main families of the spatial structures studied in the recent years: chemical waves and Turing patterns.

2.9. Turing patterns

In 1952, Alan Turing predicted theoretically in the work “The Chemical Basis of Morphogenesis” [27], that chemical systems showing feedback in situations where not all species diffuse with the same mobility might give rise to spontaneous pattern formation. An initially homogeneous well-mixed homogeneous solution would produce enhancement and depletion in the concentrations of some of the species (almost 40 years later the first experimental results⁷ were published by Castets et.al. [28]). Turing suggested that this kinetic-diffusion process might underlie the spontaneous development of spatial form in morphogenesis, e.g., of a developing embryo. The mechanism has also been applied for describing the spots and stripes marking animal coats and how these change with the size of the animal.

⁷ This first experimental Turing pattern has been observed by carrying out a chlorite-malonic acid- I_2 reaction in a gel into which starch as complexing agent was incorporated. Starch bound the I^- and I_3^- ions. This big complex had a smaller diffusion mobility in the gel and made the large difference in diffusion coefficients required for Turing patterns. Until now no Turing pattern could be observed in the BZ-reaction.

To understand the formation of Turing patterns let us shortly return to the pictorial example of the prairie fire. Let's assume additionally that the smoke produced by the fire has an inhibitory effect on fire and somehow the smoke diffuses much faster than the fire propagates. In this case there will be no fire front on the prairie but small, only locally burning fires will appear after the smallest perturbation of the initially unstable homogeneous state. This is because the autocatalytic fire can maintain itself but in its environment the smoke prevents the fire propagation. This is a phenomenon observed often in biology: short range activation combined with long range inhibition which can be responsible for many patterns in plants and animals as well.

3. Short History of Chemical Wave Experiments

For a long time, experiments reported on concentric and spiral-shaped waves were carried out in thin layers of BZ solutions [29,30,31]. In these closed systems, the reagents were gradually consumed, therefore the applied solutions were ageing rather rapidly, and it was not possible to maintain constant conditions for a longer time. Also, the commonly used ferroin catalyst has a tendency to decompose at usual BZ conditions. Furthermore, in solutions the disturbing effect of convection and hydrodynamic motion cannot be separated from reaction-diffusion phenomena. Finally, in most BZ solutions bubble formation due to gas evolution also interferes with pattern formation.

To eliminate these disadvantages of liquid systems, gel media were suggested to study chemical waves in the BZ reaction [32]. The polymer structure of gels prevents convection but it does not influence significantly the diffusion of the small molecules [33,34]. Kuhnert was the first to use agar-agar gel [32], in which all the components including the catalyst could diffuse freely. In an early work the catalyst of the reaction was immobilized in silica gels [35]. Interestingly, two works on BZ waves used home made collodion membranes (that is cellulose nitrate) to fix the catalyst [36]. To avoid convection, Winfree used Millipore filters and Aerosil (or Cabosil) gelling agent [37,38]; however, this method remained a curiosity for a long time. It is interesting to remark that Winfree also noticed that the different commercial membranes influence the wave propagation in a different way.

The real break-through of gel systems was the development of real open systems and of the so called continuously fed unstirred reactors (CFUR), which offered the possibility to study chemical waves under steady state conditions. Noszticzius et al. developed the first CFUR with a ring geometry using acrylamide gel and they created chemical pinwheels in that reactor [11]. Soon after other CFUR-s were constructed [12,13]. The openness of the system is also a necessary condition for producing Turing structures. For example, the first Turing structures were observed in the chlorite-malonic acid- I_2 -starch (CIMA) reaction in a gel-ring reactor [28]. Later on, Turing Patterns were observed in gel-free narrow capillaries, too [39]. Two-dimensional Turing structures were also observed [40,41,42]. Gel systems were used to study three-dimensional pattern formation as well [35,43,44]. Steady concentration gradients were maintained in a special arrangement of gel [45]. A survey on the possible gel systems was presented by Yamaguchi et. al. [33].

In most of the gel systems listed above the BZ reaction was running in the gel. Immobilizing the catalyst on the surface of a membrane or an ion exchange resin offers special means to influence the transport processes and obtain real two-dimensional patterns. Maselko and Showalter loaded ferroin on the surface of cation-exchange resins and observed spirals on the spherical surfaces [46]. The use of ion-exchange resins was also suggested by Zhabotinsky and Rovinsky to immobilize the activator component of the BZ reaction [47]. Slow diffusion of the activator relative to the inhibitor is another necessary condition to achieve Turing-structures,

but in the BZ reaction this was not realized so far. Cation-exchange membranes produced interesting crossing phenomena [48,49] but no Turing-structures were found. Most recently, chemical waves were studied in narrow capillary tubes [50].

4. Experimental

4.1. *Immobilization of catalysts on membrane surfaces*

Two types of membranes were investigated in our experiments: cellulose nitrate and polysulfone membranes. Both of them are commercially available. The immobilization methods and the applied catalysts were different for the two types of membranes.

4.1.1. *Fixation of ferroin on cellulose nitrate membranes*

For cellulose nitrate membranes (Sartorius, pore size 0.20 μm , diameter 47 mm) ferroin catalyst was applied. The preparation procedure used the following solutions: Solution 1: 600 mg of 1,10-phenanthroline (Figure 19, page 27) was dissolved in 12 cm^3 of 66 % (v/v) acetic acid. Solution 2: 0.5 cm^3 of 10 % sodium dodecyl sulfate solution (in water) was added to 20 cm^3 of 0.01 M Fe(II)ammonium sulfate solution, which also contained 0.2 M H_2SO_4 . The cellulose nitrate membrane was placed in Solution 1. After 15 minutes the membrane was washed with 10 % ammonia solution and placed into Solution 2 for 20 minutes. The membrane was continuously moved in Solution 2 and the solution was gently agitated with a glass rod for 20 minutes. This way the ferroin catalyst formed a homogeneous coating on the surface of the membrane and on the surface of the pores. The membrane was washed for 20 minutes in distilled water to remove an excess of ferroin, which was fixed only loosely. Membranes prepared this way can be stored in darkness under water for weeks without any substantial loss of activity.

4.1.2. *Fixation of bathoferroin on polysulfone membranes*

For polysulfone membranes (Gelman, pore size 0.45 μm , diameter 47 mm) 'bathoferroin' (the complex of iron(II) and bathophenanthroline analogous to ferroin, Figure 20, page 27) catalyst was applied. The fixation procedure applied two different solutions: Solution 3 and Solution 4. Solution 3: 30 mg of bathophenanthroline (4,7-diphenyl-1,10-phenanthroline) was dissolved in 5 cm^3 glacial acetic acid. Solution 4: 20 cm^3 0.002 M Fe(II)ammonium sulfate solution in 0.2 M H_2SO_4 .

The dry polysulfone membrane was dipped briefly into Solution 3 (about 2 seconds) and placed into Solution 4 for 2 minutes. The membrane was continuously moved in Solution 4 and the solution was gently agitated with a glass rod again to avoid any inhomogeneity in the catalyst formation. Then it was washed in distilled water for 20 minutes. We stored membranes prepared this way in darkness under water.

In the case of gelled membranes (see section "Gelation of membranes and filter papers", page 19) the membrane was placed for ten minutes in glacial acetic acid to remove its water content. Next, it was moved into Solution 3 for another 10 minutes and then into Solution 4. After ten minutes the membrane was washed with distilled water.

4.2. Creating different geometries

Chemical waves are only propagating in membrane regions where the catalyst is fixed. To investigate the properties of chemical waves it is necessary to create channels of any geometry. In this work two simple methods were developed.

4.2.1. Cutting the membranes

The commercial microfiltration membranes used in our experiments were rather strong and easy to cut. This was especially true for the polysulfone membranes while the cellulose nitrate membranes were somewhat weaker. We cut rings out of these membranes by placing the membranes between two sheets of paper and cutting the paper together with them. To cut these rings we used knives consisting of two concentric rings. The outer ring had a diameter of 40 mm, for the inner ring diameters of 10, 20, 30 mm were used. The knives were made from stainless steel and the distance holder was made from hard PVC.

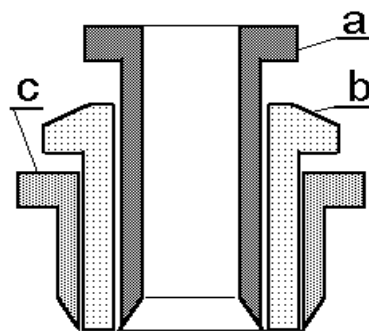


Figure 13. The knife used for cutting concentric membrane rings.

(a) inner knife, (b) distance holder (c) outer knife

4.2.2. Catalyst patterns painted on polysulfon membranes

There is another method for creating excitable regions on the membrane. Now, the catalyst is fixed only at certain membrane regions and other regions are left free of catalyst, like a drawing on a paper.

The inner part of a fiber-pen was washed with acetone, dried and filled with Solution 3. This pen was used to make drawings on polysulfone membranes. After a short drying on air, the membrane was placed in Solution 4 to "develop" the drawings.

A further inventive development of the technique was achieved by Showalter and coworkers, who used an inkjet printer to put computer generated patterns of excitable zones on the polysulfone membranes [51].

4.3. Preparation of the BZ solution

Since the catalyst was immobilized on the membrane surface, no catalyst was applied in the BZ solution. In the following the BZ solution is always meant without the catalyst.

The BZ solution was prepared from stock solutions in a 50 cm³ stoppered Erlenmeyer flask. 2 cm³ 2M malonic acid solution, 2 cm³ 2M NaBrO₃ solution, 5 cm³ 2M H₂SO₄ solution and 4 cm³ 0.66M KBr solution was mixed together in this order. The bromide added to the mixture is consumed by the acidic bromate to form bromine. The bromine brominates the malonic acid producing a mixture of mono- and dibromomalonic acids. After the yellow color of Br₂ disappeared, 6 cm³ of 2M (NH₄)₂SO₄ and 0.5 cm³ 10% sodium dodecyl sulfate (SDS) solution

was added. The role of the ammonium sulfate was to make the mixture less acidic ensuring a higher pH and a longer lifetime for the fixed catalyst. SDS (0.24% in the final mixture) created a more uniform and reproducible environment on the membrane surface for the chemical wave experiments. In general the above recipe produced a relatively sharp contrast for chemical waves and was not strongly self-oscillatory in contact with the catalyst.

4.4. Gelation of membranes and filter papers

The geometry and velocity of chemical waves are very sensitive to the transport properties and to the local concentrations of the medium. The membrane with the fixed catalyst is not in close contact with the glass fiber filter disc. There are places where the contact between the two is not uniform, small air bubbles may remain there, or the rim of the membrane bends up. At these places the BZ solution concentrations will be higher, because of the drying effect, causing an increased wave velocity and changing the shape of the wave front. To avoid these effects the membranes and also the glass fiber filter discs were embedded in an acrylamide gel. Small molecules (water, bromate, malonic acid, etc.) have essentially the same diffusion properties in gels as in the liquid phase. On the other hand, the gelled surfaces are very smooth, thus the contact between them is much better.

To gel the membrane it was placed in solution M (monomer, 0.8% triethanol-amine, 0.8% N,N'-methylene-bis-acrylamide, 16% acrylamide in water) and the air bubbles in its pores were removed and replaced by the monomer solution applying vacuum. Then the membrane was placed on a glass plate in a small pool (2-3 cm³) of solution M. To initiate the polymerization 5-6 drops of solution I (initiator) were added to the pool and mixed rapidly. Solution I was prepared freshly by mixing solution I₁ (20% of ammonium-peroxi-disulfate in water) and solution I₂ (1.6% N,N'-methylene-bis-acrylamide and 32% acrylamide in water) in a 1:1 ratio. To produce a smooth and thin gel another glass plate was placed on the top of the membrane immediately. After ten minutes the glass plates were removed and the gel was washed with distilled water. The ready made membranes had an overall thickness of 200 μm and were stored in distilled water. The same method was used to gel filter paper and glass fiber filter discs.

It has to be explained why exactly this recipe was applied instead of direct polymerization of solution M. In that case - if the mixing is not perfect - the monomer would be diluted at places where the initiator solution was added causing holes in the gel. Because the mixture of solutions I₁ and I₂ has the same monomer concentration as solution M this dilution effect cannot occur. Furthermore, the separated initiator solutions last longer, because the mixture of them polymerizes after approximately 15 minutes.

4.5. Creating membrane zones with reduced wave velocity

Two methods have been developed for creating zones with reduced wave velocity. One method was a precipitation of BaSO₄ concentrated on a small spot in the gelled membrane. First

a small disk of glass fiber filter - in the size of this spot - was cut. It was wetted with concentrated Ba-acetate solution and placed on the top of the membrane. Under the membrane there was another glass fiber filter disk with a hole in it and wetted with water. The hole was the same size as the small disk with Ba-acetate and was placed exactly below it. This way the membrane region under the disk was in contact with the concentrated Ba-acetate solution while other regions were in contact with pure water. The Ba-acetate diffused into the membrane and after 15 minutes the membrane was placed on a glass fiber filter disk soaked with 5M H₂SO₄. After another 15 minutes the membrane was washed with distilled water. The precipitated microcrystals enhance the red color of the catalyst, this makes the precipitate region darker. The method can be repeated to increase the amount of the precipitate on the same spot. The other, simpler and more reproducible method for creating membrane zones with reduced wave velocity was placing a piece of foil under the membrane.

4.6. Reactors

Two different reactors were developed, one was a simple Petri dish reactor for preexperiments and demonstration, while the other one was intended for the investigation of chemical waves with the possibility of controlling the temperature, the atmosphere and also the chemistry.

4.6.1. The Petri dish reactor

This type of reactor was in fact a batch type one but worked as a CFUR for many hours. It consists of a Petri dish and a glass fiber filter disc (Macherey-Nagel GmbH, Rundfilter GF-2, diameter 55 mm) as shown in Figure 14. The glass fiber filter disc was soaked with the BZ solution and it was placed in the reactor. The membrane with the fixed catalyst was simply placed on the top of the filter disc. In this reactor the BZ components can diffuse to the surface of the membrane, the reaction takes place only on the surface covered with the catalyst and the reaction products can leave the surface in the same way. Therefore this arrangement is OPEN, the transport of the components is provided by diffusion, at least for some hours.

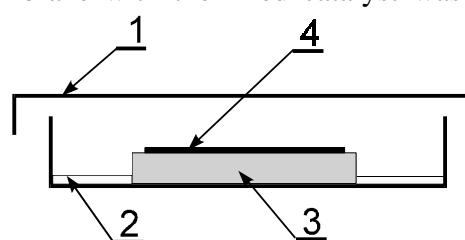


Figure 14. The simple Petri dish reactor

1. Petri dish with cover,
2. BZ solution with no catalyst,
3. glass fiber filter disc,
4. membrane with fixed catalyst

It is interesting to remark that the reaction catalyzed by the membrane surface consumes negligible amounts of the BZ reagent. Thus the diffusional feed from the glass fiber filter disc soaked with the reagent probably would be enough to maintain chemical waves for a much longer time than the observed 8-10 hours. Therefore the time limitation of the experiments is not due to the consumption of the reagents by the catalytic membrane, rather it is due to a drying effect caused by the imperfect isolation between the dish and the cover. Another effect

which limits the time of the experiments is the hydrolysis of the oxidized form of the catalyst. As the amount of the reaction products was minute, no bubble formation occurred in the experiment. This is an advantage, because conventional chemical wave experiments with the BZ reaction were often disturbed by bubbles.

A slightly modified version of the reactor applied a gelled glass fiber filter disc and a gelled membrane. This arrangement enhanced the contact between the membrane surface and the BZ soaked disc. Chemical waves could be maintained in this simple reactor for more than one week provided that the cover of the reactor was tightly closed to prevent evaporation. The observed wave propagation was somewhat slower than in the gel free reactor. Probably this is caused by a Hofmann-degradation type reaction between the polyacrylamide gel matrix and hypobromous acid, a process generating bromide and slowing down the waves.

4.6.2. A real continuously fed membrane reactor

To perform extended experiments with modified membranes a special new CFUR was constructed, shown in Figure 15. The reactor consists of three main parts. Part A ensures a

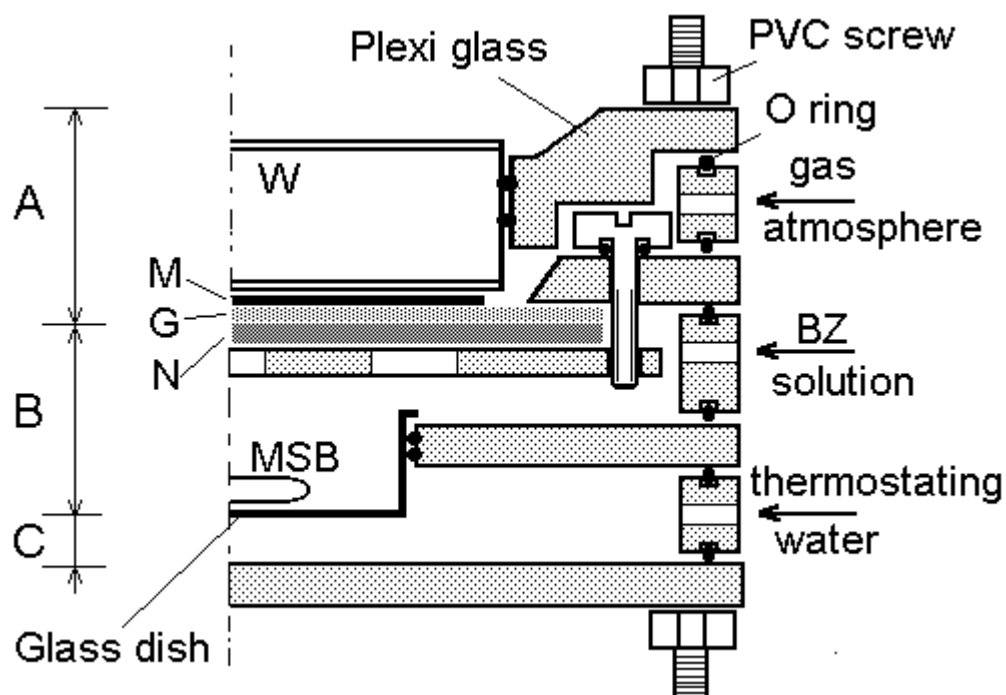


Figure 15. Cross sectional view of the reactor.

Dotted elements with solid borders are made of plexi-glass, the screws are made of hard PVC. The function of the different parts are described in the text.

controlled atmosphere above the modified membrane. It is separated from the environment by a double glass window. Part B is designed for the BZ reagent to feed and to flow out. Part A is separated from part B by a polyacrylamide gelled filter paper. This prevents a mechanical flow of the liquid from part B to A but allows the diffusion of the chemical components. The

membrane with fixed catalyst is placed on the gelled filter paper. Part *C* of the reactor is a small thermostat to keep the temperature constant.

The gelled filter paper (*G*) separating parts *A* and *B* lies on a polypropylene net (*N*) to keep its surface flat. The gelled membrane (*M*) with the fixed catalyst is placed on this flat surface. The magnetic stirrer bar (MSB) in the glass dish improves the heat exchange between Part *B* and *C* and eliminates temperature and concentration gradients inside *B*. The waves running in the membrane can be observed through a double glass window (*W*). To enhance heat isolation the interior of the window is evacuated. In addition the window can be electrically heated by a resistance wire to prevent water condensation on its outer surface in experiments where the reactor is used below laboratory temperatures.

4.7. The experimental setup

A schematic diagram of the experimental setup with the reactor is given in Figure 16. A special device besides the reactor is a vacuum flask containing a long silicon rubber tubing. This device removes carbon dioxide from the BZ solution continuously. The BZ solution is pumped through a heat exchanger and a thin walled silicone rubber tubing (inner diameter 2.0 mm, outer diameter 2.7 mm, length 6m) placed in the vacuum flask. Gases dissolved in the solution, especially CO₂ which has a high permeability in silicone rubber, permeate through the wall of the tubing and are removed by a vacuum pump. With this method removing of already existing gas bubbles in the reactor is also possible. The pumping rate is about 15 ml/min. After gas elimination the liquid enters the reactor and the container with the stock solution.

As the fixed catalyst consumes only minute amounts of the reagent the same BZ solution can be recirculated for days. In experiments applying a controlled atmosphere the dry inert gas (presently N₂) is saturated with water vapor before entering the reactor. A ring shaped lamp is

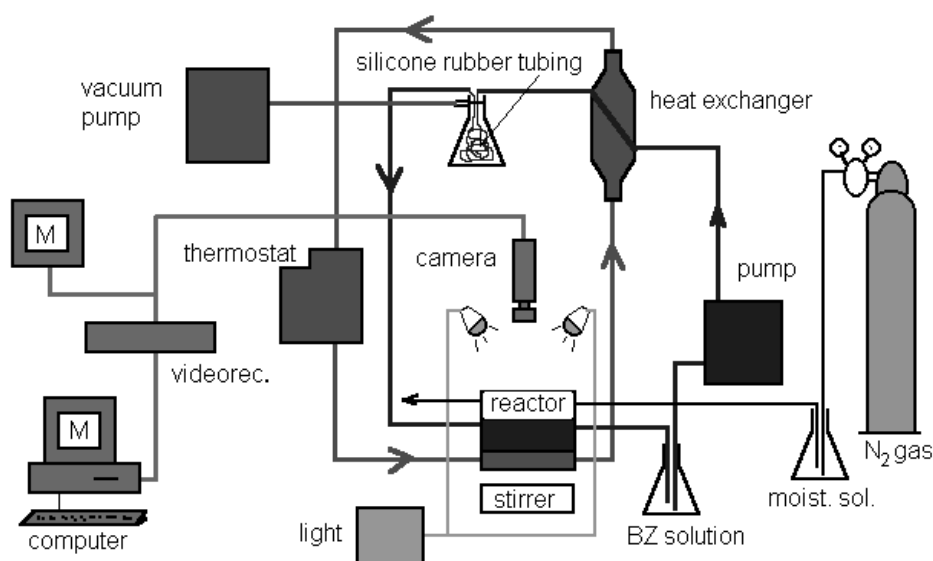


Figure 16. Schematic diagram of the experimental setup.

used to homogeneously illuminate the membrane. The records are taken with a CCD camera and stored in a video recorder and in the computer.

4.8. *Starting an experiment*

It is rather difficult to manipulate the waves in the reactor, because the gel dries out very rapidly if the reactor is open. Therefore the pinwheel was always created in a Petri dish, and then the membrane was placed in the reactor.

4.8.1. *Starting chemical waves*

The glass fiber filter paper was placed in the Petri dish and it was wetted by the BZ solution. Then the membrane with the fixed catalyst was placed on it.

There are several ways to start chemical waves: touching the membrane with a silver wire or a silver nitrate crystal or using small pieces of highly excitable or self oscillatory membranes as pacemakers, which were made by applying a more acidic BZ solution. Silver nitrate crystals were not used in our experiments, because after initiation, small drops of silver nitrate solution remain on the surface of the membrane working as pacemakers for a longer time.

The initiated wave develops as a target pattern (Figure 7, page 11). Spirals could be created by perturbing the initial target patterns. (The wave front was gently touched with an iron paper clip, a method suggested by L. Kuhnert.) It is also to be noted here, that spirals work as wave source after creation, by rotating around a core.

4.8.2. *Creating a chemical pinwheel*

Chemical pinwheels are wave fronts propagating in the same direction in an annular membrane. To create a chemical pinwheel, a spiral wave was initiated on the annular membrane. This spiral as a pacemaker sends waves in both direction in the membrane ring, clockwise and counterclockwise. The waves propagating in one direction, let's say the clockwise waves, were deleted by using the paper clip, thus only the counterclockwise waves remained. If the number of counterclockwise waves was sufficient the spiral was also deleted. The distances between the arms of the pinwheel were equalized after some time because of the dispersion effect. After the pinwheel was ready, the membrane with the rotating waves was placed in the reactor. The pinwheel usually survives this process. It is also possible to create the pinwheel in the reactor, but it is more convenient to manipulate the waves in the Petri dish.

4.8.3. *Loading the reactor*

After the gelled filter paper was placed in the reactor and fixed with the screws, the reactor was loaded with the BZ solution. To maximize the contact surface between the gel and the liquid, all bubbles were removed by keeping the reactor slanted, so that the outflow tube pointed to the top letting the air out. When the reactor has been already loaded, it was moved back to its horizontal position. The flask with the BZ solution was always kept below the level of the

reactor to keep the pressure slightly lower than the atmospheric pressure. The pressure difference of approximately 10 mbar was enough to keep the gelled filter paper (*G*, see Figure 15) flat, soaked onto the supporting net (*N*). The membrane (*M*) with the created pinwheel was then placed in the reactor, and it was covered with a thin PVC foil (household foil) to avoid evaporation even into the reactor inside. Any halogenid (Cl^- , Br^-) traces on the foil (fingerprints!) can disturb or even break up the waves, therefore the foil was carefully washed with distilled water before placing it onto the membrane, and gloves were used at this step to avoid further impurities transferred from the skin into the reactor. The reactor was then closed, stirring and thermostating was turned on.

5. Results and Discussion

5.1. Composition of the BZ solution

A HPLC analysis was made to check the composition of the BZ solution described in the section "Preparation of the BZ solution" (page 18). There are many bromination products beside the theoretically expected bromomalonic acid, as shown in Figure 17. Table 1 lists the concentrations calculated from Figure 17. The retention times for the identification of the peaks and the extinction coefficients ϵ were taken from [52,53]. The first peak is the injection peak containing mainly bromate. Note that there are only traces of Br_3Ac in the solution; however, the UV signal is relatively high, because of the very high extinction coefficient.

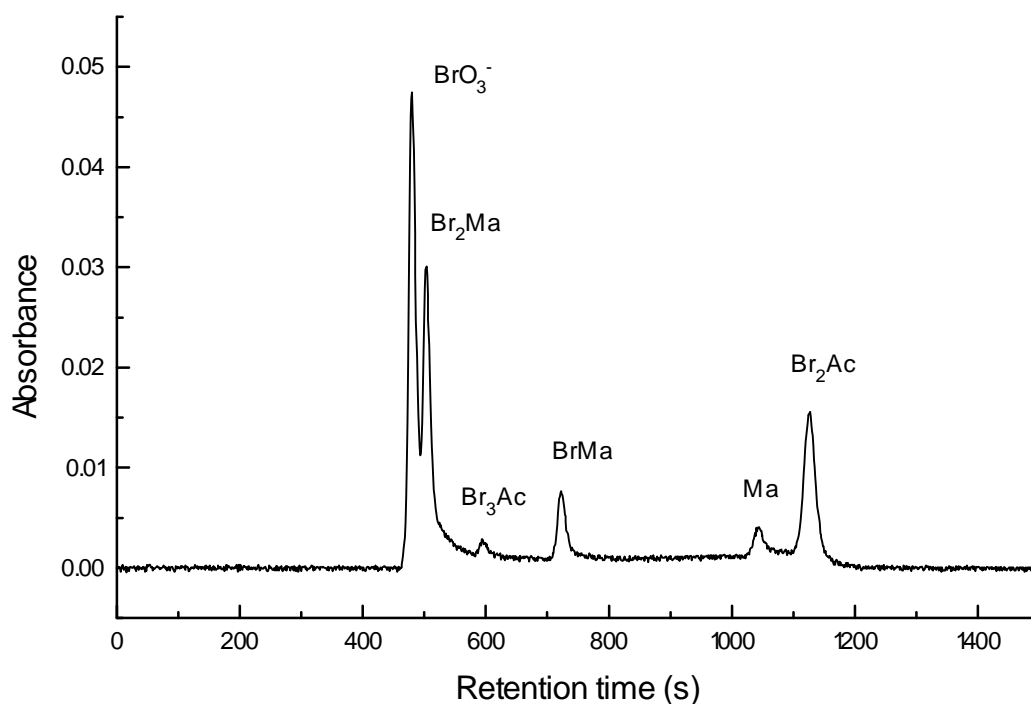


Figure 17. Reaction products of bromination in the freshly prepared BZ.

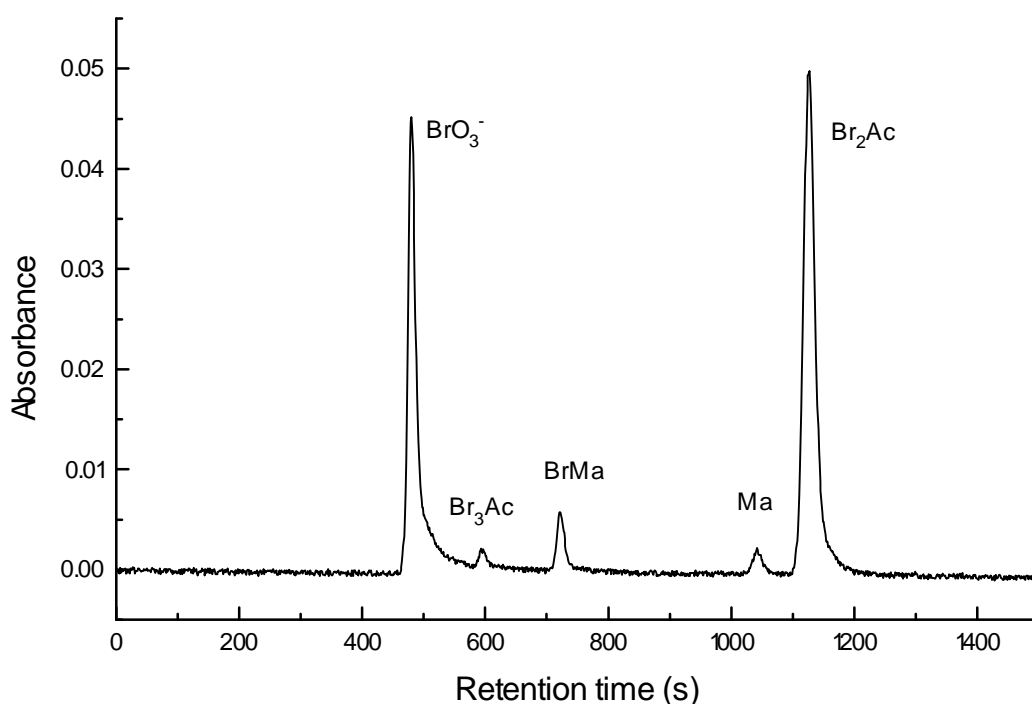
Preparation of the sample: 1.4 ml of the BZ solution (sodium dodecyl sulfate was not added) was diluted to 50 ml. 5 ml of this stock solution was diluted again to 50 ml (the overall dilution is now 1:350) and injected into the HPLC. 0.01 M H_2SO_4 was used as eluent, and the column was thermostated at 45 °C. The peaks were detected at 220 nm.

Table 1. Properties of selected products in the freshly prepared BZ checked by HPLC. The initial concentration of malonic acid was 0.186 M.

name	notation	ϵ ($M^{-1} \text{ cm}^{-1}$)	concentration (M)
malonic acid	Ma	11	0.078
bromomalonic acid	BrMa	120	0.026
dibromomalonic acid	Br ₂ Ma	166	0.063
dibromoacetic acid	Br ₂ Ac	220	0.023
tribromoacetic acid	Br ₃ Ac	700	0.0005

A decomposition process of Br₂Ma began immediately after the BZ solution was put together. Figure 18 shows the composition of the solution after 24 hours. The Br₂Ma disappeared completely within this time and the peak of Br₂Ac became higher. The concentration of the other components did not change.

We did not observe any changes in the chemical wave geometry or velocity which could have been attributed to the changing of these concentrations. Probably these components do not play any important role in the kinetics of the chemical waves. It should also be noted, that most of our experiments were carried out some hours after preparation⁸ of the BZ solution, when the majority of the Br₂Ma has already decomposed.

**Figure 18. The composition of the BZ after 24 hours.**

Br₂Ma disappears completely and the concentration of Br₂Ac grows to 0.086 M.

⁸ There are also technical reasons for the delay between preparation of the BZ solution and the start of the wave experiments. Creation of the pinwheel for the reactor experiments, removing of bubbles from the reactor, thermostating to a constant temperature and achieving an asymptotic state of the pinwheel arms in the reactor need a minimum of time.

5.2. Comparison of different catalyst-membrane systems

We started our experiments using cellulose nitrate membranes. Placing a catalytic membrane ring on the top of a glass fiber filter disc previously wetted with the BZ reagent generates spontaneously appearing waves. These waves can be systematically perturbed to form a pinwheel. However, here some problems arise with the cellulose nitrate - ferroin system. First of all, the orange color of ferroin and the light blue waves (ferrin) didn't give a satisfying contrast for the image processing; it was even very difficult to take photos. Another problem is that the ferroin catalyst couldn't be fixed strongly enough on the cellulose nitrate membrane, causing a slightly "bleeding" of the catalyst during the experiment.

To overcome these difficulties we tested other membranes and catalysts. We found that the polysulfone-bathoferroin system displayed a better contrast, greater stability and no "bleeding", compared to the cellulose nitrate-ferroin system. This is not only due to the darker purple color of the catalyst, but also to the much higher whiteness of the polysulfone membranes that "lights" through the waves (compare Figure 2 and Figure 4 in [54]). Thus in later experiments the polysulfone-bathoferroin system was used exclusively. It is important to emphasize, however, that cellulose nitrate-ferroin membranes can be also used in chemical wave experiments; this gives the possibility of combining different catalytic membranes within one experiment.

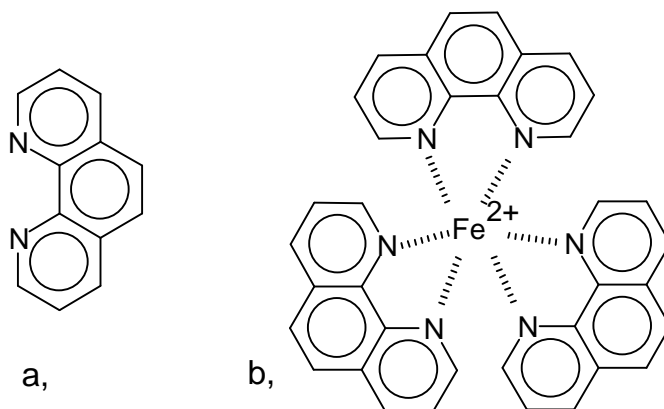


Figure 19. 1,10-Phenanthroline (a) and its iron(II) complex ferroin (b). The complex with iron(III) is called ferrin.

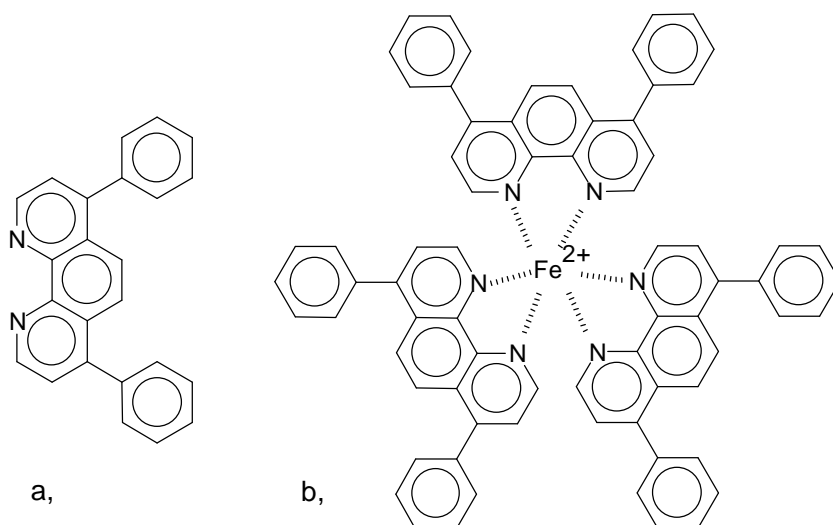


Figure 20. Bathophenanthroline (a) and bathoferroin (b)

5.3. The geometry of chemical waves in homogeneous medium

In 1946 Wiener and Rosenblueth [55] constructed a simple mathematical model to describe wave-like phenomena in excitable medium. In their classical paper they studied the conduction of impulses in nervous fibers and in cardiac muscles. Their postulates were:

- The impulses spread with constant velocity in every direction in the excitable medium.
- The amplitude of impulses remains constant while they are spreading.
- The points of the medium may exist in three different states: (a) “Active” state. This state occurs only at the instantaneous wave front; (b) “refractory” state. Its duration is assumed to be constant after passing the wave front; (c) “resting” state.

Using these postulates, Wiener and Rosenblueth gave a mathematical treatment of the evolution of wave fronts, and they derived several properties of wave propagation. Specifically, for the two-dimensional case, using Huygens’ principle, they concluded that the wave fronts starting from a point source are circles, and in the shadow region caused by a convex obstacle, the wave fronts are *involutives* of the obstacle.

5.3.1. A simple model of wave propagation

Let’s recall the concept of involutes⁹. In this case only the involutes of closed curves are considered.

Let C be a closed curve (of any convex form), which is the boundary of the hole (Figure 21). Involutives of C are the orthogonal trajectories of the tangents of C [56] and will be denoted by Γ . The distance between any point of the involute Γ_1 from an other involute Γ_2 of C is constant; it is the distance of the two involutes.

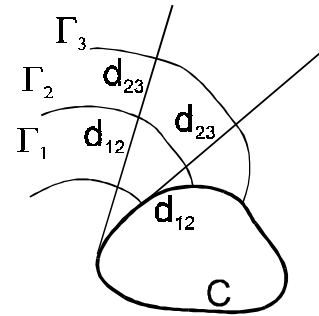


Figure 21. Involutives of a closed curve

Let’s return to the pictorial prairie fire model of wave propagation and consider the following two postulates:

- The fire propagates from any burning point in any direction on the plane where burning is possible. The velocity of propagation is denoted by v .
- If the fire can reach a point on different pathways, the real path of ignition is the one along which the fire arrives first.

From these postulates a Fermat principle for chemical waves can be formulated:

$$\tau = \int \frac{ds}{v} = \text{minimum}$$

Eq. 18

⁹ In pictorial terms an involute of an obstacle is the locus of the endpoint of a string which is laid along the obstacle and unwrapped keeping the string always tight.

The integral represents the propagation time belonging to a given path. The Fermat principle selects the real path which corresponds to the minimum propagation time between two points (Figure 22).

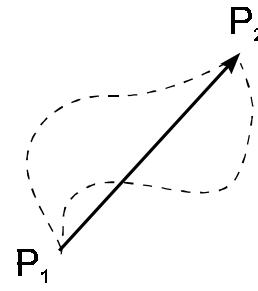


Figure 22. Fermat principle

The geometrical theory based on the above postulates allows us to determine the evolution of the wave fronts. Starting from any burning point of a fire front the propagation of combustion caused by that point can be followed, and the paths of ignition can be constructed this way. Let us assume that F_0 is the fire front at an initial instant t_0 (Figure 23). At time t_1 , the position of the front is F_1 , and at time t_2 it is F_2 . Since the velocity v was assumed to be constant (homogeneous case), the time minimum requires the shortest path in space, therefore the orthogonal trajectories of the front sequence F_0, F_1, F_2, \dots are straight lines (rays), and the distance between these fronts is $d_{01} = v(t_1 - t_0)$, and $d_{12} = v(t_2 - t_1)$, respectively.

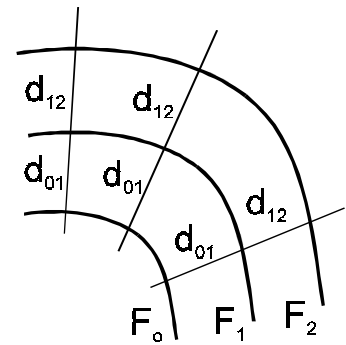


Figure 23. Evolution of fire fronts

Now, consider the propagation of chemical waves around a hole. If the initial wave front is an involute of the hole, it is transformed to another involute of the hole during the wave propagation (this follows from comparing Figure 21 and Figure 23). If the initial front F_0 was not an involute, it will generate fronts determined by F_0 in zone A, and the continuation of these front lines are arcs of involutes of the hole in the shadow “zone” B. The two zones are separated by the tangent e belonging to F_0 . In the case of a bounded region (e.g., in the case of an annular membrane), as Figure 24 shows, the front will necessarily be an involute of the hole after a finite time independently of the shape of the initial front.

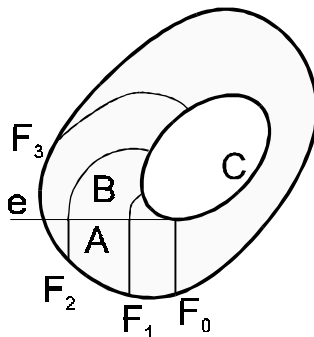


Figure 24. Formation of involutes starting from an arbitrary initial front

5.3.2. A special case: involute of a circle

In the case of a circle as obstacle it is easy to derive an analytical expression for the involute. Consider a string wound around the perimeter of the circle. Let us slowly unwrap the string (Figure 25, straight line AP) keeping it tightly and calculate the pathway which is drawn by the endpoint of the string. The string leaves the circle as a tangent in the point A. It means that

$$\overset{\frown}{AD} = \overline{AP} \tag{Eq. 19}$$

Now let's place the origo of the polar coordinate system in the center of the circle and describe the point P by the polar coordinates r and ϕ . According to the Pythagoras theorem, for the triangle OAP we obtain

$$r^2 = r_o^2 + (r_o\alpha)^2 = r_o^2(1 + \alpha^2) \tag{Eq. 20}$$

where r_o refers to the radius of the circle and $\alpha = \angle AOD$. From Eq. 20 it follows:

$$\alpha^2 = \frac{r^2}{r_o^2} - 1 \quad \alpha = \pm \sqrt{\left(\frac{r}{r_o}\right)^2 - 1}$$

Eq. 21

Furthermore, β can be expressed by r_o/r (triangle OAP):

$$\beta = \pm \arccos \frac{r_o}{r}$$

Eq. 22

Then we obtain, by combining the last two equations:

$$\varphi = \alpha - \beta = \pm \sqrt{\left(\frac{r}{r_o}\right)^2 - 1} \mp \arccos \frac{r_o}{r}$$

Eq. 23

Adding a constant angle φ_o to allow arbitrary starting of the involute along the circle, the final equation is:

$$\varphi = \varphi_o \pm \sqrt{\left(\frac{r}{r_o}\right)^2 - 1} \mp \arccos \frac{r_o}{r}$$

Eq. 24

An involute-shaped front may rotate in both direction, counterclockwise and clockwise. In Figure 25 the front rotates clockwise. When taking the second term in Eq. 24 with + sign and the third term with - sign we obtain the equation of the involute. The mirror image of this involute (taking the second and third term in Eq. 24 with the opposite signs) is also a stationary wave profile and we will call it *reverse involute*.

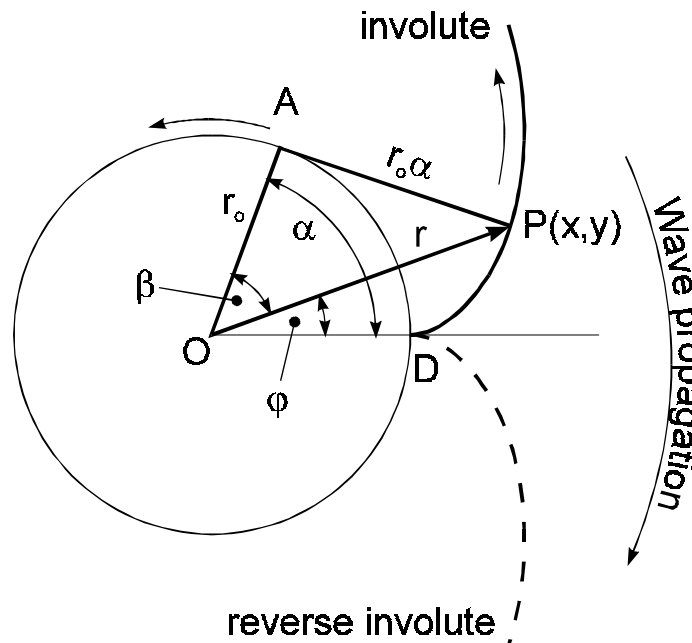


Figure 25. Geometry of involutes

Suppose a string that is wound around the perimeter of a circle. Let' s slowly unwrap the string keeping it always tightly. The endpoint P of the string follows the path of the involute.

5.3.3. Results

It was Winfree [29] who suggested first that the shape of spiral waves should be an involute of a small circle, the “core” of the spiral wave. This core is too small, however, to decide experimentally whether the shape of the wave front is an Archimedian spiral or an involute [57]. It is an additional problem that the tip of the spiral often meanders along a hypocycloid [44,58,59] instead of a small circle. Thus we decided to study a more simple situation: a two dimensional excitable medium with a relatively large and well defined “hole”. The waves can rotate around the hole as chemical pinwheels and according to the above geometrical theory the wave fronts should be involutes of the hole.

Digital images of chemical waves rotating around a circular hole can be seen in Figures 26 and 27. Subsequent images were subtracted, thus only the wave fronts remained in the pictures. Additionally, theoretical wave fronts which are evenly distributed involutes (the distances between the waves are equal) of the inner circle are shown (thin solid lines) corresponding to the asymptotical state.

In Figure 26 we consider a five-armed pinwheel. It can be seen, that only the starting points of the involutes fit well with the theoretical curves, however, the shape of the wave fronts is slightly different. The image in Figure 27 was taken after two arms of the five-armed pinwheel were deleted. It shows that agreement between theory and experiment becomes better when decreasing the number of arms. This observation suggests that deviations from the theory are caused by inhomogeneities in the membranes. Such inhomogeneity effects are enhanced,

when the frequency of wave trains is increased. At higher frequencies the time for recovery is relatively short. Using the prairie fire picture in this case the grass is fresh and “wet”. Thus close

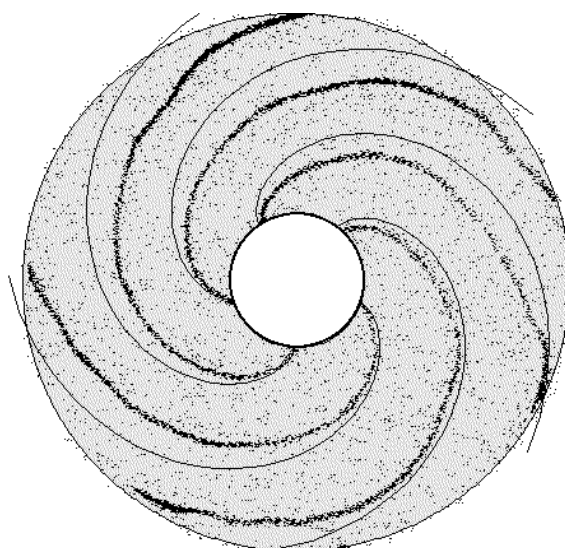


Figure 26. A five armed pinwheel rotating around a hole.

Outer diameter 40 mm. Dots: measurement, thin lines are calculated involutes of the inner circle.

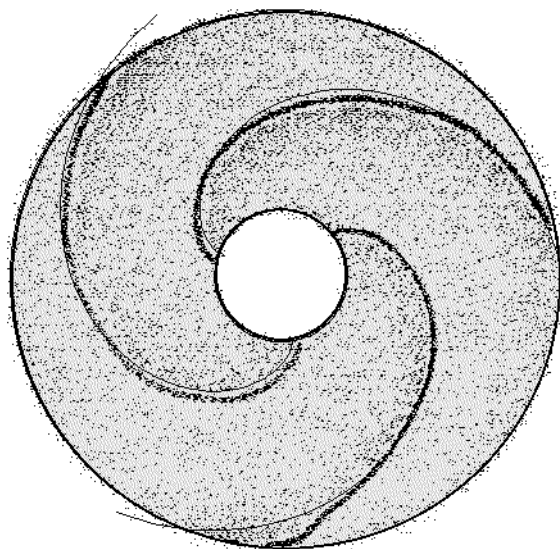


Figure 27. A three armed pinwheel.

Outer diameter 40 mm. Dots: measurement, thin lines are calculated involutes of the inner circle.

to the propagation failure small inhomogeneities can make a big difference. On the other hand, at lower frequencies there is enough recovery time - the grass is already “dry” - and small inhomogeneities don’t matter.

Figure 28 shows a different experiment, where the hole in the membrane is not a circle. A convex polygon hole has the advantage that its involutes are composed of circles, and this is easy to check. As an example, a triangle was cut out of the membrane. The theoretical wave fronts here are arcs of different circles centered at the vertices of the triangle. The vertices play the role of a wave source producing circular waves in the “shadow region”. The experimental wave fronts displayed in Figure 28 show a good agreement with the theoretical prediction, although in this case the number of arms is the same as in Figure 26. However, the circumference of the obstacle here is bigger than that in Figure 26, thus the distances between the waves are also bigger here. Therefore, the five arms of the pinwheel cannot disturb each other as strongly as in Figure 26.

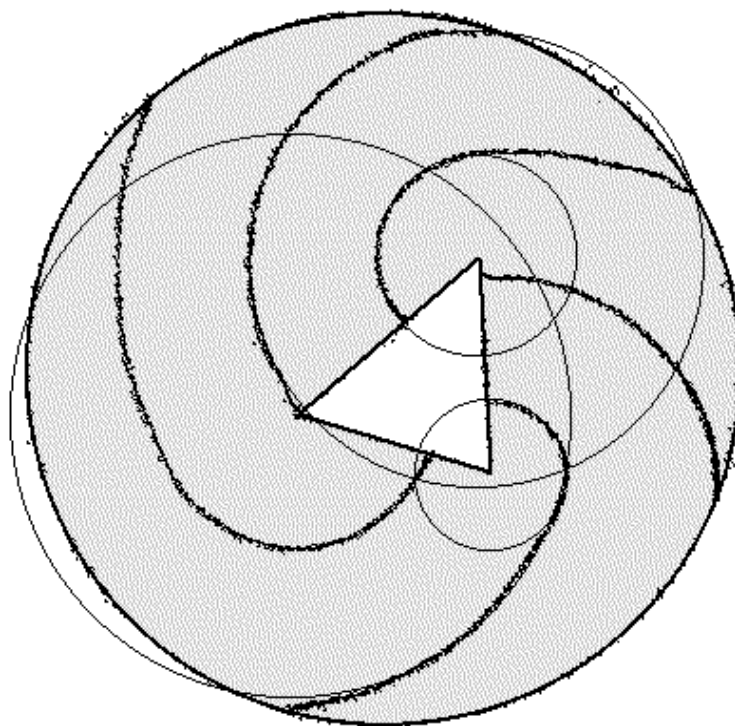


Figure 28. Chemical waves rotating around a triangular hole

Outer diameter 40 mm. Dots: measurement, thin lines calculated involutes (here circles) of the triangle. The centers of the circles are vertices of the triangle.

5.4. Refraction of chemical waves

Refraction of waves occurs on the boundary of two excitable zones with different wave propagation velocities. Thus our aim was to find a method to modify the physico-chemical properties of the excitable medium in a stepwise manner to create sharp boundaries between

regions of different refractivity. There are various prospective physical and chemical methods to reach this goal.

A possible physical method would be to modify somehow the pore size of the membrane in certain regions. The idea of this physical method is coming from a report by Müller and co-workers [34], who found that in silica gels structural differences influence the wave propagation.

Another possibility is to apply chemical methods to change the local wave velocity. However, to establish and to maintain an inhomogeneous chemical concentration distribution in the reactor is a necessary, but not a sufficient condition. E.g. in the annular gel [11,60] and in the gel strip [40,61] or slab [45] reactors the chemical concentrations are inhomogeneous as required but the concentration gradients are not localized to narrow boundary regions. Thus while the local wave velocity is space dependent, as it should be, it varies everywhere and in a continuous way, which is not optimal for wave refraction experiments.

To create stepwise changes in the local chemistry Zhabotinsky and co-workers [62] applied oxygen gradients in BZ systems [49], which are in contact with air. Due to these gradients the bottom of thicker layers of the BZ reagent can be free of oxygen while thinner layers can contain atmospheric oxygen close to saturation. The presence of oxygen changes the excitability of the BZ reagent. Thus Zhabotinsky and co-workers were able to observe wave refraction on the boundary of two silica gel layers with different thicknesses when both layers were open to air. They showed that Snell' slaw is obeyed for the boundary of two media, in which the components have different diffusion coefficients, but the chemical kinetics is identical.

The light sensitive BZ reaction (with the ruthenium bipyridyl complex as catalyst) was applied by Markus and co-workers [63]. The wave front curvature was deformed by projecting a light spot on the medium. In this way refractive phenomena analogous to traditional glass lenses in linear optics were observed. The excitability of the medium decreased at places of illumination; this caused an effect they called "chemical lenses".

5.4.1. Comparing two methods leading to local inhomogeneities

In our initial experiments we tried to change the local physical properties of the membrane. Barium sulfate was precipitated in the pores of the gelled membrane in certain regions. We hoped that changing the pore size with this method would influence the lateral diffusion (mass transport in the plane of the membrane) and would alter the wave velocity as a consequence. While these experiments were successful in slowing down the waves in membrane regions containing barium sulfate, it turned out that the crucial factor to achieve this result was not a change in the lateral but rather in the transversal diffusion (mass transport between the catalyst layer and the BZ reagent reservoir), which is perpendicular to the plane of the membrane. Soon it was realized that for the control of the transversal diffusion there are more effective and reliable means than precipitate formation.

Various diffusion barriers separating the fixed catalyst from the rest of the BZ reagents like plastic foils and porous Nuclepore membranes were tested successfully. It was found that with the aid of this new technique homogeneous regions of low wave velocity with different plane geometries can be formed rather easily by cutting appropriate shapes from the barrier membranes.

Presently the chemical nature of the intermediate responsible for the observed effect, is not clear. The inhibitory bromide ion is a strong candidate for that role. It is interesting to point out that the present construction, in principle, is similar to Zhabotinsky' swave refraction experiments. In that case also physical barriers controlled the transversal diffusion of another inhibitor, namely oxygen. Nevertheless the chemistry should be different because our measurements in an inert atmosphere prove that atmospheric oxygen plays no role in the wave refraction experiments reported here.

5.4.2. Wave refraction with $BaSO_4$ precipitate

A snapshot of wave fronts propagating through a barium sulfate precipitate region is shown in Figure 29. The picture was taken in an asymptotic state more than two hours after the creation of the pinwheel. The darker spot on the annular membrane is the region, where the precipitate was formed inside the gelled membrane. The waves slow down in this region, thus the wave front is deformed accordingly.

While these results were satisfactory on a qualitative level, there were some problems as well. First, to produce reproducible precipitate spots in the membrane and especially to control their shape was rather difficult. Second, the mechanism of slowing down the waves was not quite clear for us. Initially it was assumed that blocking the pores or making them more inaccessible by precipitate formation may slow down the lateral diffusion in the membrane somehow.

Another possibility was, however, that the precipitate layer in the membrane can hinder the mass

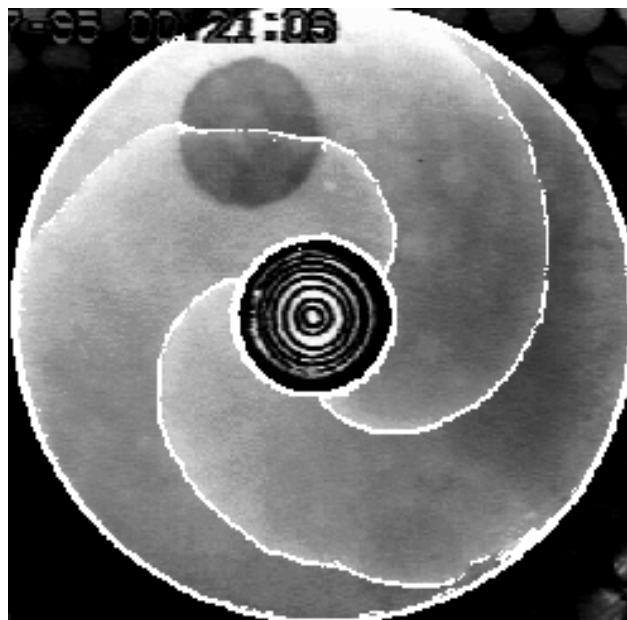


Figure 29. Refraction of a pinwheel front on a spot of $BaSO_4$ precipitate.

The image was taken by the digitizer card of the PC and it was digitally enhanced¹⁰. The darker spot is the region where barium sulfate was precipitated inside the gelled membrane. As the waves slow down here the front is deformed in this region. The target pattern in the center was used for the exact positioning of the subsequent images.

¹⁰ An "edge detect" filter was applied on the original image, then a threshold filter was used to convert the edges and background colors to white and black followed by a manually editing to remove unnecessary edges. The resulting image was then added to the original image that now clearly shows the wavefronts and the boundaries of the membrane ring.

transport in a direction perpendicularly to the membrane, that is between the fixed catalyst in the membrane and the pool of the other BZ reagents underneath. This latter possibility was also suggested by an observation made inadvertently. An air bubble, which remained accidentally between the membrane and the BZ reagent pool, also caused a strong refraction of the wave fronts. Thus in the following we tried to block or at least modify the mass transport between the membrane and the BZ pool intentionally by placing different barriers between them.

5.4.3. Refraction of waves with a plastic foil barrier

A quadrangular piece of a polyethylene foil (thickness = 50 μm) was placed between the polysulfone membrane with the fixed catalyst and the gel containing the other BZ components. The velocity map (see section "Reconstructing the velocity map" on page 53) calculated from the results of this experiment can be seen in Figure 30. From this map it is clear that the wave velocity in membrane regions above the barrier foil is reduced considerably compared to other

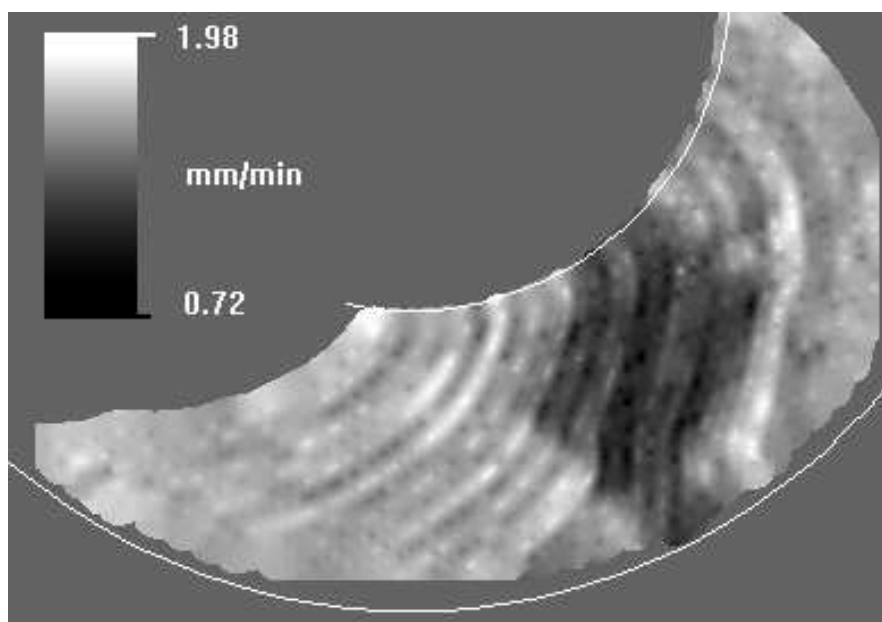


Figure 30. Velocity map of a wave refraction experiment with a plastic foil barrier membrane

The wave slows down above the quadrangular barrier foil (darker spot) because some transport processes are hindered. The picture was made with low resolution to make the wave fronts clearly visible. The barrier foil is invisible. Outer diameter of the ring shaped membrane is 40 mm, inner diameter 20 mm.

areas. Thus it can be concluded that in the present experiments it is the transversal and not the lateral mass transport controlling the wave velocity.

A next logical question is which component of the BZ reaction is responsible for the observed effect? Apparently, the transversal diffusion of this component (or components) is blocked by the barrier. There are three large groups of chemicals involved in diffusional transport here: initial components, intermediates and products of the BZ reaction. As final products are not reactive by definition, their role here can be ruled out. Thus in principle two possibilities remain. The barrier hinders

- the feeding of the membrane by the initial components of the BZ reaction from the pool underneath,
- the escape of certain inhibitory intermediates of the BZ reaction from the membrane down to the pool.

In the first case it would be the depletion of the initial components in the membrane, which would cause a slowing down of the waves in the depleted areas of the membrane. In the second case it would be the accumulation of certain inhibitory intermediates, which would decelerate the waves in the affected areas. The chemical identification of the specific component responsible for the observed slowing down of the waves was not possible in the present experiment.

On the other hand, a choice between the above two mechanisms seems possible. Our next experiments were aimed to decide whether "the key transversal transport component" (KTTC) is a starting material or an intermediate.

5.4.4. Considerations and observations suggesting that KTTC is an intermediate

Regarding first the starting materials it is the proton and the bromate concentration, which are able to affect the wave velocity. In our buffered solution any relative change in the proton concentration should be minimal, however. Thus among the starting materials only bromate could be a candidate for KTTC.

Theory and experiment agree that the wave velocity is proportional to the square root of the bromate concentration [64,65]. Therefore to decrease the velocity by a factor of two the bromate concentration should be depleted by a factor of four. This is highly improbable because the amount of the fixed catalyst is very small, thus the rate of bromate consumption should be also small. E.g. we were never able to observe the formation of CO₂ bubbles in our experiments, which would indicate higher reaction rates.

Moreover, after placing the barrier foil under the membrane, already the first wave passing through this area was slowed down and the velocity of the subsequent waves was practically the same. As it is known the rate of the reaction, and consequently the rate of the bromate consumption as well, is orders of magnitude higher in the wave front than in other places. If the bromate consumption were a crucial factor in slowing down the waves, then the depletion of bromate would take place gradually to reach its final value after the passage of several wave fronts only.

Our observations, however, show the opposite, thus we can conclude that KTTC should be an intermediate. This inhibitory intermediate (e.g., bromide) should be produced continuously not only in the wave front but also in other membrane regions characterized by a steady state where most of catalyst is in its reduced form. If the transversal diffusion is blocked by a barrier then the continuously produced inhibitor can reach a higher steady state concentration and this higher concentration can slow down the waves. E.g., Reusser and Field [66] were able to observe a slowing down of BZ waves when bromide ions were added to the system.

5.4.5. Acceleration of waves due to water evaporation

In theory, in the regions of the membrane above the barrier foil a certain depletion of the BZ reagents might occur. In the beginning of an experiment the concentrations of the reagents above the barrier should be the same as in the other regions of the membrane. This is because in a usual procedure the barrier foil is placed under the membrane only after the creation of an ordinary pinwheel. When the barrier foil is placed under the membrane, however, further transversal feed of the BZ reagents is cut, only the lateral diffusion from the perimeter of the blocked area can supply some fresh reactants. Due to a consumption of the initial components of the BZ, especially during wave propagation, a certain depletion of the reagents cannot be avoided. Nevertheless, because of the small concentration of the fixed catalyst, this depletion should be a rather minor one. To search for some signs of consumption of the BZ reagents

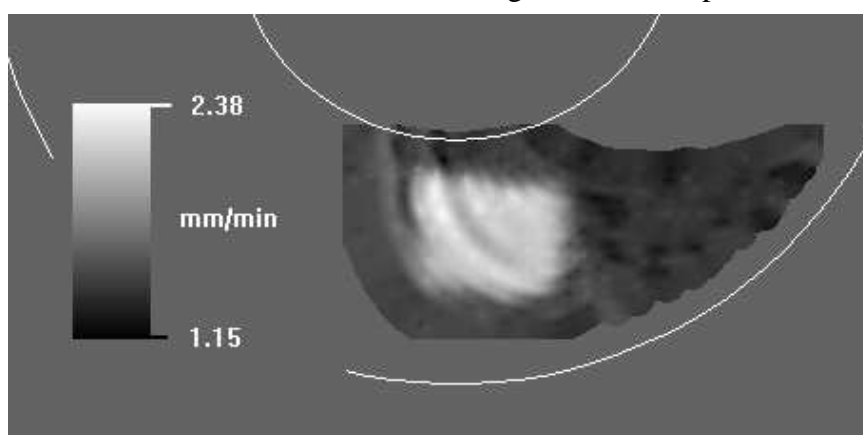


Figure 31. Acceleration of chemical waves in partially dried out regions of the membrane.

The figure shows the velocity map of an experiment made 20 minutes after the reactor window was opened. Regions over a barrier foil placed under the membrane dried out relatively more effectively than other areas: the wave velocity is considerably higher above the foil than in the surroundings. The barrier foil is invisible.

above the barrier foil, experiments lasting several hours were performed. When these experiments were made in a reactor with a closed top preventing an evaporation of water we were not able to detect any sign of even a partial exhaustion of the reagents. On the other hand, when the top was open then an inverse effect occurred: evaporation of the solvent water made the reactants above the barrier more concentrated after a while. This effect can be seen in the velocity map of Figure 31 where the wave velocity is considerably higher in membrane regions above the barrier than in the surroundings. The reactant concentrations in surface areas above the barrier become higher because the concentration changes due to the evaporation are not counterbalanced by a transversal diffusion there.

5.4.6. Refraction with Nuclepore barrier membranes

A plastic foil is a perfect barrier as it stops the transversal transport of all chemical components completely. A more gradual control of the transversal diffusion can be achieved by

applying permeable membranes as barriers. Nuclepore membrane filters are especially well suited for this purpose because of their structure. These membranes are thin polycarbonate foils (thickness $10\mu\text{m}$) containing circular holes (the diameter is $8\mu\text{m}$ in our case). As diffusion is possible only via the holes, the membrane cuts the mass transport rather effectively but not completely. The result of an experiment with Nuclepore membranes is shown in Figure 32. It

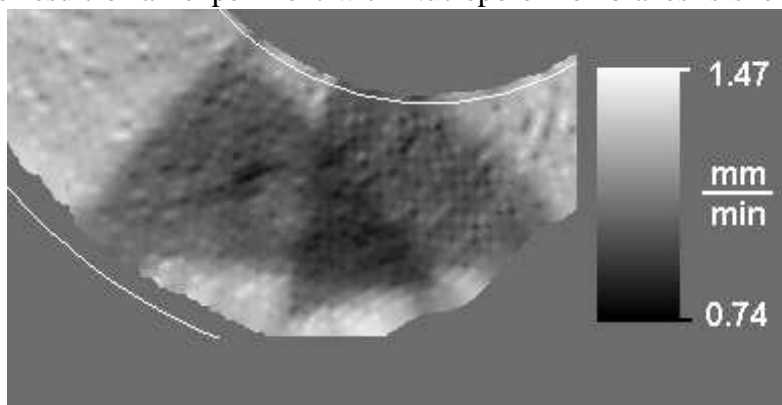


Figure 32. Additive effect of Nuclepore membranes as barrier.

Two triangle-shaped Nuclepore membrane foils were placed under the gelled membrane. The waves are slower in the region above the overlapping foils. The barrier foils are invisible.

proves that the barrier membrane is somewhat permeable. The experiment applies two Nuclepore membranes forming double barrier layers under certain regions of the membrane and single layers elsewhere. The velocity map proves that the waves are slower in membrane regions beneath of which there are two layers of the barrier membrane compared to waves in other regions with only one layer or without any barrier membrane underneath.

5.4.7. Wave refraction in an oxygen-free environment

Oxygen has a strong influence on the BZ reaction [67]. As Zhabotinsky and Epstein [62] have demonstrated a refraction of BZ waves occurs on the boundary of gel layers with different oxygen concentrations. In the present experiments the oxygen concentration differences should be less significant. Nevertheless, the applied barrier membranes would obstruct the diffusion of the dissolved oxygen as well and also of any products of its reactions.

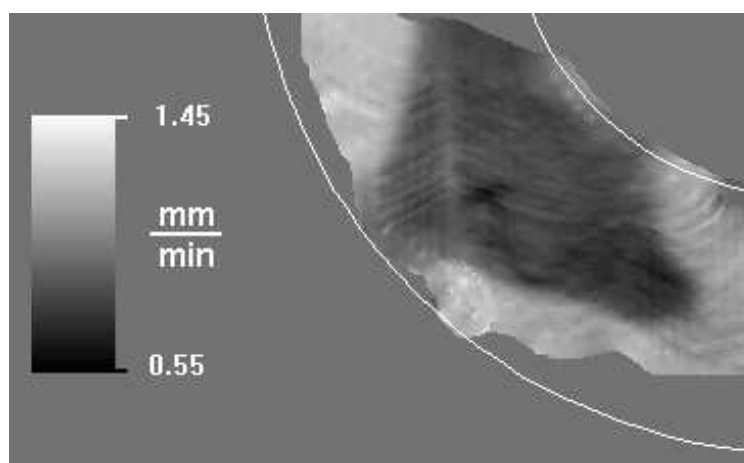


Figure 33. Effect of a nitrogen atmosphere on wave refraction.

This velocity map demonstrates that a slowing down of the waves above the barrier membrane can be observed in oxygen free atmosphere as well. The barrier foil is invisible.

Consequently an oxygen effect in our wave refraction experiments cannot be ruled out on a

theoretical basis. To prove that here it is not the oxygen, which is responsible for the wave refraction, the atmosphere in a wave refraction experiment was changed from air to nitrogen. The result (Figure 33) shows convincingly that the phenomenon of wave refraction is not caused by oxygen of the air because it can be observed in pure nitrogen as well.

5.4.8. Studies on chemical lenses¹¹

One of the most interesting properties of chemical waves is that the propagation of wave fronts obeys similar rules as the light in classical linear optics. As it was shown in the previous chapter the wave fronts refract on boundaries of membrane regions supporting different velocities; thus it is possible to repeat some optical experiments with chemical waves. Since chemical waves are orthogonal trajectories of "chemical rays" these experiments could be an analogue to experiments with "light waves".

First suppose a point-like wave source. It can be easily created by applying two small circular holes with a narrow gap between them. A pinwheel can be created around one of the holes. The

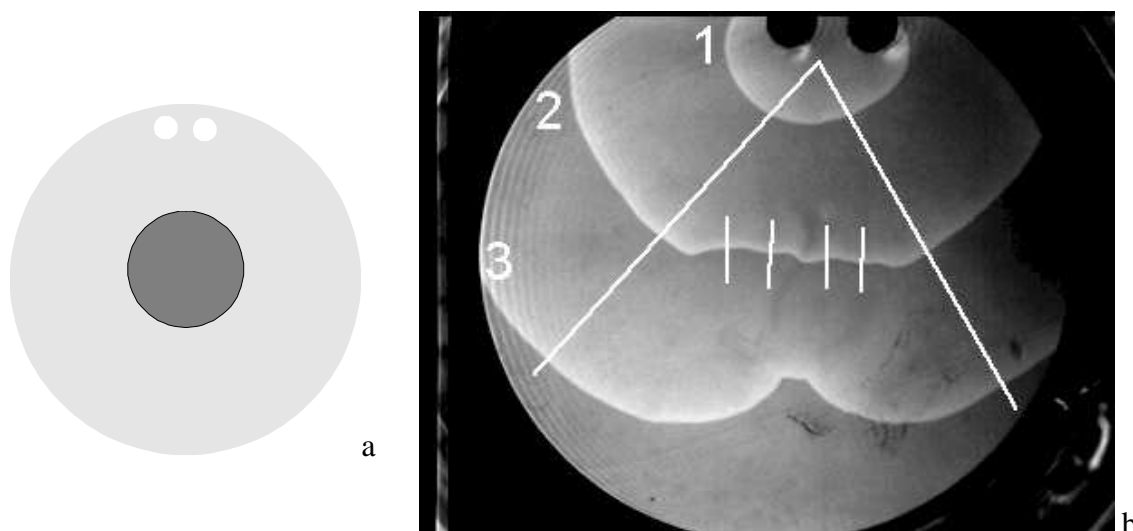


Figure 34. Parallelization of "chemical rays".

(a) Experimental arrangement. Dark gray region refers to the place of the barrier foil under the membrane (light gray). (b) Digitally enhanced image of the experiment. The rays are drawn with thin white lines. The gap between the two holes on top is the wave source.

wave front appears then in the gap from time to time as the pinwheel rotates. Figure 34 shows an experiment where the rays starting from a point-like source are parallelized by a lens. The image was taken in the Petri dish reactor using an ungelled membrane. The lens - a circular plastic foil - was placed as barrier under the center of the membrane.

The effect of refraction on planar waves was also studied. The first difficulty was that with the above method it was not possible to create planar waves reproducibly, because the geometry of the wave changes further, and the wave does not remain in the planar state (see wave 3 in

¹¹ The experiments in this chapter were carried out within the "Vertiefungsversuch" on the summer 1996 by Christian Jung and Michael Schroers.

Figure 34). Thus a new arrangement of the pinwheel and the foil was applied that was based on Snell' s law. (Snell' s law for chemical waves was verified by Zhabotinsky[2].)

For these experiments a new form of membrane was cut (Figure 35). There is a small annular region (S) on the left hand side to create a small pinwheel as wave source. Foils with different

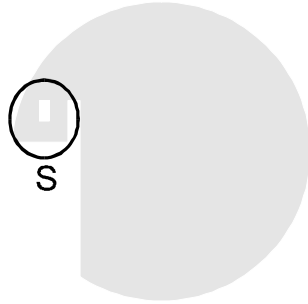


Figure 35. Membrane for refraction experiments

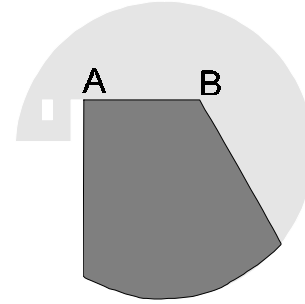


Figure 36. Foil under the membrane

geometries were placed under the membrane tightly close to the long straight side of the membrane as Figure 36 demonstrates.

Let' s recall Snell' s law to understand how it works. When a plane wave falls to a boundary between two homogeneous media of different optical properties the transmitted wave will be refracted. The angle of refraction can be calculated from Snell' s law:

$$\frac{\sin \alpha_1}{\sin \alpha_2} = \frac{v_1}{v_2} = n_{12} \quad \text{Eq. 25}$$

where the suffixes 1 and 2 refer to the different media, v is the velocity of propagation in the medium, and n_{12} is the refractive index (Figure 37, ray a).

Let' s suppose the case that the incident ray arrives in the plane of the boundary of the two media ($\alpha_1=90^\circ$) and medium 2 is optically denser than medium 1: $v_1 > v_2$ (Figure 37, ray b). Now we can write:

$$\frac{v_1}{v_2} = \frac{1}{\sin \alpha} \quad \text{Eq. 26}$$

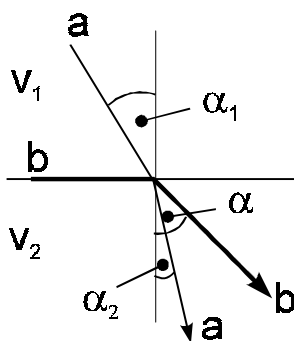


Figure 37. Snell's law

While the direction of the rays can be inverted without losing the validity of the law (ray b starts now from medium 2 with the incident angle α), the angle α in Eq. 26 can be considered as the critical angle of total reflection.

Returning to the chemical waves the pinwheel working in the small annular region in the membrane (Figure 36) sends waves that are approximately circular above the horizontal line AB . The waves hit the boundary always perpendicularly thus the "wave ray" on the boundary is identical with the boundary. That is exactly the case of Eq. 26.

Figure 38 shows the geometry of the waves entering the refractive zone at the point *A* with the angle α (analogue to Figure 37, shown by the thick arrow). The trapezoid *ABCD* refers to the slower, refractive zone with the velocity v_2 . In the "shadow zone" (between the line *e* and the vertical side *AD* of the trapezoid) the wave geometry is circular because there is only one

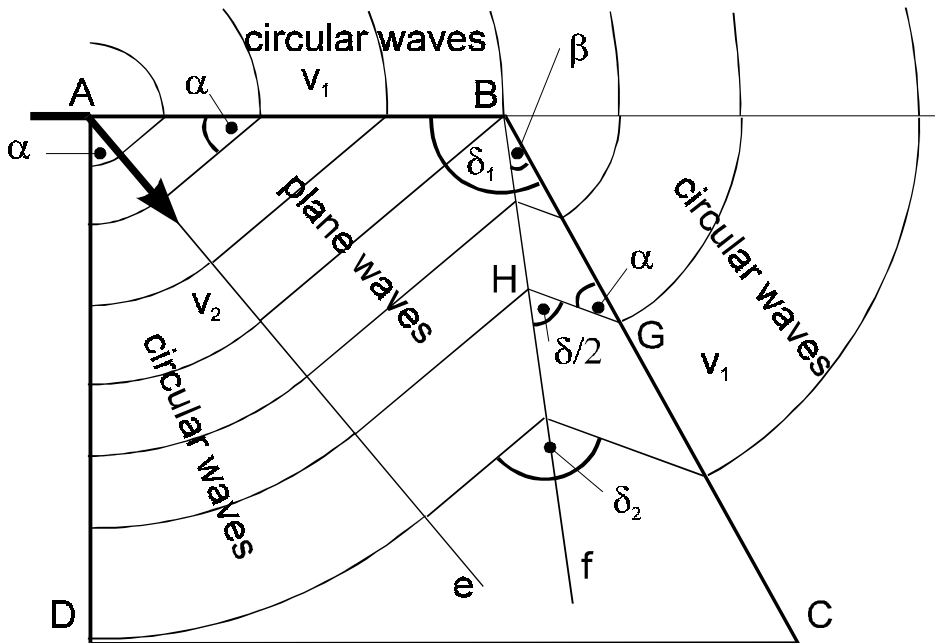


Figure 38. Geometry of chemical waves in the "refractive zone"

point-like wave source for that region, namely at point *A*. The circular waves that are propagating faster above the *AB* line than the waves in the zone *ABCD* are initiating always a new wave point (a new pseudo *A'*) propagating in the direction parallel to line *e* resulting in a zone of "plane waves".

In the zone above the *BC* line but below the lengthened *AB* line the waves are circular again, because of the only wave source point *B*. These circular waves are initiating plane waves again in the direction of α similarly to the *AB* line. The two plane wave zones are separated by the line *f*. Where exactly lies this line *f*?

Denote δ_1 the $\angle ABC$ and δ_2 the angle between the fronts of the two types of plane waves. Because δ_2 is the same angle as δ_1 rotated by α , we can write $\delta_1 = \delta_2 \equiv \delta$. Line *f* divides δ into two, equal sized angles. From the triangle *BGH* it follows that

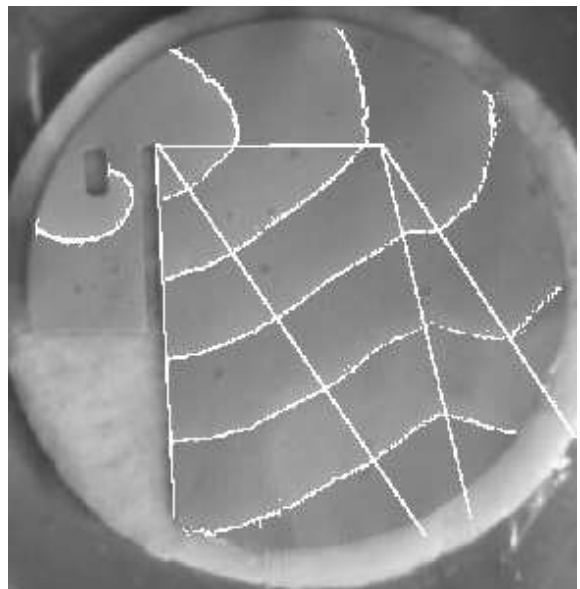


Figure 39. Creating plane waves for the lens experiments

The image was taken in a lens experiment which was carried out in the Petri dish reactor. The wave fronts were digitally enhanced (as described at Figure 29) and the lines separating the different regions of wave geometries were manually drawn.

$$\alpha + \beta = \delta / 2$$

$$\beta = \frac{\delta}{2} - \alpha$$

Eq. 27

The experiment shown in Figure 39 was taken in the Petri dish reactor. The lines e and f and the boundaries of the foil applied to create the slower zone were drawn manually. The angle α is approximately 35° , thus the refraction index of the two zones is $n_{12}=1.74$.

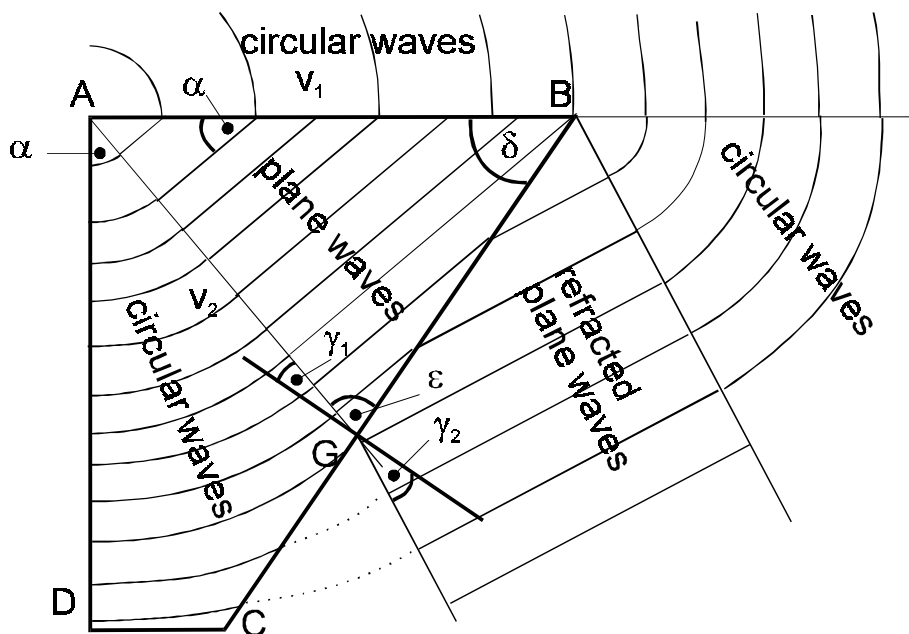


Figure 40. Creating planar waves in the faster zone

The next problem is the creation of plane waves in the faster zone. A similar arrangement to the previous one was used, but here the waves leaving the slower zone are also plane in a region as Figure 40 shows, because these waves are refracted again. This is indicated in the figure by the angles γ_1 and γ_2 at point G . The connection between the different angles is

$$90^\circ - \alpha + \delta + \epsilon = 180^\circ$$

(from the triangle ABG), thus

$$\epsilon = \alpha - \delta + 90^\circ.$$

On the other hand

$$\gamma_1 = 90^\circ - \epsilon.$$

The geometry of the dotted waves below the point G is complex, a transition from circular waves to plane waves. The experiment in Figure 41 shows the membrane arrangement and the result for creating plane waves in the faster region.

The experiment with a converging lens is shown in Figure 42. A small circular foil was put in the plane wave region of the faster zone.

A diverging lens was made by placing a circular faster region in the slower zone. A simple hole was cut in the foil applied as barrier under the membrane as Figure 43 shows. The position of the barrier foil can be seen as a light circular spot where the refraction takes place. It also indicates that in that region the chemistry is somewhat different.

These experiments can help to understand the phenomena of refraction, and are very suitable for demonstrating. Thus it is planned to construct a chemical wave kit - in cooperation with a

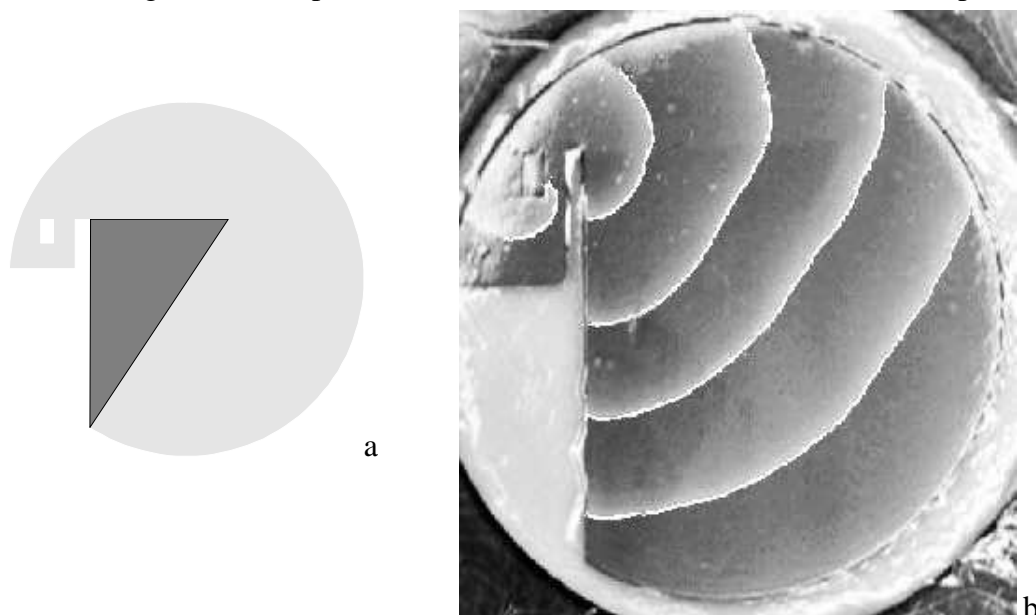


Figure 41. Creation of plane waves in the faster membrane zone.

(a) There is a barrier foil under the dark region of the membrane, thus this zone is slow. (b) As the experiment shows the waves remain plane also in a region of the faster zone.

The sparkling of the membrane is caused by a covering foil that was applied to prevent evaporation.

membrane selling firm - that includes all the necessary chemicals for carrying out these wave and lens experiments. This kit will be offered to educational institutes (schools, highschools, universities) to support teaching in linear optics. Of course, the present experiments must be refined further.

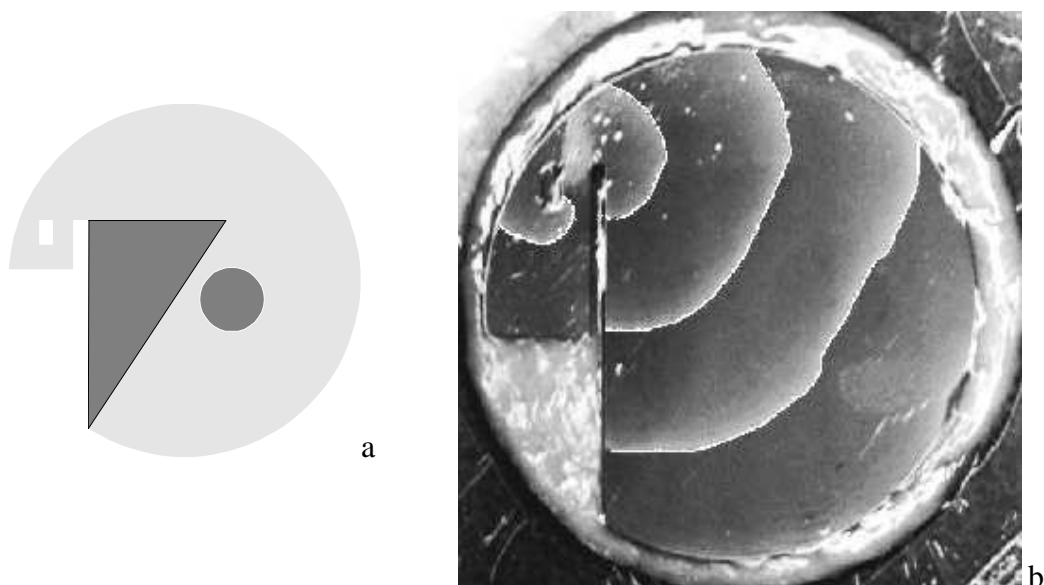


Figure 42. Plane waves are refracting on a converging lens in the faster zone.

A covering foil was also applied here, that caused sparkling. The image was slightly modified digitally to enhance the contrast of the wave fronts as it was described previously.

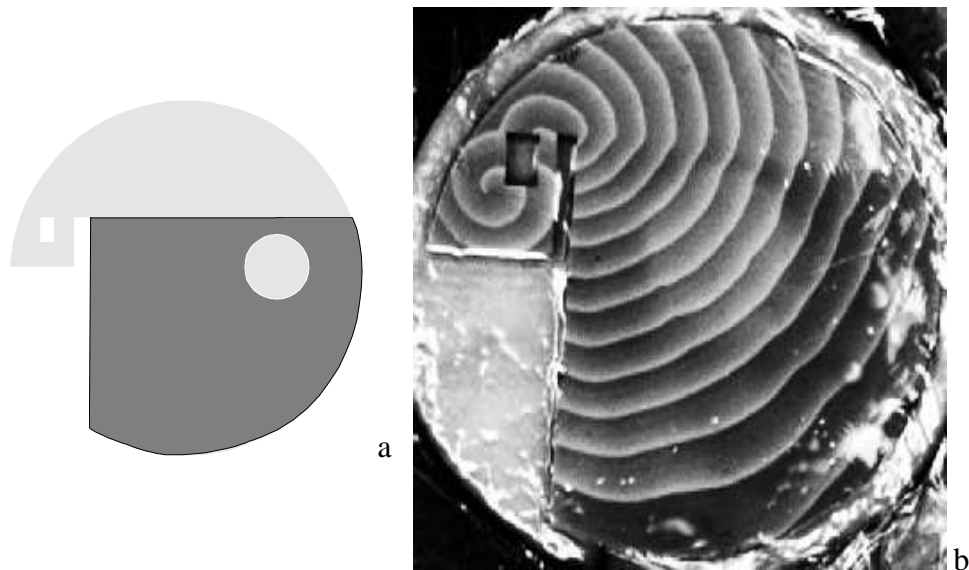


Figure 43. Plane waves are refracting on a diverging lens.

The membrane was covered with a thin foil to prevent evaporation, that's why it is shining on the right hand side. The pinwheel as wave source turned accidentally into a spiral that sends the waves more frequently, but it does not disturb the experiment itself. The contrast of the image was increased digitally, but the wave fronts were not enhanced as on previous pictures.

5.5. The geometry of chemical waves in nonuniform membrane rings

In recent models of atrial flutter [16,17] it is assumed that the obstacle is a "combined functional-anatomical conduction block" which is surrounded by a region, where the wave propagation is slower than in the other parts of the atrium. Presently the critical reentrant pathway is unclear. Either it is the slow circuit near the combined obstacle or the fast one far from it [16]. Thus our aim here is to generalize the Wiener-Rosenblueth theory for a nonuniform excitable medium, where the central obstacle is surrounded by an inner slow and an outer fast region. Then we want to compare the theoretical predictions with chemical wave experiments. The generalized theory makes it possible to predict the shape of wave fronts for such cases in terms of geometrical concepts like *caustics* [68], *minimal loops*, *involutives* and *reverse involutes*.

5.5.1. Generalization of the Wiener-Rosenblueth theory

The basic concepts of the present geometric theory are the fronts and the rays, which are orthogonal to each other [69]. The advantage of starting with rays is that Fermat's principle (the wave propagation time is a minimum) can be used.

Homogeneous case

First, let us briefly reconsider the case of a homogeneous ($v=\text{const.}$), annular membrane analyzed by Wiener and Rosenblueth (Figure 44). The inner disc is an obstacle in which the wave does not propagate ($v=0$). Figure 44 shows the evolution of a wave front. There are two

different types of rays starting from the points of the initial wave front F_0 : The rays of type a start at point Q_{10} , go for a while along the inner circle, and depart tangentially. The rays of this type generate the inner part of the wave front, which is an involute of the inner circle. The rays of type b start from the interval (Q_{10}, Q_{20}) . These rays are line segments perpendicular to F_0 . They generate the outer part of the front which is parallel to F_0 . The stationary wave profile is the involute of the inner circle, because the rays of type b propagate in a fixed direction, and hence, they are “transient”, in other words the front parts generated by them are finally swept out. The stationary front, which preserves its shape during rotation is produced by Q_{10} . Pictorially, we can imagine a *leading point* which starts from the point Q_{10} , runs around the inner circle, and drags the front.

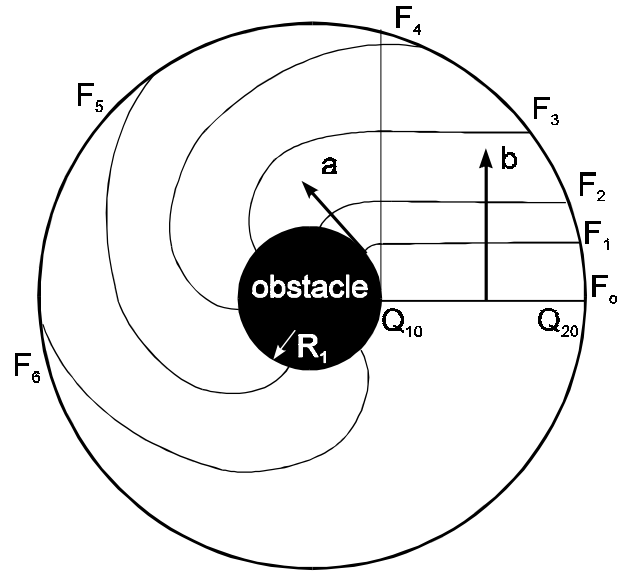


Figure 44. Evolution of a wave front in an annular homogeneous region

Inhomogeneous case, $\omega_1 < \omega_2$ ($v_1 \ll v_2$)

Next let us regard Figures 45 and 46. Here the obstacle is surrounded by a slower (wave velocity= v_1) inner and a faster (wave velocity= v_2) outer ring. The borderline between them will be referred to as interfacial boundary. The radius of the obstacle is R_1 , the outer radius of the slower region is R_2 . An angular velocity can be assigned to the obstacle and to the interfacial boundary as well:

$$\omega_1 = v_1/R_1, \quad \omega_2 = v_2/R_2$$

$$\frac{R_2 v_1}{R_1 v_2} = \frac{\omega_1}{\omega_2}$$

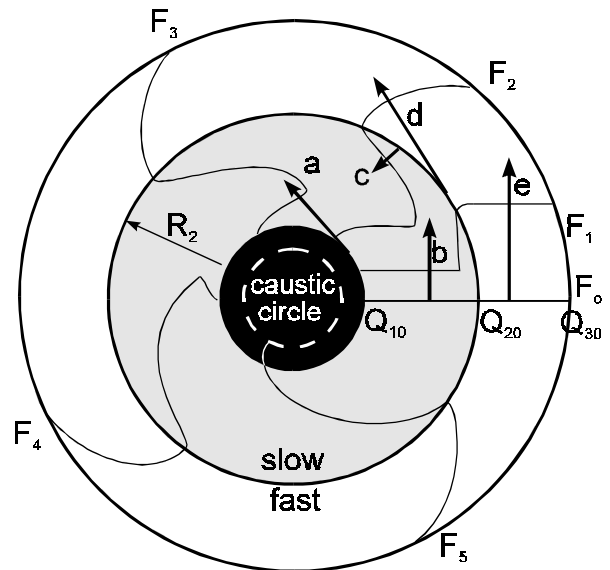


Figure 45. Wave propagation in a two ring system, case $\omega_1 < \omega_2$.

The shape of the front is determined by the *minimal loop*, a closed curve surrounding the central obstacle to which the propagation time is minimal. Let us consider the case when $\omega_1 < \omega_2$ ($v_1 \ll v_2$, the very small value of v_1 overcompensates the bigger R_2 , $\omega_1/\omega_2 < 1$), the interfacial boundary is the minimal loop (Figure 45). There are five different types of rays starting from the points of the initial front F_0 : The ray a starts at point Q_{10} , goes for a while along the inner circle, and departs tangentially. The rays of this type generate the inner part of the wave front, which is

an involute of the inner circle. The ray b starts from the interval (Q_{10}, Q_{20}) , it is a line segment perpendicular to F_0 . The rays of this type generate the next part of the front which is a line parallel to F_0 . The ray c starts from Q_{20} (at the interfacial boundary), goes along the interfacial boundary for a while, and departs inward with the critical angle of total reflection

$$\sin \alpha_{cr} = v_1/v_2 .$$

These rays are tangents of the caustic¹² (dashed circle inside the obstacle), whose radius is

$$C_1 = R_2 \sin \alpha_{cr} = R_2 v_1/v_2 = R_1 \omega_1/\omega_2 .$$

The part of the front generated by these rays is a part of a *reverse involute* (mirror image of an involute) of the caustic. The ray d starts from Q_{20} , goes along the interfacial boundary for a while, and departs from it tangentially outward. The corresponding part of the front is a part of an involute of the interfacial boundary. The straight ray e starts from a point of the interval (Q_{20}, Q_{30}) , it is perpendicular to F_0 . The rays of this type generate the outermost part of the front, which is a line parallel to F_0 .

The rays of the types b and e propagate in a fixed direction, and hence, they are “transient”, in the same sense as previously. The innermost front part is produced by the leading point starting from the point Q_{10} , and running around the innermost circle with the angular velocity ω_1 . The parts of the front belonging to the rays of the type c and d are produced by an other leading point starting from Q_{20} and running around the interfacial boundary with the angular velocity ω_2 . The result of the *competition* of the two leading points will determine the asymptotic shape of the front. In the present case the outer leading point wins, that is, its domain will survive, and the *asymptotic front* (F_5) consists of a reverse involute of the circle C_1 and a (forward) involute of the circle R_2 .

Inhomogeneous case, $\omega_1 > \omega_2$ ($v_1 < v_2$)

Finally let us consider the case when $\omega_1 > \omega_2$, ($v_1 < v_2$, the small value of v_1 can not overcompensate the much bigger R_2 , $\omega_1/\omega_2 > 1$) the minimal loop is the obstacle (Figure 46). First the front evolution is qualitatively similar to the previous case. The difference becomes essential only when the front domains of the two leading points meet. Now it is the inner point winning the competition, its domain will survive. That means that the asymptotic front (F_5) is determined by the rays of the type a . When the ray a reaches the interfacial boundary refracts according to Snell’s law:

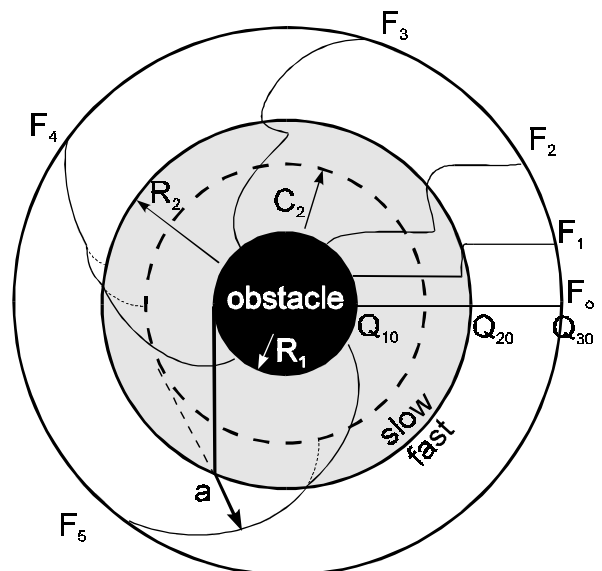


Figure 46. Wave propagation in a two ring system, case $\omega_1 > \omega_2$

¹² The caustic is the envelope of the rays. For example in the case of the involute of a circle in a homogeneous medium the caustic is exactly the circle. The rays to the points of the involute are tangents of the circle and the envelope of these tangents is the circle itself.

$$\sin\alpha_2 = \sin\alpha_1 \cdot v_2/v_1 = (R_1/R_2) \cdot (v_2/v_1) = \omega_2/\omega_1.$$

The family of these refracted rays determines the caustic (dashed circle with radius $C_2 = R_2 \sin\alpha_2$). The outer part of the asymptotic front will be a part of the involute of this caustic.

The concepts of stationary wave profile, leading point, minimal loop and caustic - introduced above - can be also applied in the case of an inhomogeneous medium with continuously varying velocity. However, the construction of the wave fronts is not so simple, since the rays are not straight lines in a continuously inhomogeneous medium.

5.5.2. Experimental verification of the generalized Wiener-Rosenblueth theory

Figure 47 shows a three armed “chemical pinwheel”: three wave fronts rotating counterclockwise in a homogeneous membrane ring. The central obstacle, a circular hole, was cut into the membrane before its dyeing. According to the original Wiener-Rosenblueth theory the wave fronts should be involutes of the hole. The experimental shape is very close to this prediction except the fronts are involutes of a somewhat smaller circle as can be seen in Figure 47. (Compare with Figure 27, where the involutes were drawn directly to the hole.) The reason for this small deviation is an

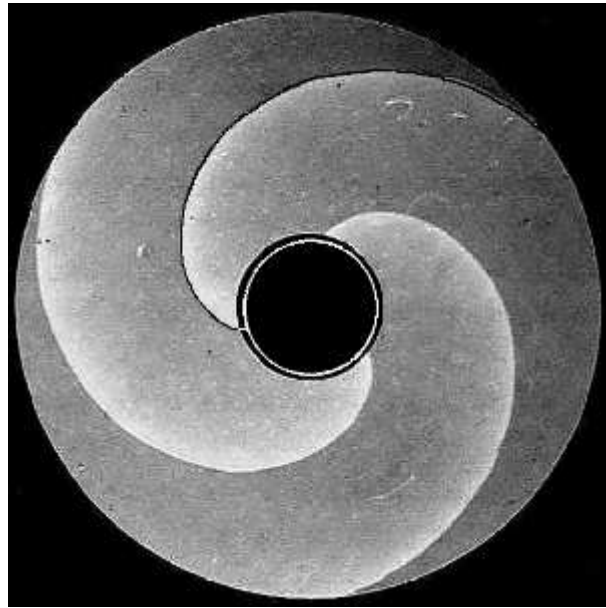


Figure 47. A three armed pinwheel in a uniform membrane ring

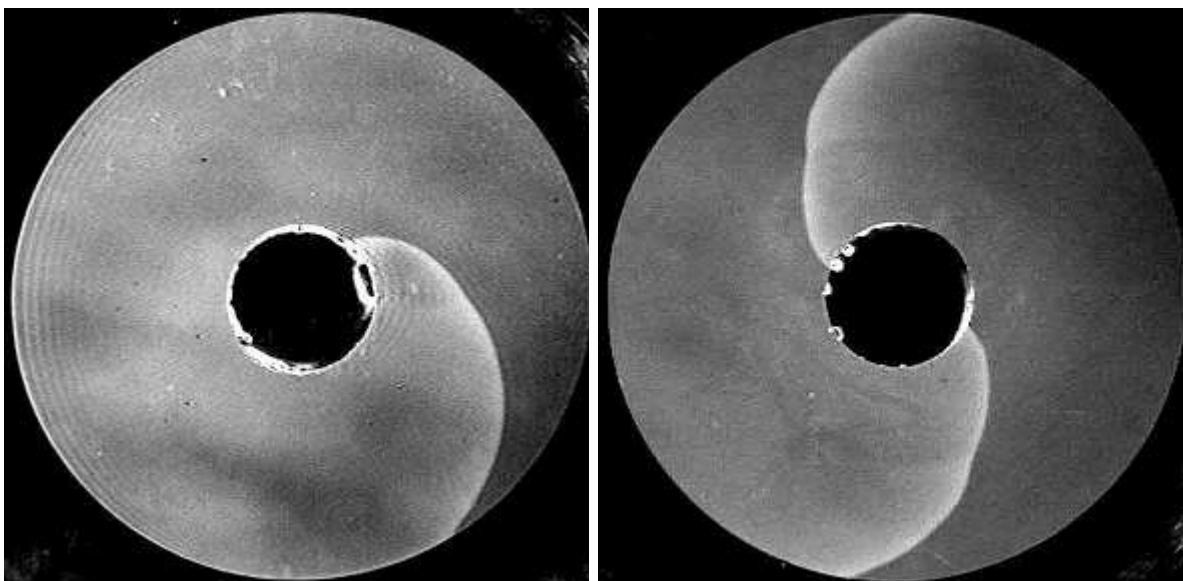


Figure 48. A one and a two armed pinwheels in nonuniform membrane rings

The geometry of the wave fronts are similar to that described in Figure 46, $\omega_1 > \omega_2$.

inhomogeneity caused by the cutting of the membrane. Due to the cutting the wave velocity at the inner rim of the membrane is a little bit higher than in the other homogeneous regions¹³. According to the generalized Wiener-Rosenblueth theory discussed here, the wave fronts should be involutes of a caustic in this case. Moreover, that caustic should be a circle now with a radius smaller than that of the obstacle. Thus the generalized theory is in a good agreement with the observations displayed in Figure 47. This experiment was made with a uniform membrane for comparison.

In all other experiments the membrane ring was nonuniform. This was achieved by placing a disc of a 10 μm thick nonporous polyethylene foil between the membrane and the supporting gel layer. The position of the foil disc with respect to the annular membrane is concentric. Consequently there is an inner ring in the membrane with lower and an outer ring with higher wave velocities. Figures 48 and 49 show the effect of this inhomogeneity on the wave front in the case of one, two and three armed pinwheels respectively. To eliminate transient effects all the pictures were recorded at least 4-6 hours after the start of the experiment and the stable wave fronts were maintained for 12-24 hours. As can be seen, increasing the number of arms has a

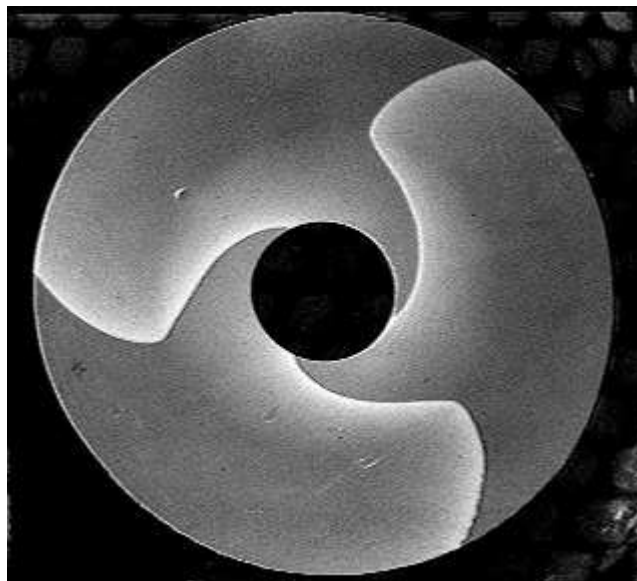


Figure 49. A three armed pinwheel in a nonuniform membrane ring

The geometry of the wave fronts are similar to that described in Figure 45, $\omega_1 < \omega_2$.

strong effect on the asymptotic shape of the waves. There is a break on the wave fronts in all the three cases at the perimeter of the otherwise invisible foil disc. This break is slight, however, in the case of the one- and two-armed pinwheels but it is very pronounced in the three-armed case.

A qualitative explanation for this abrupt change is the following. Increasing the number of arms decreases the wave velocity in the inner region because the steady state concentration of the intermediates increases there with more arms. This gradual decrease of velocity can cause an abrupt change in the wave shape, however, when the wave velocity on the perimeter of the obstacle reaches a critical value. While above this critical value the minimal loop is the perimeter of the obstacle ($\omega_1 > \omega_2$, like in Figure 46), it is the perimeter of the foil, which plays the role of the minimal loop below the critical value ($\omega_1 < \omega_2$, see Figure 45).

¹³ We observed that waves propagate slower in gelled than in gel free membranes. Probably this is caused by a Hofmann-degradation type reaction between the polyacrylamide gel matrix and hypobromous acid, a process generating bromide and slowing down the waves. Cutting the membrane can produce gel free edges with higher velocities there.

Figures 50-53 present a quantitative evaluation of the wave velocities and the front shapes in the case of the two and a four-armed¹⁴ pinwheel. A grayscale “velocity map” of the membrane ring is given in Figure 50 for the case of the two armed pinwheel. Slow zones are shown in various shades of dark gray, while fast regions are colored light gray. The radial velocity profile is given in Figure 51. Analogous diagrams for a four armed pinwheel are shown in Figures 52 and 53. White fronts on the gray-shaded background in Figures 50 and 52 are snapshots of the experimental wave fronts. The local velocity was determined by measuring the displacement of the front perpendicularly to it (solid curves in Figures 51 and 53). White fronts against the lightgray background in Figures 50 and 52 are theoretical wave fronts calculated by a two velocity model (assuming a stepwise radial velocity profile). In Figure 50 these theoretical wave fronts start as involutes of the inner hole and at the perimeter of the barrier foil (thick lightgray circle), and continue as involutes of a caustic (dashed circle between the perimeter of the foil and the hole). The radius of the caustic is

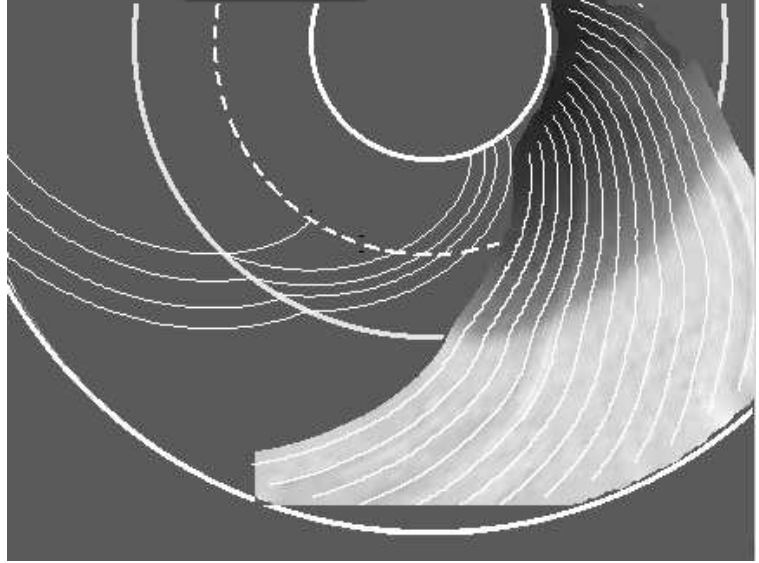


Figure 50. Velocity map of a two armed pinwheel with measured and calculated wave front geometries in a nonuniform membrane ring

Thin white lines on the uniform gray background show calculated wave fronts, while the lines on the grayscale velocity map show the observed wave fronts. Darker shades of gray refer to slower regions on the velocity map.

perpendicularly to it (solid curves in Figures 51 and 53). White fronts against the lightgray background in Figures 50 and 52 are theoretical wave fronts calculated by a two velocity model (assuming a stepwise radial velocity profile). In Figure 50 these theoretical wave fronts start as involutes of the inner hole and at the perimeter of the barrier foil (thick lightgray circle), and continue as involutes of a caustic (dashed circle between the perimeter of the foil and the hole). The radius of the caustic is

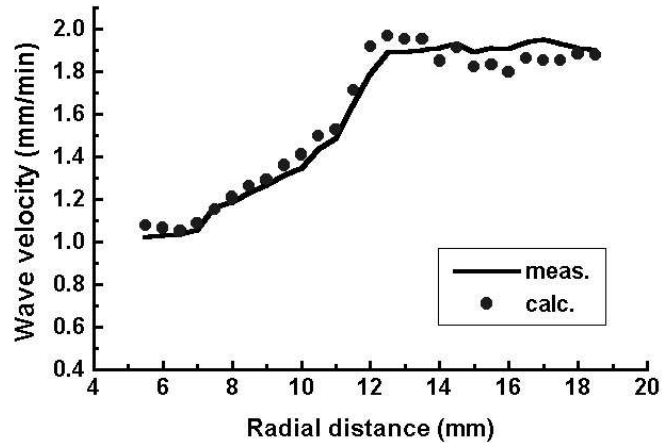


Figure 51. The radial velocity profile of the two armed pinwheel

Dots were calculated from the geometry of the measured wave fronts, the solid line is measurement from Figure 50.

$$C_2 = R_1 v_{\max} / v_{\min} = 9 \text{ mm}$$

where $v_{\max} \cong 1.8$ and $v_{\min} \cong 1.0$ mm/min according to Figure 51. In Figure 52 the theoretical wave fronts start as involutes of a caustic (dashed circle inside the hole) and continue as involutes of the thick lightgray circle beyond the rim of the foil. In this case the radius of the caustic is

¹⁴ Here a four armed pinwheel was chosen instead of the three armed one, because in the three armed case the caustic curve lies almost on the circle of the obstacle, while in the four armed case the caustic curve is better separated.

$$C_1 = R_2 v_{\min} / v_{\max} = 4 \text{ mm}$$

where $v_{\max} \approx 1.8$ and $v_{\min} \approx 0.6$ mm/min according to Figure 53.

Comparing the experimental and the theoretical wave fronts the qualitative agreement is good but there are also some differences. This is due to the fact that the velocity profile is not a stepwise but it is a continuous function (due to the radial diffusion of the intermediates from the zone above the foil their concentrations, together with their ability to slow down the waves, decrease to zero gradually and not abruptly toward the edge of the foil). Applying the theory presented here the shape of the waves can be calculated from the

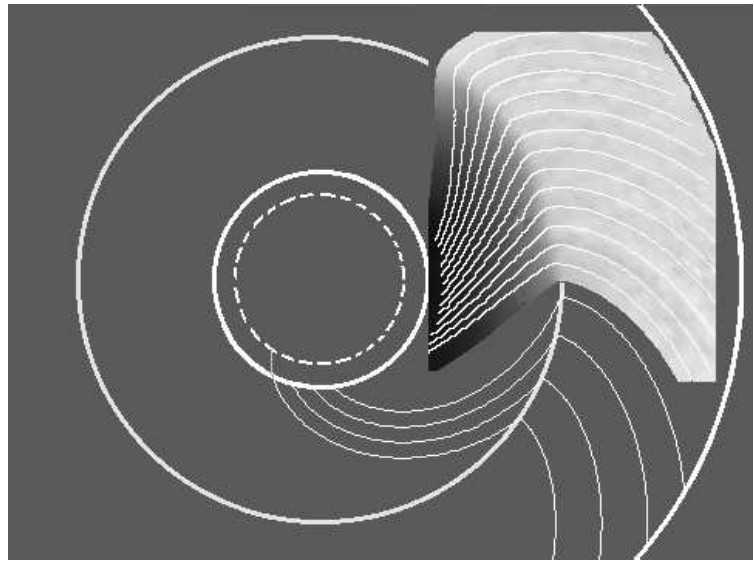


Figure 52. Velocity map of a four armed pinwheel in a nonuniform membrane ring

Thin white lines on the uniform gray background show calculated wave fronts, while the lines on the grayscale velocity map show the observed wave fronts. Darker shades of gray refer to slower regions on the velocity map.

measured $v=v(r)$ function or vice versa. To illustrate this (theory and details see in the sections beginning on page 51 and page 59) the velocity profile from the geometry of the wave fronts was calculated in both cases (dots in Figures 51 and 53). As can be seen, the agreement between the measured and the calculated values is good.

Our experimental and theoretical results might help to investigate the critical reentrant pathway (minimal loop) in atrial flutter. The shape of the wave front shows the location of the leading point that moves on the minimal loop. Furthermore, changing some parameters slowly, abrupt changes in the position of the minimal

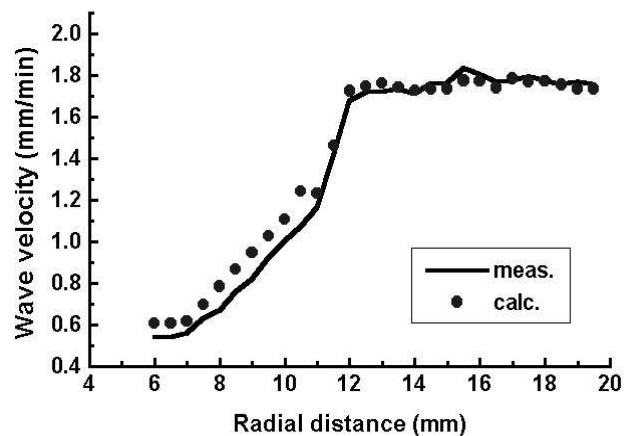


Figure 53. Radial velocity profile of the four armed pinwheel

Dots were calculated from the geometry of the measured wave fronts, the solid line is measurement from Figure 52.

loop and shape of the wave are possible but these radical changes do not have an essential impact on the circulation time.

5.5.3. Connection between front shape and wave velocity

Let' s consider a rotating wave front (constant asymptotic shape) in a nonuniform annular region (Figure 54). The velocity of the front on the minimal loop is v_m and its direction is always perpendicular to its radius r_m thus the angular velocity is

$$\omega = v_m / r_m$$

At a point $P(r, \phi)$ the velocity of the wave front v_r (real velocity) is perpendicular to the wave

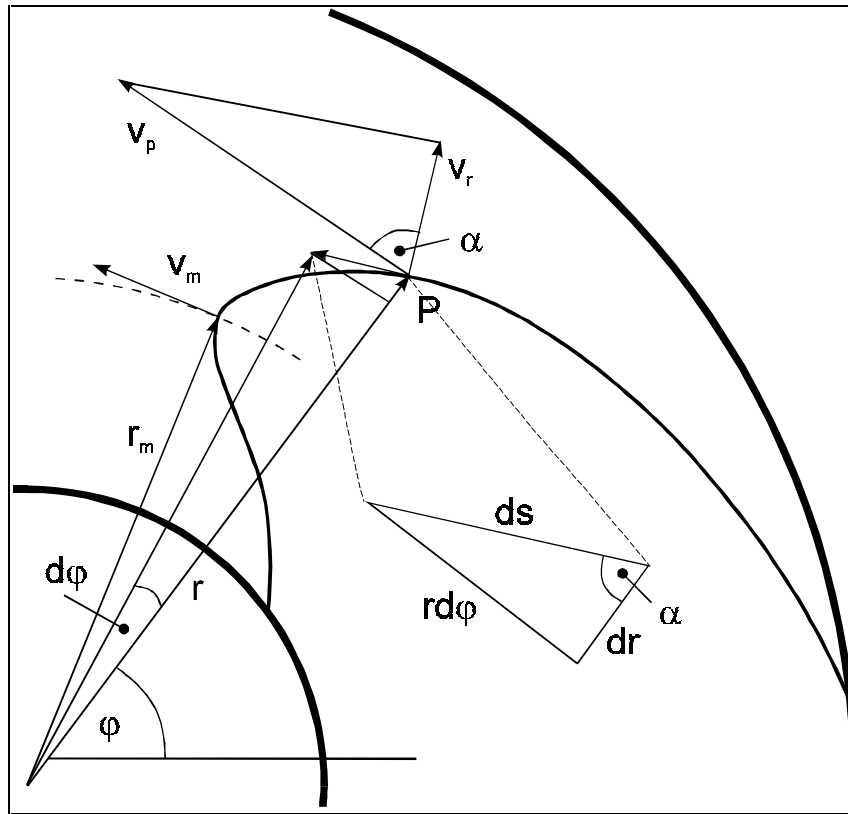


Figure 54. Connection between wave shape and velocity in a nonuniform annular region

front (but not to the radius any more). However, a velocity v_p (virtual velocity) can be defined from the rotational movement, that is perpendicular to the radius:

$$v_p = \omega r,$$

because the angular velocity ω is uniform along the whole wave front. v_p and v_r are only equal on the minimal loop, in all other points v_r is a projection of v_p . Denote α the angle between v_p and v_r . Now we can write:

$$\cos \alpha = \frac{v_r}{v_p} = \frac{v_r}{r\omega} = \frac{v_r}{v_m} \cdot \frac{r_m}{r} = n_r \frac{r_m}{r}$$

Eq. 28

where n_r is the refractive index.

Let' s move infinitesimally along the wave front tangentially (ds) (see enlarged part in Figure 54). The radial component of this movement is dr and the tangential component is $r \cdot d\phi$. Writing the Pythagoras theorem for this triangle results in:

$$ds^2 = (r d\varphi)^2 + (dr)^2 \quad \text{Eq. 29}$$

On the other hand, we can write:

$$\cos \alpha = \frac{dr}{ds} \quad \text{Eq. 30}$$

Combining the equations 29 and 30 results in:

$$\cos \alpha = \frac{dr}{\sqrt{(r d\varphi)^2 + dr^2}} = \frac{1}{\sqrt{1 + r^2 \left(\frac{d\varphi}{dr}\right)^2}} \quad \text{Eq. 31}$$

Finally, let's replace $\cos \alpha$ from Eq.28:

$$\boxed{n_r = \frac{r}{r_m} \sqrt{1 + r^2 \left(\frac{d\varphi}{dr}\right)^2}} \quad \text{Eq. 32}$$

Or, in an other form:

$$d\varphi = \frac{dr}{r} \sqrt{\left(n_r \frac{r_m}{r}\right)^2 - 1} \quad \text{Eq. 33}$$

If the function $r=r(\varphi)$ is known from the measurements the radial velocity profile can be calculated from Eq. 32. On the other hand, Eq. 33 can be integrated numerically if the radial velocity profile n_r is known; then the shape of the wave front $r=r(\varphi)$ is obtained.

6. Reconstructing the Velocity Map

Nowadays chemical wave experiments are evaluated mostly by digital image processing. The literature describes several methods how to apply video- and pattern recognition techniques [70,71], however, there are no standards. Therefore, we developed a method of our own to satisfy our requirements.

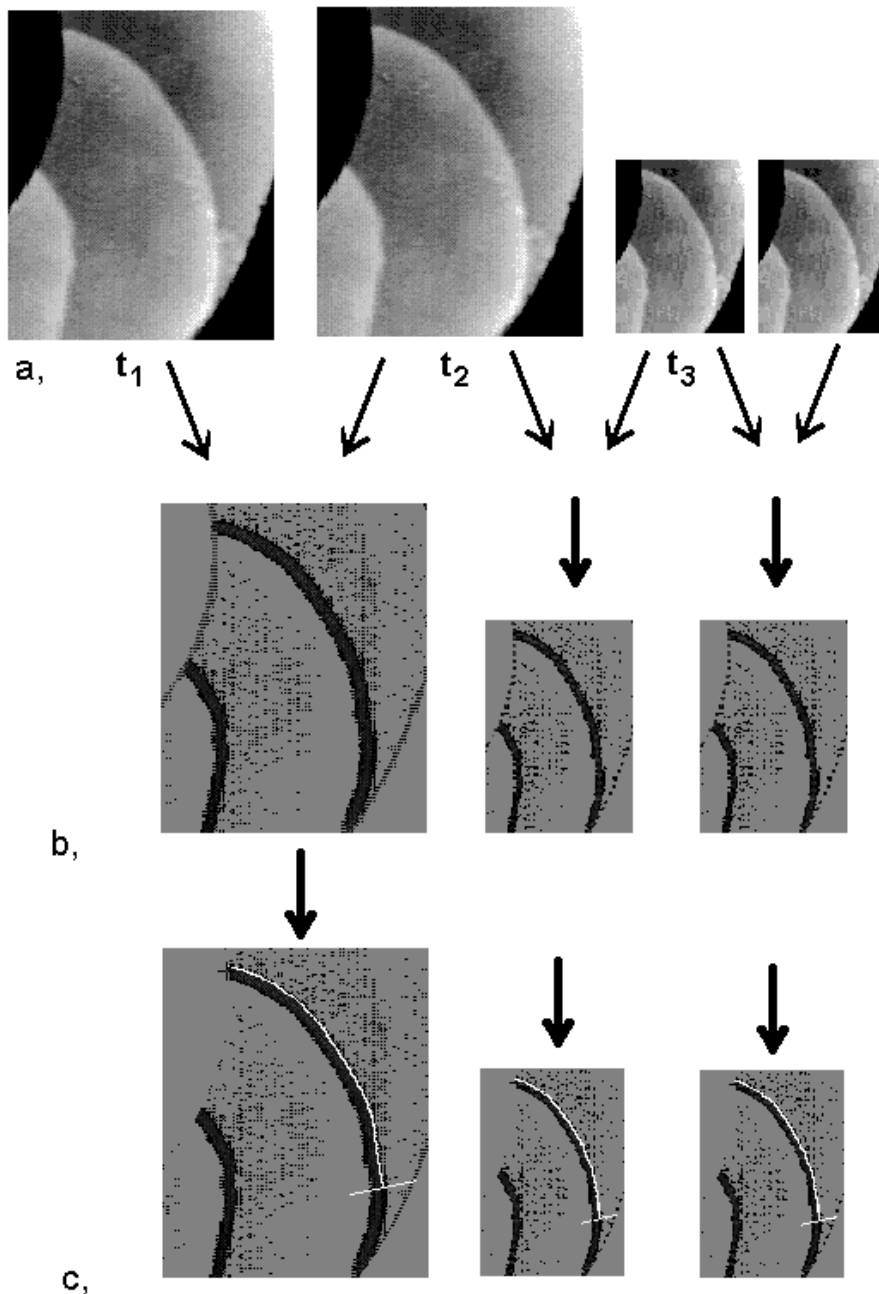


Figure 55. Subtraction of images.

(a) Original images. (b) Subtracted images. (c) Localization of wave fronts on each image.

We started to develop an image processing program on a Pentium 90 PC in Turbo Pascal 6.0, but it turned out soon, that this was not efficient enough, because neither our frame grabber card nor the DOS operating system satisfied our requirements of image processing with high accuracy. So we changed to a Silicon Graphics Indy workstation and implemented almost the same algorithm which had already worked on the PC. Silicon Graphics workstations are optimized especially for graphical tasks; they contain an integrated development environment supporting the programming of applications. Our image processing program was developed in C++ using the ViewKit and ImageVision libraries; it has a Motif user interface¹⁵ that highly simplifies the interaction with the user.

6.1. *Capturing images*

The camera we used was a Hamamatsu CCD C3077 with different objectives. It was connected to a Mitsubishi HS-5300 video recorder and through a video amplifier (ELW VÜB 7000) to the workstation. As capturing program a UNIX C-shell script was used. The script evaluated the command line options, called the vidtomem program to read the image from the camera, converted the captured images to grayscale and saved a catalog file with the names of the images and the time of capturing for later evaluation. The script is shown in Appendix D (page 82). Every ten seconds a picture (size of 768x576 pixels) was taken. Usually 40 pictures were needed for one data set and they were stored in JPEG (Joint Photographic Expert Group) format to save disk space.

6.2. *Subtraction and contrast enhancement of images*

To focus on the moving wave fronts and to eliminate any interference caused by other steady patterns subsequent images were subtracted (Figure 55a,b). Negative values in the subtracted image were converted to zero. All the fixed parts of the image (reactor parts, membrane edge, inhomogeneous illumination or small wrinkles on the covering foil) disappear and only gray levels corresponding to the propagating wave fronts remain. Next, to enhance the contrast a linear LUT filter¹⁶ was applied. Furthermore, to smooth the image (e.g. eliminate the sharp

¹⁵ Motif is a widely-used graphical user interface for UNIX workstations running with the X-Window system. It was developed by the Open Software Foundation (OSF). Motif simplifies not only the programming, but also the interaction between user and application. The user supplies any input by manipulating the screen representations of different objects (menus, buttons, sliders, etc.) with the pointer, the keyboard, or both.

¹⁶ LUT (LookUp Table) attributes a new output value to an input value corresponding to a given table. A table with two configurable parameters (a,b) was applied:

Input value (x)	Output value (y)
$x < a; x > b$	$y = 0$
$a < x < b$	$y = 256 * (x - a) / (b - a)$ (Linear interpolation between 0 and 256)

(Usual parameter values were: $a = 6 - 8$; $b = 35 - 50$)

edges) we used a blur filter¹⁷. The latter is necessary because the algorithm locating the wave fronts gives a better performance with smoothed images than with very sharp ones.

6.3. Wave front determination

It turned out very soon during the program development, that the accuracy of velocity calculation is very low if distances measured between wave fronts were calculated from pixel coordinates. Though it was possible to improve the accuracy a bit by changing the image capturing parameters (like zooming the image or changing the frequency of capturing), the calculated velocity maps were always striped because of the regularity of the pixel lattice. The measured distances involved a rather big statistical error that clearly originated from the low resolution of the images: there are only integer coordinate numbers of pixels. Therefore we developed an interpolation algorithm calculating distances using floating point numbers.

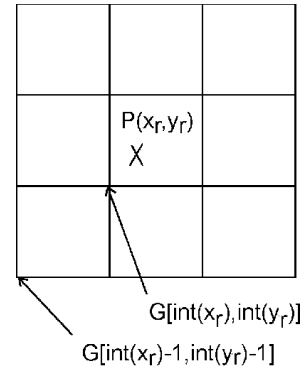


Figure 56. A point in the grid.

6.3.1. Calculation of graylevels for points with floating point coordinates

Let's suppose a 3x3 pixel grid around a point $P[x_p, y_p]$ between the pixels (Figure 56). The coordinates $[x_p, y_p]$ are floating point numbers. The left bottom corner of this grid is $G[\text{int}(x_p)-1, \text{int}(y_p)-1]$, where $\text{int}()$ is the integer function, and the graylevel is c . All measured graylevel values belong to grid points. Points between the grid points are attributed a calculated value c_{x_p, y_p} . The calculation is based on weighed averages:

$$c_{x_r, y_r} = \sum_{x=\text{int}(x_r)-1}^{\text{int}(x_r)+2} \sum_{y=\text{int}(y_r)-1}^{\text{int}(y_r)+2} w(x, y, x_r, y_r) \cdot c(x, y) \quad \text{Eq. 34}$$

where x and y are the grid coordinates, $c(x, y)$ is the graylevel of the grid point $P(x, y)$ and $w(x, y, x_p, y_p)$ is the weighing factor for the grid point $P(x, y)$:

$$w(x, y, x_r, y_r) = \frac{1}{\sum_{x=\text{int}(x_r)-1}^{\text{int}(x_r)+2} \sum_{y=\text{int}(y_r)-1}^{\text{int}(y_r)+2} \frac{1}{(x-x_r)^2 + (y-y_r)^2}} \quad \text{Eq. 35}$$

which is the weighted average of reciprocal square distances. The weighing factor calculated this way gives a fairly good, smooth interpolation between the pixels. In the case of $x=x_r$ and $y=y_r$ the program uses the measured $c_{x, y}$ value.

¹⁷ The blur (smear) filter applies a n*n matrix kernel for smoothing an image (n=3-7, ususally). The new pixel value is calculated from the old one and from the neighbour pixels in the region of n*n weighted by a Gaussian.

6.3.2. Preliminary conditions of wave front calculation

Before starting the wave front calculation some initial data about the waves must be known. The requested information is the position and size of the membrane, the type, size and position of the obstacle in the membrane (None, Circle, Polygon), one point of the wave where the calculation should start and the direction of wave propagation (Figure 57). This initialization is made by the user simply by clicking on different points in the image with the mouse (more details about this is shown in Appendix A, page 76).

6.3.3. Describing the wave front

The general problem is how to gain information about the wave fronts. The subtracted wave fronts are rather wide, that's why it is difficult to describe their position. Which points of the broad line characterize the wave front itself? Curve fitting is probably not a good idea, because it would smooth the details of the geometry that we'd like to measure.

The wave front geometry can be very complex, it cannot be defined either as a function of the radius $f(r)$ or a function of the coordinates $f(x,y)$, but a parameterized curve $X(k)$ and $Y(k)$ describes the fronts well even in complicated cases. The parameter k is the serial number of the points subsequently found on the wave front.

Let's extend this definition: the serial number can be a floating point number. It is somewhat difficult to imagine a serial number with a floating point number, but you can suppose this k as a physical parameter, e.g. distance or an "imaginary time" if we imagine a point moving with a constant velocity between two points of the wave front. It means we will start at time $k=0$ at the beginning of the front, and we will arrive to the second point at $k=1$. A number between $k=0$ and $k=1$ means, that we are still between the two points.

Which point of the wide wave front describes physically the wave? Since we'd like to calculate velocities from two wave fronts, we need their position as accurate as it is possible. Let's see a cross section of the wave (Figure 58a). Figure 58b shows a typical curve (graylevel (c) versus position (r)). The top of the curve is rather wide and indefinite, it would be a bad choice to characterize the front by a point on the top. However, the rising part of the curve corresponding to the autocatalytic reaction front is definite¹⁸ and as we saw in the experiments it is very well reproducible.

We would like to approximate the shape of the cross section of the wave front by fitting a Gaussian:

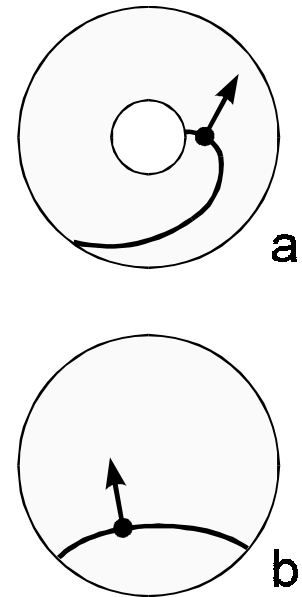


Figure 57. Direction of wave propagation

(a) with a circular obstacle; (b) without any obstacle

¹⁸ Note, that the steeper side of the curve was obtained by subtraction of images; it contains no information about the wave front location.

$$c = H \cdot \exp\left(-\frac{4 \ln 2}{W^2} \cdot (L - r)^2\right)$$

Eq. 36

where c and r refer to the grayscale (function value) and local coordinate (independent variable), while H , W , L refer to the height, width and position of the Gaussian, respectively.

How to find out the location (L), height (H) and width (W) parameters of the cross section? The cross section was divided into 80 points equidistantly. (It does not matter how many pixels

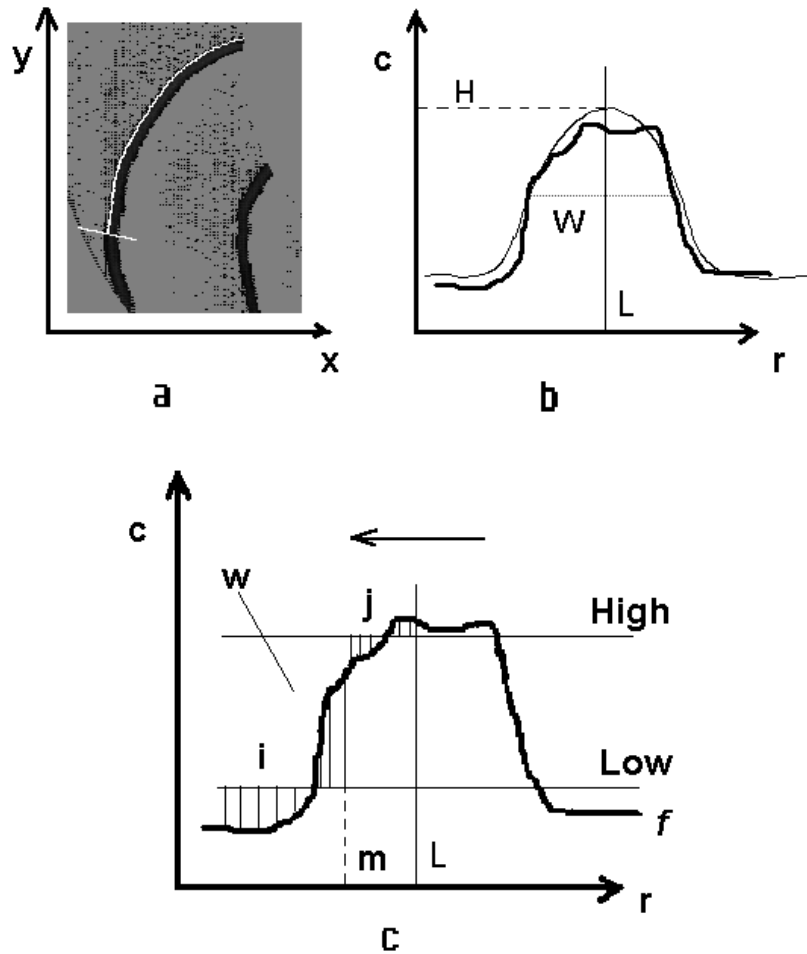


Figure 58. Which point of the wave front cross section is characteristic?

(a) A located wave front and the marking of a cross section on it. (b) Fitting a Gaussian on the cross section as first approach. (c) Calculation of the characteristic point, that represents the wave front in this cross section.

there are physically (a lot fewer) because one can interpolate with floating point coordinates between them.) The average of the five highest points gives a temporary *MAX* value. Only the points above $MAX/2$ were used for further calculation. The height of these points were logarithmed and a second order polynomial was fitted to them (Eq. 37).

$$\ln c = \ln H - \frac{4 \ln 2}{W^2} (L - r)^2$$

Eq. 37

The parameters of the Gaussian (L and W) were obtained from the parameters of the polynomial. While logarithming can cause a rather big error, the obtained H from the polynomial was not accepted, it was recalculated by fitting a new Gaussian with the already known L and W parameters on the original, not logarithmed points. This new Gaussian is still a raw approximation of the shape of the cross section and it was only supposed to determine some starting values (Figure 58b). Let's define two levels $High=0.8H$ and $Low=0.2H$ (Figure 58c). The point describing the front in this cross section was searched between these values. The range between the location L and $L-2W$ was divided into n small intervals and the following expression was calculated:

$$\min_{m=1}^n \left[\sum_{i=1}^m (c(i) - Low)^2 + \sum_{j=m+1}^n (c(j) - High)^2 \right] \quad \text{Eq. 38}$$

where $c(i)$ is the graylevel at the point i . The first part of the expression within the parenthesis describes the sum of vertical square distances between Low level and the function values $c(i)$ in the range of $1 < i < m$. Similarly, the second part describes the sum of vertical square distances between $High$ level and the function values $c(i)$ in the range of $m < i < n$. The min operator calculates the expression within the parenthesis several times changing the parameter m in the range of $1 < m < n$ and chooses the minimum of the results. The location of this minimum characterizes the position of the wave front at the given cross section (coordinates $X(k); Y(k)$). These coordinates were saved to a database for later use.

How to find the next point on the wave? The first five cross sections were determined along a line starting at the point given by the user in the left handed direction perpendicular to the wave propagation (left half arm of the wave). The places of the following cross sections were calculated from the last three points by linear regression (a numerical estimation of the tangential) and extrapolated to a distance of $\sqrt{2}$ pixels from the last point. The cross sections were always taken perpendicular to the actual tangential direction. The calculation was finished for the half arm if one of the endpoints of the cross section or the calculated characteristic point were situated either in the obstacle or out of the membrane. Then the calculation returned to the starting point and started with the right half arm in a similar way. At the end we have a set of coordinates which identify the wave front.

It is possible that the fitted Gaussian is 'inverted' (it has a minimum instead of a maximum over the cross section) giving a very bad approximation of the curve because of image contrast problems or pixel errors. In this case the algorithm ignores that cross section and searches for the next one. The probability of such errors is low (less than 1%), but it increases with decreasing image quality.

6.4. Calculation of the velocity

Two methods were developed for velocity calculations. The first one is an absolute method, based on the calculation of distances between wave fronts divided by time needed for the propagation. The second one is based only on the wave geometry, it gives the ratio of velocities.

6.4.1. The distance based method

After the determination of the wave fronts we have as many sets of $[X,Y]$ coordinates as the number of images. Denote $A[i,k]$ the k -th point with $[X,Y]$ coordinates of the set i at time $t(i)$ (Figure 59). To the point of $A[i+1, j]$ the nearest point is $A[i,k]$ on the previous set. For a raw approximation it is enough to calculate the distance between these points, but we used a more sophisticated method. A straight line was fitted to the points $A[i+1, j-1]$, $A[i+1, j]$ and $A[i+1, j+1]$ and another straight line was fitted to $A[i, k-1]$, $A[i, k]$, $A[i, k+1]$ as shown in Figure 59a. The length L of the arc through $A[i+1, j]$ (Figure 59b) was calculated (the radius R and the angle α are obtained from the data of the straight lines). Then the velocity v was calculated as $v=L/\Delta t$, where

$$\Delta t = t(i+1) - t(i)$$

is the time span between taking pictures i and $i+1$. The velocity was attributed to the point $(A[i+1, j] + A[i, k])/2$ (Figure 59c). This method was repeated for all points and all sets.

6.4.2. The geometry based method

Using Eq. 32 (on page 52) it is possible to calculate the refraction index, if the function $\varphi = \varphi(r)$ is known. Though this function is not known in its analytical form, the located points of the wave fronts can be used instead.

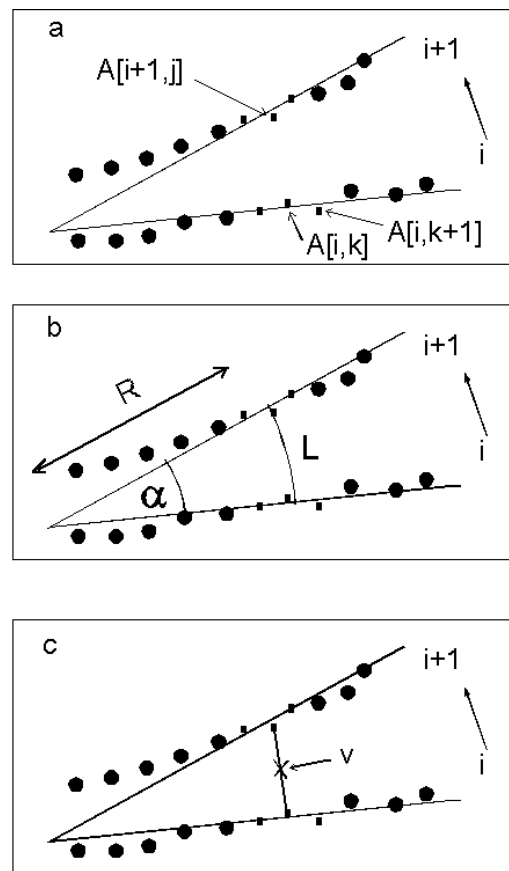


Figure 59. Calculation of distances between waves

Dots are the measured points of the wave front, the groups of small dots are the points selected for the current calculation.

The coordinates $[X, Y]$ of the wave fronts were converted to polar coordinates $[\varphi, r]$ and the derivative $d\varphi/dr$ was approximated by numerical differentiation:

$$\frac{d\varphi}{dr} = \frac{\Delta\varphi}{\Delta r} \tag{Eq. 39}$$

While the numerical differentiation is rather noisy a smoothing algorithm¹⁹ was applied to filter the resulted differential quotients. Then the refractive index was calculated from Eq.32. To compare the calculated relative radial velocity profile with the velocities calculated from the displacement of the wave fronts, the scaling factor v_m (velocity on the minimal loop) should be used. This value was taken from the absolute method as an average of some hundreds of points in the faster region. This approximation seems to be correct, because the velocity in the faster region is more or less constant (see Figures 50-53) and thus equal to the velocity on the minimal loop.

It should be also noted here, that this method can be only used if the minimal loop is well defined, and it does not change its location (its radius) during the measurements. Furthermore the obstacle (the hole) in the membrane should be a circle, because Eq. 32 is valid only in that case. In spite of this, the absolute method does not have such limitations, it can be used in all cases independently of the shape or presence of the obstacle.

6.5. Visualization of the velocity map

Our database consists of three sets of floating point values: the X and Y coordinates of a point and the velocity v . A velocity map was created by using a graylevel or an artificial color scale corresponding to the velocities.

The velocity calculation method produces only some hundreds of points (denoted as P_c , these are the points with the floating point coordinates), hence it was necessary to interpolate the pixel points of the velocity to cover the drawing area. The interpolated velocity (v_{int}) in point P is:

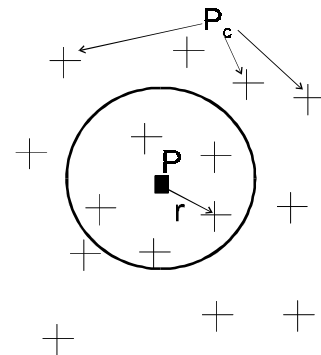


Figure 60. Calculate pixel values

$$v_{int} = \frac{\sum_j \frac{1}{r_j^2} v_j}{\sum_j \frac{1}{r_j^2}} \tag{Eq. 40}$$

where j is the index of all the points $P_{c,j}$ inside of a given circle (the radius of this circle is one of the user-definable parameters, its default value is ten pixels) around the pixel P , r_j is the distance

¹⁹ The smoothing is based on a seven-point average: the weighing factors are symmetrically arranged to the center point and they are decreasing with increasing distance from the center. The weighing factors were chosen as 0.25, 0.2, 0.12, 0.055 respectively.

between P and $P_{c,j}$, v_j is the velocity at the point $P_{c,j}$. This calculation was performed for all pixel points of the drawing area.

The ten highest and lowest velocity values of the database were averaged to $VMAX$ and $VMIN$. The velocity $VMAX$ was shown on the screen with the highest graylevel value (255, white) and $VMIN$ was shown with the lowest graylevel value (0, black). All other velocities were interpolated between 0 and 255. To print color slides the graylevel color table was changed to an artificial color table with the Corel PhotoPaint 3.0 program.

6.6. A simple method to enhance the resolution of the velocity maps

The number of the captured images can be increased by choosing a smaller time interval Δt . If $\Delta t=5$ seconds, the resolution should be 4 times better than for $\Delta t=20$ seconds. Measuring very small distances, however, would result in a large error. To avoid this we processed images that are not directly subsequent. This is shown in Table 2 in a case, where the images are taken 5 seconds apart, but all calculations are performed between images taken 20 seconds apart.

Table 2. Choosing appropriate images for a calculation with higher resolution

Captured images	a	b	c	d	e	f	...
Subtraction of images	A=e-a	B=f-b	C=g-c	D=h-d	E=i-e
Velocity calculation	E-A	F-B	G-C	H-D

For example, the subtracted image A is now calculated from images e and a and the velocity is calculated from the subtracted images E and A . This method leads to a much better resolution, because of the much higher number of data points and the avoiding of measuring very small distances. Furthermore, it gives a possibility of controlling the width of the subtracted fronts, which should be below a chosen distance (presently 20 pixels).

7. Simulation of Chemical Waves

Waves in simple excitable media (using the Oregonator model) can be characterized by solving the following two-variable reaction-diffusion equation system:

$$\frac{\partial u}{\partial t} = D_u \nabla^2 u + f(u, v) \quad \frac{\partial v}{\partial t} = D_v \nabla^2 v + g(u, v) \quad \text{Eq. 41}$$

where u and v are called excitation and recovery variables (in the Belousov-Zhabotinsky reaction the excitation variable is bromous acid and the recovery variable is ferroin), D_u and D_v are the corresponding diffusion coefficients, ∇^2 is the Laplacian operator and f, g are the reaction terms. Excitability properties can be explained by the local uncoupled dynamics given by the following ordinary differential equation system:

$$\frac{du}{dt} = f(u, v) \quad \frac{dv}{dt} = g(u, v) \quad \text{Eq. 42}$$

A typical phase-plane with the nullclines $f(u, v) = 0$, $g(u, v) = 0$ and the trajectories are shown in Figure 61. The steady state at the intersection of the nullclines is globally, asymptotically stable. This rest state is excitable. This means that after a small perturbation the system returns directly and quickly to the steady state, but larger perturbations (above a threshold) trigger a long excursion before returning to the rest state. In the section (a) the excitation variable u increases rapidly causing (b) a slower and temporary increase in v , followed by (c) rapid extinction of u and (d) slow decrease of v back to the rest state. The pathway (e) is starting from the already “excitable refractory” state showing an excitation before achieving the rest state.

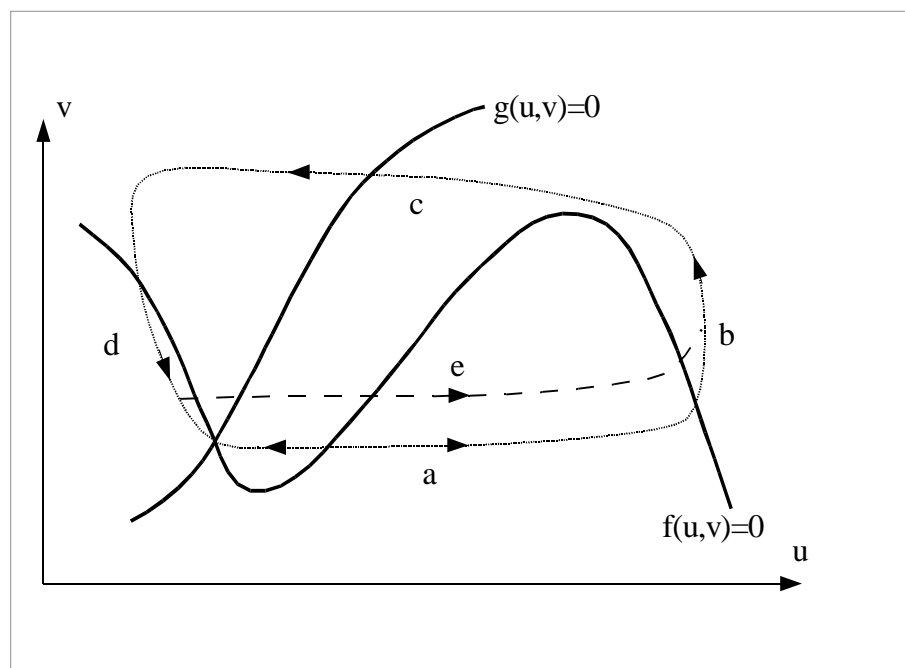


Figure 61. A typical phase plane diagram for a differential-equation model of an excitable medium.

7.1. *Why cellular automaton model?*

Cellular automaton models of excitable media are rough approximations of the behavior of excitability. Their advantage is the relative little computational effort compared to a numerical solution of the original partial differential equation (PDE) system. In earlier cellular automaton models [72,73] it was usually assumed, that the state of the system can be described by a single variable, that takes integer values: 0,1,2,3..N. Later two-variable models were developed [74-79] and complicated calculation rules were used to fit the model to the behavior of the excitable medium. These models described the excitable system quite well, they were able to reproduce even such phenomena like dispersion (the speed of an excitation front depends on how fully recovered the medium is) and curvature effect (the speed of wave propagation depends on the curvature of the front), but their disadvantage was the difficulty of fitting to a real chemical, excitable system [77].

The excitable medium is represented as a grid of cells in cellular automaton. A cell is treated as a small reactor where homogeneous chemical reactions are running. The “connections” between neighbor cells are established by diffusion. Operator splitting is used: the reaction and diffusion terms are calculated in alternation.

Our newly developed model is based on a similar pathway shown in Figure 61, we calculate the reaction terms directly from the phase plane without using any chemical kinetics and differential equations. This model is simpler than earlier cellular automaton models, essentially faster and more flexible than solving PDE-s. Thus it might be better suitable for modeling a variety of excitable media. In recent simulations (for testing the model) a simplified phase plane was used which is shown in Appendix C (page 81).

7.2. *Calculating the reaction term*

For the reaction we assume a so-called slow manifold with discrete points as states of a two variable system, similar to Figure 61. Each state is defined by its location on the phase-plane and by a pointer to the next state (Figure 62a). The stable focus points to itself, all other states point to a different state that represents the state of the system after the next reaction step. This arrangement defines the chemical pathway that occurs in an isolated cell if it was somehow excited. At the beginning of the calculation all the grid cells are attributed to one of the system states, usually to the stable focus. A reaction step means that the cell springs from one state to the next along the slow manifold, until it reaches the stable focus.

7.3. *Calculating the diffusion term*

We calculated the diffusion in a similar way as Barkley [78,79]. The Laplacian was evaluated by finite differences on a regular square grid using the nine-point formula to reduce grid

anisotropy (in a square grid the diagonal neighbors are farther from the center than the cross neighbors):

$$u'_{i,j} = D_{u,i,j} \left(\frac{\sum_{r,s} A_{r,s} u_{i+r,j+s}}{20} - u_{i,j} \right) + u_{i,j} \quad \text{Eq. 43}$$

and similarly $v'_{i,j}$ was obtained, where $u_{i,j}$ is the value of u at grid cell (i,j) , $D_{u,i,j}$ is the diffusion coefficient for component u in the cell (i,j) , and $A_{r,s}$ is the weighing factor: $A_{r,s}=4$ for the four nearest (cross) neighbors, $A_{r,s}=1$ for the diagonal next-nearest neighbors, otherwise $A_{r,s}=0$. So, the denominator in Eq. 43 is the sum of the weighing factors: $4 \times 4 + 4 \times 1 = 20$.

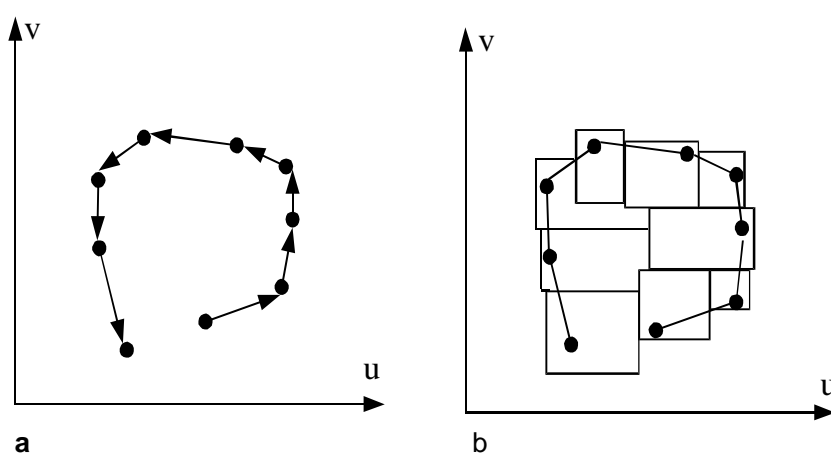


Figure 62. The simplified phase-plane used in the simulation. Slow manifold (a) and fast manifold (b).

Though the grid anisotropy can be reduced by this nine-point method, the shape of the cells of the periodic lattice still propagates to macroscopic scales and square shaped waves appear instead of circles. To reduce this effect further, more diffusion steps are calculated subsequently before a new reaction step is calculated.

It was observed in chemical experiments [80,81], that changing the diffusion coefficients in regions of the medium, changes the geometry of chemical waves. That's why a second diffusion factor was applied for each cell in the grid to define spatial inhomogeneity in the medium. The resulting diffusion coefficient $D_{u,i,j}$ was calculated by a simple multiplication: $D_{u,i,j} = D_u * D_{i,j}$ where D_u is the component dependent part and $D_{i,j}$ is the spatially dependent part. $D_{i,j}$ can be in the range of (0.1-2), the default is $D_{i,j}=1$ in all cells (no inhomogeneity).

Of course the calculated new coordinates (u', v') do not fit to the discrete states of the phase-plane. To convert them, a so-called fast manifold (similar to a lookup table) was defined, that attributes all the inner points of the phase-plane to one of the possible states (points of the slow manifold) of the system (Figure 62b). (If there was no attribution given in the fast manifold to a phase-plane point, the algorithm maps automatically the point to the nearest state defined in the slow manifold. It is especially useful if 'waterwalls' are used (see later), because the x, z concentrations of 'water' is zero (phase-plane coordinates are (0,0)) that is normally outside of

the defined slow manifold.) Both the fast and slow manifold are defined in an input file and can be easily changed and fitted to different chemical systems.

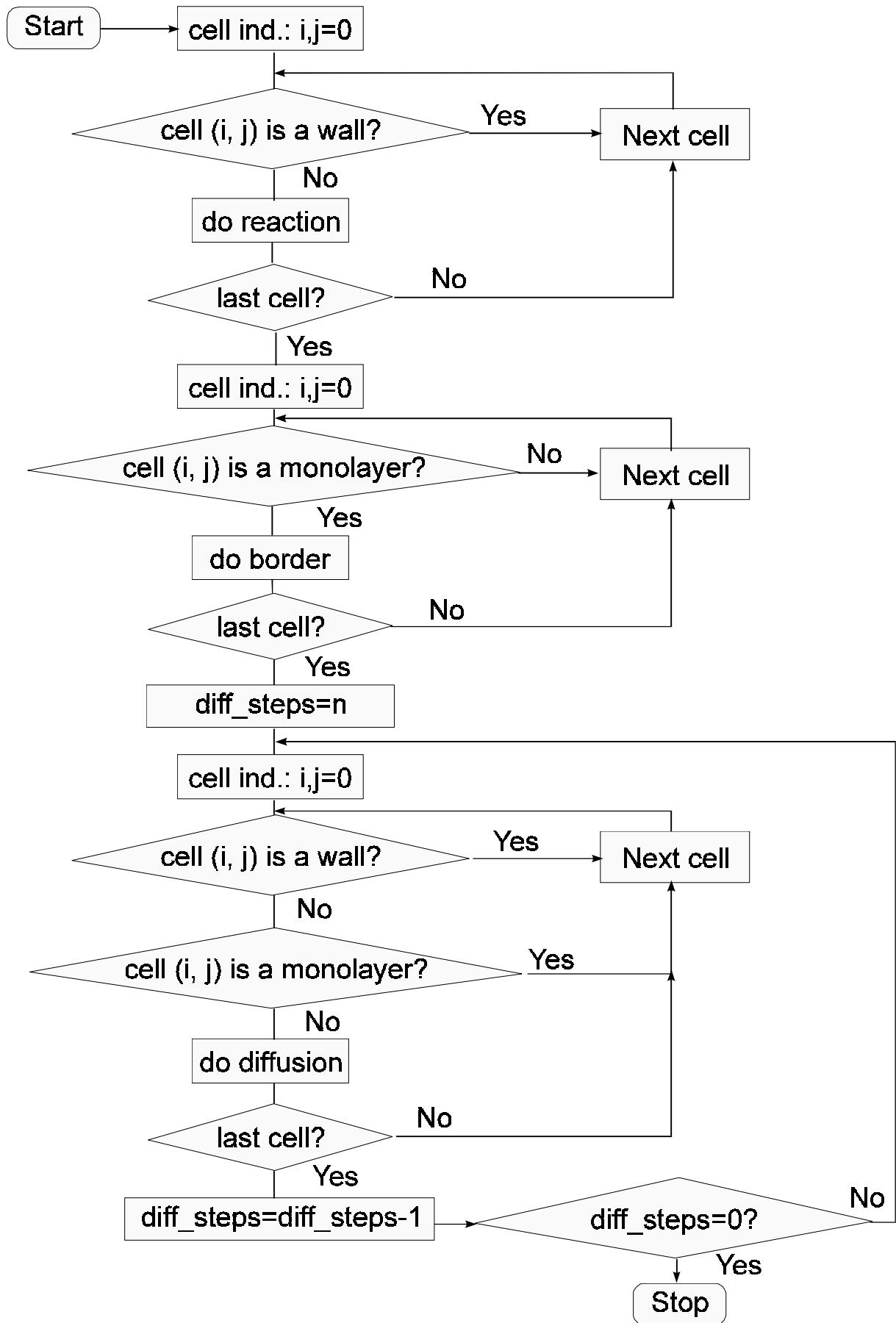


Figure 63. Block diagram of the core of the simulation

7.4. Borders and walls

A grid cell can be also marked as wall. There is no reaction and no diffusion in walls, of course. To handle wall effects a monolayer is defined along the walls and borders. The monolayer is a set of grid cells, lying directly next to the walls. There is reaction in the monolayer, but no diffusion is assumed (because the nine-point formula (Eq. 43) cannot be evaluated, its points lie also in walls).

Two different types of walls (borders) are used (Figure 64): 'Waterwall' fills the monolayer with water, a compound with the phase-plane coordinates of (0,0). 'Glass wall' mirrors the second cell layer along the walls to the first monolayer.

A simple block diagram of the simulation can be seen on Figure 63. It represents only the core of the calculation and shows the logical connection between different modules. The program was developed in C++ on a Silicon Graphics Indy Workstation with a 200 MHz Mips R4400 processor. The reference pages of the program are shown in Appendix B (page 79).

7.5. Results

The ability of this simulation program is shown in the following examples. The same phase-plane model, as presented in Appendix C, was applied. The differences in the different examples are the values of the diffusion parameters: D_u , D_v , n_D (diffusion coefficients of the components u and v , and the number of diffusion steps calculated for one reaction step respectively), and the combination of different geometries of walls.

A target pattern is initialized by using a pacemaker that triggers a new wave with a given frequency. However, in the simulation a small region was set to the excited state manually. After some simulation steps (when the medium returned to the rest state in the place of the initialization) a new wave was started manually again exactly in the same location. On Figure 65a this method was repeated three times.

To form a spiral (Figure 65b) a wave front was broken up and one half of the wave was deleted. After some simulation steps a spiral, which rotates with constant angular velocity around a core, develops. The process of the spiral development can be seen in Figure 66.

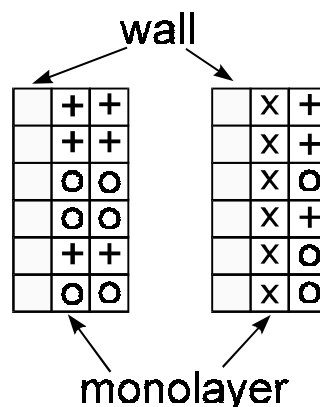


Figure 64. Glass wall and Water wall. Gray squares are walls, + and o are two different chemical states and x is water.

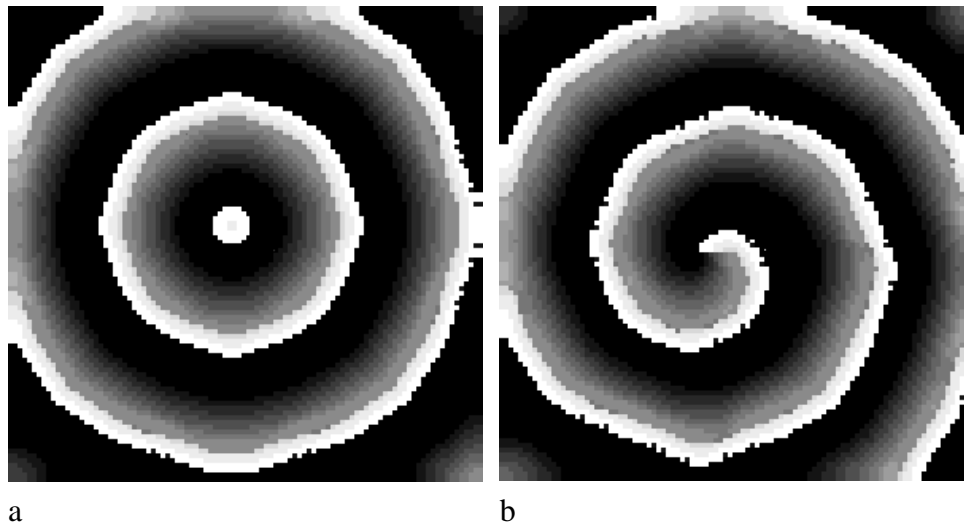


Figure 65. Target pattern (a) and spiral (b) wave.

Grid size: 100×100 ; $D_u = D_v = 0.6$; $n_D = 7$

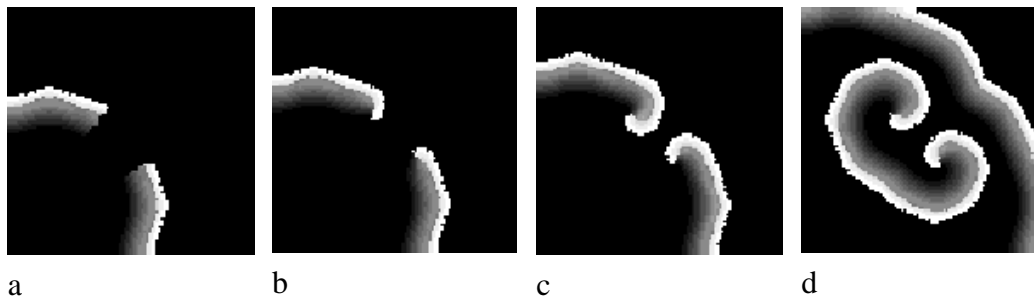


Figure 66. Snapshots of spiral development on broken wave ends

The continuous wave front was broken up on the (a) image. The free wave ends form a double spiral that works as a wave source and sends waves without any further outer influence (b-d).

Grid size: 100×100 ; $D_u = D_v = 0.6$; $n_D = 7$

The model shows also the dispersion effect. Since this is a discrete algorithm with relative few points of states the waves are propagating always in a fully regenerated medium. That means that even after infinite time there is no dispersion effect, the distances between the waves do not equalize. Thus a trick is necessary to observe this effect. Either a new phase-plane with much more points should be defined or the range of diffusion should be increased. The latter can be seen in Figure 67, where a three armed pinwheel was created by placing a circular obstacle (wall) in the center. The arms of the pinwheel were arranged asymmetrically at the beginning. The range of diffusion was then slowly increased by increasing n_D . The arms became wider and the tail of the wave front slowed down the next front until the distances between the waves were equalized.

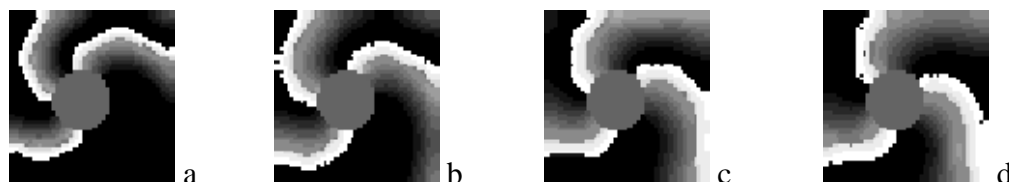


Figure 67. The dispersion effect equalizes the distances between the waves

The circle shaped gray obstacle in the middle was created as wall and the pinwheel is rotating around it.

Grid size:50x50; $D_u=D_v=0.8$; (a) $n_D=3$; (b) $n_D=5$; (c) $n_D=7$; (d) $n_D=9$

The simulation program provides the possibility to create regions with different (normally lower, but also higher) diffusion properties. In the region marked by an ellipse in Figure 68 the diffusion coefficients D_u and D_v were multiplied by a local diffusion coefficient making the overall diffusion slower. This slower diffusion region acts as a chemical lens, where the local velocity of waves is lower. So the planar waves propagating from the bottom are refracted by this lens. Later, because of the curvature effect, they become planar again and run out of the simulation field (top). In real chemical wave experiments a thin foil was applied under the membrane that enabled only lateral diffusion and made the speed of wave propagation lower. This foil corresponds to the region marked with the ellipse here.

Turing patterns (stationary patterns, that don't change in time) can appear in an excitable medium if the diffusion coefficients of the two components are very different. Figure 69 was created from a wave front by changing D_u significantly smaller than D_v . After some minutes of simulation time there was no change in shape any more. Perturbing this stable pattern forms a new stationary pattern again, soon after restarting the simulation.

The program is also suitable for solving labyrinth problems (Figure 70). Showalter et al. applied a similar experimental membrane technique to find minimum-length paths in complex labyrinths [82].

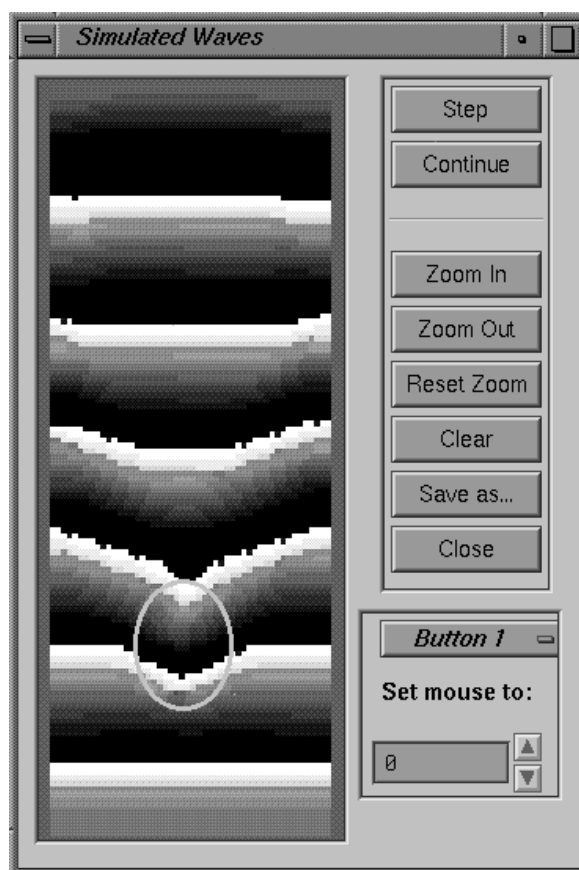


Figure 68. Chemical lens and curvature effect in the user interface of the simulation program.

Grid size: 50x150; $D_u=D_v=0.7$; $n_D=7$. In the region marked with the ellipse the diffusion coefficients D_u and D_v are multiplied by the local diffusion coefficient of 0.6. Waves are running from the bottom to the top.

Applying the curvature effect diodes can be created. These are gates allowing the waves to pass through only from one direction. These gates are narrow channels but their width is not uniform: on one end it is somewhat narrower than on the other one (Figure 71a). The wave can enter in both ends, but exit only on the wider one, because there is only a very small amount of autocatalyst and the wave curvature on the narrow side is as large that the autocatalyst distributes into the nearest environment before it can achieve the threshold limit of excitation (Figure 71b,c) and the wave dies on exit. It was also experimentally proved [50], that the wave cannot exit from a narrow capillary tube if its width is under a critical value. Even logic (AND, OR) gates were built using the Belousov-Zhabotinsky reaction [83,84].

It is possible to build complex “machines” from diodes. As an example, we consider a two-diode machine on Figure 72. The place of input is in the right bottom corner and its output is in the left upper corner. By starting a wave in the input it passes the diode ($D1$) pointed by the longer arrow. It bifurcates then to the output and also into the direction of the second diode ($D2$). The triangle shaped obstacle will be surrounded by the wave, but

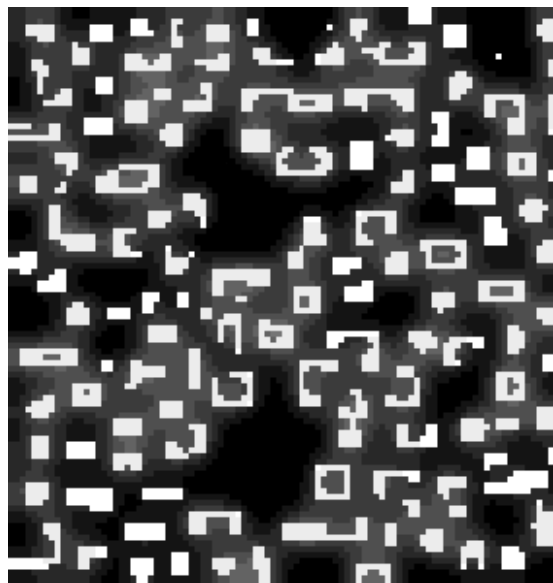


Figure 69. A stationary (Turing) pattern

Grid size: 100x100; $D_u=0.1$; $D_v=0.9$; $n_D=9$

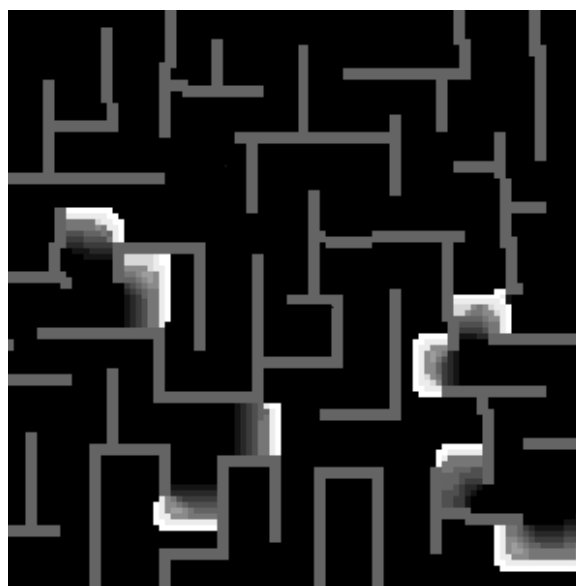


Figure 70. A labyrinth with waves

Grid size: 100x100; $D_u=D_v=0.6$; $n_D=3$



Figure 71. Diode and its open and closed states

(a) The diode itself. (b) Diode in the open direction. The wave source is a spiral on the right that sends waves through the channel of the diode. (c) Diode in closed direction. The spiral is now on the left, but the waves are unable to exit from the channel into the right side.

Grid size: 50x50; $D_u=D_v=0.6$; $n_D=3$

because of its diode property on the bottom the wave can pass it only from the counterclockwise direction, the clockwise arm will die. The diode puts an asymmetry into the system that's why a pinwheel can be formed around this obstacle without any further outer intervention. The pinwheel then acts as the wave source, rotates around the triangle and sends waves with a constant frequency only to the output, because the input is protected by diode ($D1$). Changing the diodes to normal channels changes the behavior of this machine to a simple labyrinth without any extra functionality.

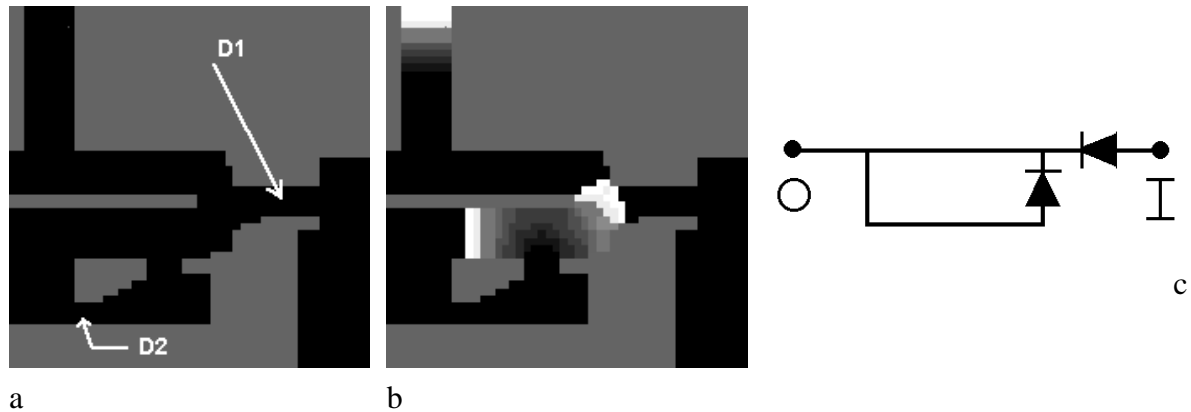


Figure 72. A simple two-diode machine

(a) Construction of the machine. The white arrows show the position of the diodes. Gray regions are walls. D1 and D2 denotes the channels of the diodes (b) Machine in work. The spontaneously developed pinwheel sends waves to the output (upper left corner) after a wave was started in the input (bottom right corner). (c) Logical connection of diodes. I:input; O:output
Grid size:50x50; $D_{11}=D_{1v}=0.6$; $n_D=3$

Summary

Pattern formation due to coupling of reaction-diffusion processes in the Belousov-Zhabotinsky (BZ) reaction is in the focus of scientific interest since its discovery about 25 years ago. For a long time, experiments were carried out in thin layers of BZ solutions. In these closed systems, the reagents were gradually consumed, therefore the applied solutions were ageing rather rapidly, and it was not possible to maintain constant conditions for a longer time. Also, the commonly used ferroin catalyst has a tendency to decompose at usual BZ conditions. Furthermore, in solutions the disturbing effect of convection and hydrodynamic motion cannot be separated from reaction-diffusion phenomena. Finally, in most BZ solutions bubble formation due to gas evolution also interferes with pattern formation.

The first aim of this work was to develop a new, simple technique to eliminate the disadvantages of the "classical" methods and to make the investigation of chemical waves easier, more flexible and more reproducible.

A second aim of this work was to achieve a better understanding of the propagation properties of chemical waves. While pattern formation seems to be a common phenomenon also in biology (for example, appearance of circular and spiral waves in the heart muscle), investigations with chemical waves can be helpful for the understanding of their more complex biological counterparts.

First the new experimental technique was developed. The ferroin catalyst was fixed on the surface of different, commercially available microfilter membranes. It turned out that the best combination was using polysulfon membranes with bathoferroin catalyst, a compound derived from ferroin. This modified membrane was contacted with the BZ solution and the propagation of waves was investigated. Two reactors were developed for these experiments, a simple one for preexperiments and demonstrations and a second one for measurements with high accuracy and with better control.

Next the shape of chemical waves propagating in homogeneous annular excitable media was investigated. We found that the general shape of the waves is an involute of the obstacle the waves are rotating around. In this case we found a good agreement between theory and measurements.

Another interesting point of this work is the investigation of chemical waves propagating in inhomogeneous media (these investigations are rather difficult using classical experimental methods). The diffusion properties of the excitable media were changed by applying barrier foils between the membrane with the fixed catalyst and the bulk of the BZ solution. The foil prevented the transversal diffusion of inhibitory intermediates, and the speed of propagation was slowed down. On the boundary between a fast and a slow region refraction effects could be detected, similarly to those in classical linear optics. Lens experiments showed that Snell's law is valid also in the case of chemical waves. These experiments can help students to understand refraction effects in general, thus we offer these experiments for schools as demonstrations in

physics lessons. The shape of chemical waves rotating in a nonuniform annular medium was also explained. This explanation and shape-forecast can be of biological-medical interest, because a similar phenomenon in the heart muscle is known, called heart-flutter.

The experiments were recorded by a computer-video system. A self-developed image processing program for the evaluation of the chemical wave experiments is presented. It calculates the velocity of the wave fronts and displays a velocity profile. There are two parallel algorithms calculating the velocity; one is based on the displacement of the fronts, the other one calculates a relative velocity (refraction index) directly from the shape of the wave fronts.

A second computer program was developed for the simulation of chemical waves. It is based on a cellular automaton model, but it is able to reproduce all of the phenomena investigated experimentally. It can even simulate Turing-structures or diode effects. However, until now, these effects have not been observed in the BZ reaction.

Zusammenfassung

Seit ihrer Entdeckung vor 25 Jahren ist die Musterbildung über die Kopplung von Reaktions-Diffusions-Prozessen in der Belousov-Zhabotinsky (BZ) Reaktion von großem wissenschaftlichem Interesse. Für eine längere Zeit wurden die Experimente in dünner Schicht der BZ Lösung durchgeführt. In diesen geschlossenen Systemen wurden die Reagenzien kontinuierlich verbraucht, und es war nicht möglich, die Konzentrationen über längere Zeit konstant zu halten. Der meist verwendete Katalysator Ferroin hatte auch die Tendenz, sich unter den chemischen Bedingungen im BZ System langsam abzubauen. Außerdem lassen sich die störenden Effekte der Konvektion und der hydrodynamischen Bewegung nicht von dem Reaktions-Diffusions Phänomen trennen. Schließlich entstehen in den meisten BZ Lösungen Gasbläschen, die bei der Musterbildung stören.

Das erste Ziel der vorliegenden Arbeit war die Entwicklung einer neuen, einfachen Technik, die die Nachteile der alten, klassischen Methoden eliminiert und die Untersuchung chemischer Wellen einfacher, flexibler und besser reproduzierbar macht.

Das zweite Ziel der Arbeit war ein besseres Verständnis der Ausbreitung chemischer Wellen. Da die Musterbildung ein allgemeines Phänomen auch in der Biologie ist (wie zum Beispiel das Auftreten von Kreis- und von Spiralwellen in den Herzmuskeln), können die ausgeführten Untersuchungen zum Verstehen der viel komplexeren biologischen Prozesse beitragen.

Zunächst wurde die neue Technik entwickelt. Der Ferroin-Katalysator wurde auf der Oberfläche verschiedener, kommerzieller Mikrofilter-Membranen fixiert. Als beste Kombination haben wir eine Polysulfon-Membran mit dem Bathoferroin-Katalysator (ein Ferroin-Derivat) gefunden. Die Membran, die mit dem Katalysator modifiziert wurde, wurde in Kontakt mit der BZ Lösung gebracht, und die Ausbreitung der chemischen Wellen wurde untersucht. Für die Experimente haben wir zwei Reaktoren entwickelt, einen einfacheren für Vorversuche und Demonstrationen und einen zweiten für Messungen mit höherer Genauigkeit und mit besseren Kontrollmöglichkeiten.

Als erstes haben wir die Geometrie chemischer Wellen untersucht, die sich in einem homogenen ringförmigen Medium fortbewegen. Wir haben gefunden, daß die Geometrie der Wellen sehr gut als Evolvente des Innenringes (normalerweise ist es ein Loch, um welches die Wellen herumlaufen) beschrieben werden kann.

In einem weiteren Teil der Arbeit werden chemische Wellen in einem inhomogenen Medium betrachtet; solche Untersuchungen sind mit den alten, klassischen Methoden nur sehr schwierig durchzuführen. Die Diffusionseigenschaften des erregbaren Mediums wurden durch die Anwendung von Folienstücken zwischen der Membran mit dem Katalysator und der BZ Lösung geändert. Das Folienstück behindert den Diffusionstransport der BZ Komponente. Dadurch verbleiben inhibierende Zwischenprodukte in dem Folienbereich, und die Wellengeschwindigkeit wird dadurch verlangsamt. An der Grenze eines langsamen und schnellen Bereichs kann man

ähnliche Brechungseffekte beobachten wie in der klassischen Optik. Linsenexperimente zeigen, daß das Gesetz von Snellius auch im Fall von chemischen Wellen gültig bleibt. Diese Experimente können Schülern bei dem allgemeinen Verstehen der Brechung helfen, so daß diese Versuche als Demonstration im Physikunterricht geeignet sind. Auch die Geometrie der chemischen Wellen, die sich in einem ringförmigen nicht-homogenen Medium ausbreiten, konnte in einem solchen Modell erklärt werden. Diese Erklärung kann für Biologen und Mediziner nützlich sein, da ein ähnliches Phänomen in dem Herzmuskel bekannt ist ("Herzflattern").

Die Experimente wurden mit einem Computer-Video-System durchgeführt. Ein selbstentwickeltes Bildauswertungsprogramm für die Wellenexperimente wird beschrieben. Das Programm berechnet die Wellengeschwindigkeiten und ein Geschwindigkeitsprofil. Zwei verschiedene Algorithmen wurden verwendet, um die Geschwindigkeit zu berechnen; einer davon basiert auf der Bewegung, der zweite auf der Geometrie der Wellenfronten. Im zweiten Fall wird aus der Frontgeometrie der Brechungsindex erhalten.

Ein weiteres Programm wurde für die Simulation von chemischen Wellen entwickelt. Es basiert auf einem Zellenautomaten-Modell, kann aber alle experimentell beobachteten Phänomene reproduzieren. Es ist sogar möglich, Turing-Strukturen oder das Verhalten von Dioden zu simulieren. Diese Phänomene konnten allerdings bisher in der BZ Reaktion noch nicht beobachtet werden.

Appendix

Appendix A. Program Reference Pages of WANA

NAME

Wana - a chemical Wave ANALysis program that produces velocity maps

SYNOPSIS

wana [catalog filename]

DESCRIPTION

This program calculates velocity maps of chemical waves in the Belousov- Zhabotinsky reaction by using a series of images taken by a video camera. The subsequent images are subtracted, LUT and BLUR operators are performed to increase picture quality. Then the program looks for waves, calculates their velocities and creates a velocity map. The user can interactively calculate some simple "statistics".

THE CATALOG FILE

The image files and their catalog file should be in the same directory. The catalog file (ASCII, with the extension ".tim") lists the image filenames and the time of capturing in clockticks (1 sec=100 clockticks on an INDY, but this is computer dependent) and also in seconds. Lines with trailing # treated as remarks. The file format is: <imagename> <clockticks> <seconds> separated with one or more spaces.

Example:

```
first-0.jpg 16226904 162269
first-1.jpg 16229148 162291
```

You shouldn't leave any blanks before the filenames. The image name should be in the form of <name-#.jpg> where # is the serial number of the image. Any widely used image formats (rgb, tif, jpg, gif, fit) are supported as long as they are grayscale, but the program was only tested with JPEG-s. (You can use the utilities gray , capture.script , and timer to fulfill these requirements. They will create the files in the desired format and they are included in the installation.)

THE USER INTERFACE

The Main Window: Input Controls

This window will be shown at startup. To load a catalog you can either drop a catalog file in the drop pocket, or write its name in the finder or load it via the Open Catalog in the File menu. The values (in 1/100 sec or clockticks) in the time difference fields control the subtraction algorithm and the velocity calculation. Suppose that the images A B C D E F G H ... were taken subsequently with the interval dt. If the time of subtraction is t then the following subtraction will be performed:

t<dt	B-A C-B D-C
dt<t<2*dt	C-A D-B E-C
2*dt<t<3*dt	D-A E-B F-C ... and so on...

You should choose a t value that gives a continuous, thin wave front (1-3 mm on the screen). Wider wave fronts can't be located perfectly. The time of evaluation controls the velocity calculation on the same way: Now suppose that the above letters are the subtracted images and B-A means, that the velocity is calculated out of the distance between the wave fronts on the subtracted image B and subtracted image A.

Check the Show subtracted images in the View menu to see each subtracted image during the searching of the waves. If it is unchecked the program shows an image as a background picture, and draws the waves on it. Input lookup table in the View menu pops up a dialog with LUT and BLUR controls. The image contrast can be modified here. If the wave searching algorithm finds too many bad waves (waves that couldn't be identified perfectly, shown with darker colors), simply change the values of the LUT to give the image more contrast. Check the Extrapolation to the hole edge in the Options menu if you want to see the waves drawn to the edge exactly. This method is not very accurate, so use it carefully. The velocity map calculated with this option ON can be unrealistic close to the edge.

The Viewer

This window is also posted at startup. It is the empty black window to the right of the main window. You will find all the images (graphic output) in this window and it is also used for doing graphical selection.

The Membrane Settings Window

This window is only a small control panel for the graphical input. The type of the hole in the membrane can be selected. To mark a circle region choose Circle and click on three different points of the hole edge with the middle mouse button. To mark a polygon region choose Polygon and click on the vertexes of the desired polygon. After the last point is drawn, close the polygon with the Close Polygon button. Mark the membrane outer edge with the left mouse button, again clicking on three different points. With the right mouse button you can mark the starting wave, and clicking again defines the propagation direction (a nice red arrow will be shown). Note, that the Clear Settings button clears all the 3 settings (outer edge, hole, direction) and you should mark them again. However, you can simply overwrite the arrow with a new one, but the other settings can be only corrected with the Clear Settings button. Redraw Screen clears all the unused “paintings”, only the valid ones remain. You can use this button also to make the still valid, previous settings visible. TIP: You can see the small arrow, if you hold down the right button and drag the mouse. Don’t forget to click again to fix it! Involutes draws a theoretical involute. The membrane sizes should be set previously. See “The Theoretical Involute Drawing dialog” section on details.

The Map Controls

If the velocity calculation is ready the Map Controls window pops up. Simply press the Calculate Map button to see the map. V_{min} and V_{max} controls the interpolation colors and velocity. You can override the default algorithm (which makes automatically the best resolution) by typing new values and turn on the Use these values button. It is especially useful, if you want to compare a series of velocity maps, that were drawn with the same color table. Show Wave fronts draws all or only some of the wave fronts into the map, turn it on-off to change to another mode of drawing. Kernel Size defines an interpolation range for the map calculation. The bigger it is the smoother the map, but the slower the calculation.

When the map is ready you can select a portion of the map. The selection follows as it was described above in the “Membrane Settings Window” with the middle mouse button. After selection you can Calculate Statistics to get average velocity values inside and outside the selected area. You can repeat the selection and statistics calculation as many times as you want. The left mouse button is for marking a line with its end points. Interpolated velocities will be calculated at ten points (or less) along this line by using the Kernel Size value and will be displayed immediately in Statistics.

The right mouse button starts a refraction index map calculation based only on wave geometry. It can be activated if the usual velocity map has been already shown. Its calculation lasts approximately as many times as the other one, but after that you can change between them very fast using the right mouse button. The two calculating methods are independent, but they are using the same set of wave data. Note, that this second algorithm works only in special cases: Circular hole in the center and circular symmetric inhomogeneity in the membrane. You can try it in other cases also, but it won’t give realistic results. Marking a line with the left mouse button works also with the refraction index map, but marking a region and calculating statistics works always with the usual velocity map, even if the other one is shown!

Save Map as... button saves the map (velocity or refraction index, currently shown) as a TIFF file. All the extra drawings are neglected, only the pure map (or the map with the wave fronts) will be saved! If you need the other drawings, use the SGI snapshot utility in the Desktop Tools folder and save the content of the window. The Involute button posts a dialog for involute drawing.

The Theoretical Involute Drawing dialog

The calculation runs between the radii of r_1 and r_2 . The radius of the base circle of the involute is r_0 and the starting angle is ϕ_0 . Change these values if they don’t fit. The default values were calculated from the membrane size, the hole size, and the position of the starting wave. You can modify the center of the base circle of the involute and move the curve in x and y directions with the thumbwheels dx and dy . The Angle fine tune defines an increment for the base ϕ_0 value. It doesn’t alter the base ϕ_0 ! There are restoring buttons on all thumbwheels to restore the original position. The direction button inverts the involute. If you change the values in the textfields, don’t forget to press the Apply button to make the changes visible. Neither the apply button, nor the other controls refresh the graphical window. If it is dirty enough, press the Redraw button in the Map Controls window and repaint the curve with the Apply button. It is possible to open more dialogs. This is the way how you can draw more complex curves.

The LUT dialog

This dialog is posted if you invoke the Input Lookup Table submenu in the View menu. It contains four slider to control the contrast settings. The LUT is a lookup table. It defines the output of an input color (graylevel). LUT Low cuts all the values to zero below its own value, LUT High cuts to zero above its own value. The values between “LUT Low” and “LUT High” are interpolated between 0-255. Blur is the smoothing

algorithm. More “blur” makes smoother. Blur Kernel Size is the environment of blurring. The bigger it is, the smoother is the result.

BUGS

Closing the “Involute Drawing dialog” with the window manager’s “Close” menu can cause a program crash. Always use the OK buttons in the dialogs to close them!

FILES

/usr/sbin/wana
/usr/lib/X11/app-defaults/Wana
/usr/lib/images/wana.icon
/usr/lib/filetype/local/wana.ftr
/usr/lib/filetype/local/iconlib/wana.closed.fti
/usr/lib/filetype/local/iconlib/wana.open.fti
/usr/share/catman/u_man/cat1/wana.z

SEE ALSO

capture.script(1), timer(1), gray(1)

COPYRIGHT

1996. Attila Lazar. The program is free. Any change of the code is permitted.

AUTHOR

Attila Lazar, Department of Physical Chemistry, Philipps University, Marburg, Germany.

Appendix B. Program Reference Pages of WASI

NAME

Wasi - a chemical WAve SIMulation program

SYNOPSIS

wasi [input filename]

DESCRIPTION

The algorithm is based on a refined cellular automaton model. The waves are calculated in a cell matrix with the operator splitting method: One step reaction will be calculated for the whole matrix and one or more steps diffusion follow.

Calculating the reaction

The reaction is calculated with the help of a simplified phase map. This phase map consists of discrete points and vectors connecting the points. One point is represented by 4 values: a serial number, a direction (in which state will be the cell after the next reaction step) and the location in the phase map (concentrations of the two key components). E.g.: "0 1 2 2" is the description of the point 0, it connects to the point 1 and its location is (2,2) on the phase map. It means the cell has only discrete states on the phase map and a "reaction step" is always a jump from one point to another point. It is called the slow manifold.

Calculating diffusion

A diffusion step takes only the nearest neighbors into consideration. A cell (P) has always eight nearest neighbors, four are attached to the side of the cell (Ai), and four are attached to the corner in diagonal directions (Bi). The new concentration in the cell P after a diffusion step is:

$$[P']=[P]+D*\{((4\text{Sum}[A_i]+\text{Sum}[B_i])/20)-[P]\}$$

for both components. D denotes the relative diffusion coefficient for the component in the range [0..1] and Sum is the summation operator. The concentration in the cell changes with the weighed average concentration of the neighbor cells. If more diffusion steps are necessary P' can be recalculated. The recalculation can only occur if the first calculation has been finished for the whole matrix of cells. Of course, P' will not fit to the discrete points of the phase map, so it will be converted to one of the phase points using a "lookup table", the so called fast manifold. It is defined as a set of rectangular regions in the phase space mapping to a phase point. Each region is represented by 5 values each: the serial number of the phase map point, and the lower-left, upper-right coordinates of the rectangle. E.g.: "2 0 0 3 2" The points in the rectangular region, defined by (0,0) (3,2) are attributed to the phase point 2.

THE FORMAT OF THE INPUT FILE

The settings for the slow and fast manifold should be given in the input file. It is an easy editable ASCII file. Empty lines and lines starting with # are neglected. The lines between the commands .SLOW and .END are considered as the definition for the slow manifold, and those between .FAST and .END are considered as the fast manifold definition (the commands can be abbreviated as .S .E .F). The commands should start at the beginning of a line and each definition point should be written in separate lines. An example is shown in Appendix C.

USING THE PROGRAM

The main window

The main window controls all the necessary starting conditions. The diffusion coefficients for the two components and the number of diffusion steps for one reaction steps can be set here. The Phase map definition area is a small text editor, here you can write your own input file or change an existing one. It provides the simplest editing functions: cut, copy, paste, open, save. These can be found in the menu bar, under the File and Edit menus. The Options menu controls the settings of the simulation: Grid Size starts a small dialog to set the x and y dimension of the cell matrix. Default is a 100x100 matrix, it can be changed in the [10..500] interval in both directions. Simulation has only one setting: how to calculate the walls. You can set "glass wall" or "water wall". Colors... brings up the color settings. In the Preferences you can turn off the warning messages that appear on acceptable but not quite correct settings.

The color dialog

The program can generate a relative big number of color maps. You can either use this facility or you can edit your own map. To use the color generation algorithm choose a Color Model and a reference from the Relative to list. Press Generate and then Apply. The Relative to list contains the possible mappings. If you'd like to attribute the colors to the serial number of phase map points, choose "points". If you'd prefer to attribute to the concentration of a component, choose "comp. u" or "comp. v" or "comp. w". The component "w" doesn't exist, but this setting generates also nice color maps. The "mixed u&v" generates a colormap

that is attributed to both components: E.g. blue changes with u, yellow changes with v and you will see the mixture of them. If you want to modify the colormap yourself, choose a color from the list on the left hand side. It appears in the text field as a triple number of “red, green,blue”. You can change it there, if ready, press the modify button. You can save your self-created map with the Save Color button, or load it with the Load Color button.

The simulation window

In the middle of the window, there is the simulation field. The controls on the right are: Step to make one step simulation; Continue to make a continuous simulation; Zoom In, Zoom Out, Reset Zoom to change the size of the view (it doesn't change the matrix size, only the size of its representation on the screen); Clear clears the simulation field; SaveAs saves the simulation filed as a TIFF image; Close closes this window. The manipulation field has an option menu with six functions. The function values can be set in the Set mouse to text field either by pressing the arrows to increase/decrease the actual value or simply enter a new value and then pressing ENTER. (Entering a new value without pressing ENTER won't do any changes!) The functions are: Button1 sets the value for the left mouse button; Button3 sets the right mouse button; Point Size sets the size of a point and Monitor sets the monitor mode. Edit Walls allows you to build walls in the simulation field, and Edit Foil allows you to build inhibited regions with an inhibitor factor. The diffusion coefficient will be then multiplied with this factor in its cell. The inhibitor factor should be entered in the textfield. Its default value is 1 (no inhibition). You can set a point (cell, foil, wall) in the simulation field by pressing mouse button 1 and clear with mouse button 3. The point corresponds to the value and size previously set in the manipulation field for the buttons. In monitor mode the textfield shows the value of the point in the simulation field, that is under the cursor when pressed mouse button 2. Its form is “cell value:inhibitor value for the cell”. The program considers mouse button 3 as the value corresponding to the stable focus in the phase map. Using the Clear button sets the whole field to this value. So it is recommended to set its appropriate value at the beginning of the work (default value is 0, if it is the stable focus, you don't need to change).

BUGS

The main window doesn't show the default value for the diffusion steps at start until an expose event occurs.

FILES

```
/usr/sbin/wasi  
/usr/lib/X11/app-defaults/Wasi  
/usr/lib/images/wasi.icon  
/usr/lib/filetype/local/wasi.ftr  
/usr/lib/filetype/local/iconlib/wasi.closed.fti  
/usr/lib/filetype/local/iconlib/wasi.open.fti  
/usr/share/catman/u_man/cat1/wasi.z
```

COPYRIGHT

1996. Attila Lazar. The program is free. Any change of the code is permitted.

AUTHOR

Attila Lazar, Department of Physical Chemistry, Philipps University, Marburg, Germany.

Appendix C. Phase-plane model used in the simulations

```
#Input file of WASI
#The modified Barkley-model
#
#Definition of the slow manifold
#
```

```
.SLOW
0 1 10 0
1 2 10 5
2 3 10 10
3 4 0 10
4 5 0 9
5 6 0 8
6 7 0 7
7 8 0 6
8 9 0 5
9 10 0 4
10 11 0 3
11 12 0 2
12 13 0 1
13 13 0 0
```

```
.END
```

```
#
#
#Definition of the
#fast manifold
#
```

```
.FAST
0 1 0 10 1
0 2 1 10 2
0 3 2 10 3
1 4 3 10 4
1 5 4 10 5
1 6 5 10 6
2 7 6 10 7
2 8 7 10 10
4 0 9 8 10
5 0 8 8 9
6 0 7 8 8
7 0 6 7 7
8 0 5 6 6
9 0 4 5 5
10 0 3 4 4
11 0 2 3 3
12 0 1 2 2
13 0 0 1 1
.END
```

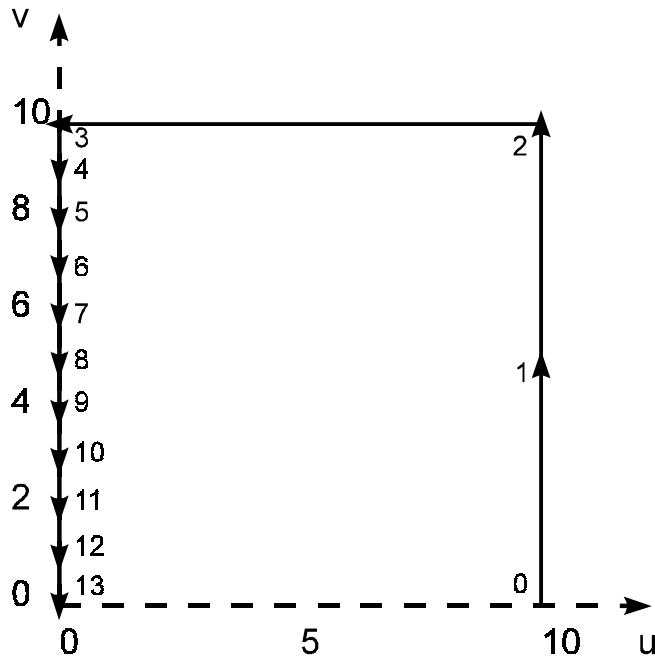


Figure 73. Graphical view of the slow manifold

Small numbers inside the diagram are serial numbers of states, large numbers outside of the diagram are coordinates of the axes (dashed lines). Solid arrows describe the reaction pathway.

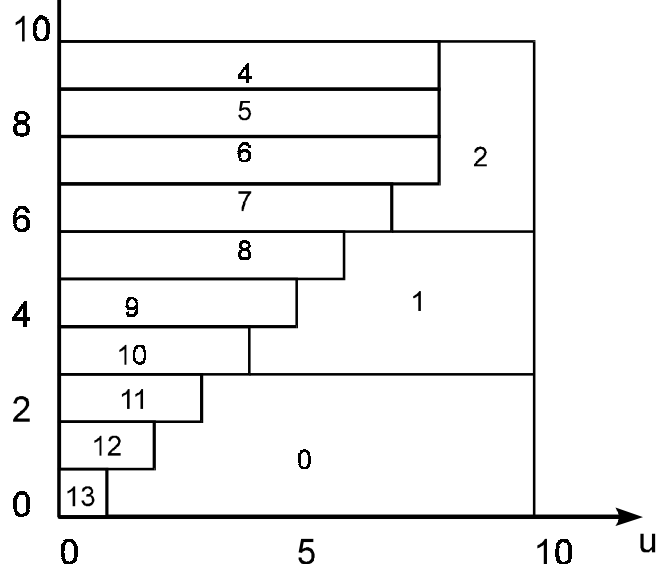


Figure 74. Graphical view of the fast manifold

Small numbers inside the diagram point to the appropriate phase-state, large numbers outside of the diagram are coordinates of the axes.

Appendix D. The C-shell script used for capturing images

```
#!/bin/csh -f
# This script captures images, saves them as JPG and creates a catalog.
# Invoke with the options:
# -n #num      Number of captured images
# -t #delta_t  Time difference between images
# -o #out      Output filename, it will be appended with a serial number
#              eg: out-0.jpg
# -s #start    Starting number. Default is 0.
# -c #camera   digital=0 (default), analog=1
# -g #gray     use grayscale conversion: OFF = 0; ON= 1  default is ON
#              E.g.      capture.script -n 5 -t 3 -o first.try

#check if an other capturing program is running
vidtomem -w >&! /dev/null
if ( $status >= 1 ) then
    echo Error! VL path is already in use! Please exit any other
    echo programs that are using the video board \(\videoin, capture,
    echo etc.\) and try again!
    exit
endif

# check write permissions in the current directory
if ( ! -w . ) then
    echo Can't write files! You do not have write permissions in this directory!
    exit
endif

# Define some defaults:
set NUMBERS=3
set TDIFF=10
set FILE=out
set START=0
set CAMERA=-v0
set GRAY=1

# Analyze parameters:
while ($#argv >0)
    switch ($1)
    case -n:
        if ( $2 > 0 ) then
            set NUMBERS=$2
        else echo The parameter \#num must be a positiv number!
            exit
        endif
        breaksw
    case -t:
        if ($2 >= 3) then
            set TDIFF=$2
            @ TDIFF -=3      #3 secs correction because of process time
        else echo The parameter \#dt must be more than 3 seconds!
            exit
        endif
        breaksw
    case -o:
        set FILE=$2
        breaksw
    case -s:
        if ( $2 > 0 ) then
            set START=$2
        else echo The parameter \#start must be a positiv number!
            exit
        endif
        breaksw
    case -c:
        if ($2 == 1) then
            set CAMERA=-v1
        endif
        breaksw
    case -g:
        if ($2 == 0) then
            set GRAY=0
        endif
    endsw
endwhile
```

```
        endif
        breaksw
    endsw
    shift argv
    shift argv
end
echo Capturing images.... Press CTRL-C to interrupt!

# Increment NUMBERS with the START starting number
@ NUMBERS+= $START

# Create header for the catalog file
timer > $FILE.tim
echo '# ' >> $FILE.tim
echo -n '# Created on ' >> $FILE.tim
date >> $FILE.tim
echo -n '# ' >>$FILE.tim

while ( $START < $NUMBERS)
    vidtomem $CAMERA >&! /dev/null          #capture image
    timer $FILE-$START.jpg >> $FILE.tim    #append catalog with current time
    if ($GRAY) then
        gray out-00000.rgb
        imgcopy gray.rgb $FILE-$START.jpg >&! /dev/null
        rm gray.rgb
    else
        imgcopy out-00000.rgb $FILE-$START.jpg >&! /dev/null #copy to jpg
    endif
    echo $FILE-$START.jpg
    @ START++                               #increment sequence
    if ($START < $NUMBERS) sleep $TDIFF    #wait if not the last image
end

rm out-00000.rgb          #delete temporary file
```

Bibliography

- [1] J.D. Murray, *Mathematical Biology* (Springer, Berlin, 1989)
- [2] A.T. Winfree, *When Time Breaks Down* (Princeton Univ. Press, Princeton, NJ, 1987)
- [3] R.J. Field, M. Burger, Eds. *Oscillations and Travelling Waves in Chemical Systems*, (Wiley, New York, 1985)
- [4] S.K. Scott, *Oscillations, Waves and Chaos in Chemical Kinetics*, (Oxford Univ. Press, Oxford, 1994)
- [5] R. Kapral and K. Showalter, Eds. *Chemical Waves and Patterns*, (Kluwer, Dordrecht, Netherlands, 1995)
- [6] A.J. Durston, *J. Theor. Biol.* **42** (1973) 483.
- [7] F. Siegert, C. Weijer, *J. Cell Sci.* **93** (1989) 325.
- [8] J. Lechleiter, S. Girard, E. Peralta, D. Clapham, *Science* **252** (1991) 23.
- [9] N.A. Gorelova, J. Bures, *J. Neurobiol.* **14** (1983) 353.
- [10] J.M. Davidenko, A.V. Pertsov, R. Salomonsz, W. Baxter, J. Jalife, *Nature* **355** (1992) 349.
- [11] Z. Noszticzius, W. Horsthemke, W.D. McCormick, H.L. Swinney, *Nature* **329** (1987) 619.
- [12] G. Kshirsagar, Z. Noszticzius, W.D. McCormick, H.L. Swinney, *Physica D* **49** (1990) 5.
- [13] W.Y. Tam, W. Horsthemke, Z. Noszticzius, H.L. Swinney, *J. Chem. Phys.* **88** (1988) 3395.
- [14] B.P. Belousov, *Sbornik Referatov po Radiatsionni Meditsine* (Medgiz, Moscow, 1958) 145.
- [15] A. M. Zhabotinsky, *Biofizika* **9** (1964) 306.
- [16] D.P. Zipes, J. Jalife, *Cardiac Electrophysiology* (W.B. Saunders Co. Philadelphia, 1990) 543.
- [17] W. Schoels, N. El-Sherif, *Cardiac Mapping*, Eds. M. Shenasa, M. Borggrefe, G. Breithardt (Futura Publishing, Mount Kisco, NY 1993) 281.
- [18] I.R. Epstein, K. Showalter, *J. Phys. Chem.* **100** (1996) 13132.
- [19] A.T. Winfree, *J. Chem. Educ.* **61** (1984) 661.
- [20] A.J. Lotka, *J. Am. Chem. Soc.* **42** (1920) 1595.
- [21] P.W. Atkins, *Physical Chemistry* (Oxford University Press, 1995) 919.
- [22] R.J. Field, R.M. Noyes, *J. Chem. Phys.* **60** (1974) 1877.
- [23] H.D. Försterling, Sz. Murányi, Z. Noszticzius, *React. Kinet. Catal. Lett.* **42** (1990) 217.
- [24] H.D. Försterling, Sz. Murányi, Z. Noszticzius, *J. Phys. Chem.* **94** (1990) 2915.
- [25] R.J. Field, E. Körös, R.M. Noyes, *J. Am. Chem. Soc.* **94** (1972) 8649.
- [26] J.J. Tyson, J.P. Keener, *Physica D* **32** (1988) 327.
- [27] A.M. Turing, *Phil. Trans. R. Soc. London* **B237** (1952) 37.
- [28] V. Castets, E. Dulos, J. Boissonade, P. De Kepper, *Phys. Rev. Lett.* **64** (1990) 2593.
- [29] A. T. Winfree, *Science* **175** (1972) 634.
- [30] R. J. Field, R. M. Noyes, *J. Am. Chem. Soc.* **96** (1974) 2001.
- [31] J. Ross, S. C. Müller, C. Vidal, *Science* **240** (1988) 460.

- [32] L. Kuhnert, *Naturwissenschaften* **70** (1983) 464.
- [33] T. Yamaguchi, L. Kuhnert, Zs. Nagy-Ungvárai, S. C. Müller, B. Hess, *J. Phys. Chem.* **95** (1991) 5831.
- [34] B. Neumann, Zs. Nagy-Ungvárai, S. C. Müller, *Chem. Phys. Lett.* **211** (1993) 36
- [35] J. A. De Simone, D. L. Beil, L. E. Scriven, *Science* **180** (1973) 946.
- [36] K.I. Agladze, V. I. Krinsky, A. V. Panfilov, H. Linde, L. Kuhnert, *Physica D* **39** (1989) 38.
- [37] A. T. Winfree, *Sci. Am.* **230** (1974).
- [38] A. T. Winfree, *The Geometry of Biological Time* (Springer, Berlin, 1980), 301.
- [39] K. Agladze, E. Dulos, P. De Kepper, *J. Phys. Chem.* **96** (1992) 2400.
- [40] K. J. Lee, W. D. McCormick, Z. Noszticzius, H. L. Swinney, *J. Chem. Phys.* **96** (1992) 4048.
- [41] Z. Noszticzius, Q. Ouyang, W. D. McCormick, H. L. Swinney, *J. Phys. Chem.* **96** (1992) 6302.
- [42] Q. Ouyang, Z. Noszticzius, H. L. Swinney, *J. Phys. Chem.* **96** (1992) 6773.
- [43] W. Jahnke, C. Henze, A. T. Winfree, *Nature* **336** (1988) 662.
- [44] W. Jahnke, W. E. Skaggs, A. T. Winfree, *J. Phys. Chem.* **96** (1989) 740.
- [45] T. Yamaguchi, S. C. Müller, *Physica D* **49** (1991) 40.
- [46] J. Masek, K. Showalter, *Nature* **339** (1989) 609.
- [47] A. M. Zhabotinsky, A. B. Rovinsky, *J. Phys. Chem.* **94** (1990) 8001.
- [48] D. Winston, M. Arora, J. Masek, V. Gáspár, K. Showalter, *Nature* **351** (1991) 132.
- [49] A. M. Zhabotinsky, S. C. Müller, B. Hess, *Physica D* **49** (1991) 47.
- [50] Á. Tóth, V. Gáspár, K. Showalter, *J. Phys. Chem.* **98** (1994) 522.
- [51] O. Steinbock, P. Kettunen, K. Showalter, *Science*, **269** (1995) 1857.
- [52] A. Sirimungkala, *Dissertation* (Cuvillier, Göttingen, 1996)
- [53] J. Oslovitch, *unpublished results*
- [54] A. Lázár, Z. Noszticzius, H.D. Försterling, Zs. Nagy-Ungvárai, *Physica D* **84** (1995) 112.
- [55] N. Wiener, A. Rosenblueth, *Arch. Inst. Cardiol. Mex.* **16** (1946) 205.
- [56] H. Lass, *Vector and Tensor Analysis*, (McGraw-Hill, New York, 1950) 64.
- [57] S.C. Müller, Th. Plessner, B. Hess, *Physica D*, **24** (1987) 87.
- [58] G.S. Skinner, H.L. Swinney, *Physica D*, **48** (1991) 1.
- [59] O. Steinbock, V. Zykov, S.C. Müller, *Nature*, **366** (1993) 322.
- [60] E. Dulos, J. Boissonade and P. De Kepper, *Physica A*, **188** (1992) 120.
- [61] J. J. Perraud, K. Agladze, E. Dulos and P. De Kepper, *Physica A*, **188** (1992) 1.
- [62] A. M. Zhabotinsky, M. D. Eager, I. R. Epstein, *Phys. Rev. Lett.* **7** (1993) 1526.
- [63] M. Markus, K. Stavridis, *Phil. Trans. R. Soc. Lond. A* **347** (1994) 601.
- [64] K. Showalter, J.J. Tyson, *J. Chem. Educ.* **64** (1987) 742.
- [65] Zs. Nagy-Ungvárai, J.J. Tyson, B. Hess, *J. Phys. Chem.* **93** (1989) 707.
- [66] E. J. Reusser, R. J. Field, *J. Am. Chem. Soc.* **101** (1979) 1063.
- [67] Z. Váradi, M.T. Beck, *J. Chem. Soc. Chem. Commun.* (1973) 30.

- [68] V.I. Arnold, *Singularities of Caustics and Wave Fronts*, (Kluwer Academic Publishers, Dordrecht, Netherlands 1990)
- [69] E. Wolf, M. Born, *Principles of optics*, (Pergamon Press, Oxford, 1959) 120.
- [70] P. Hanusse, E. Bastardie, C. Vidal, *Spatial inhomogeneity and transient behavior in chemical kinetics*, eds. P. Gray, G. Nicolis, F. Baras, P. Borckmans, S.K. Scott (Manchester University Press, 1990) 371.
- [71] S.C. Müller, Th. Plessner, B. Hess, *Science* **230** (1985) 661.
- [72] J.M. Greenberg and S.P. Hastings, *SIAM J. Appl. Math.* **34** (1978) 515.
- [73] M. Markus. *Electrochemistry and Corrosion*, eds. G. Sandstedt and G. Kreysa (VCH-Verlagsgesellschaft, 1989) 445.
- [74] M. Markus and B. Hess, *Nature* **347** (1990) 56.
- [75] M. Gerhardt, H. Schuster, J.J. Tyson, *Science* **247** (1990) 1563.
- [76] M. Gerhardt, H. Schuster, J.J. Tyson, *Physica D* **46** (1990) 392.
- [77] M. Gerhardt, H. Schuster, J.J. Tyson, *Physica D* **46** (1990) 416.
- [78] D. Barkley, M. Kness, L.S. Tuckerman, *Phys. Rev. A* **42** (1990) 2489.
- [79] D. Barkley, *Physica D* **49** (1991) 61.
- [80] A. Lázár, Z. Noszticzius, H. Farkas, H.D. Försterling, *Chaos* **5** (1995) 443.
- [81] A. Lázár, H.D. Försterling, A. Volford, Z. Noszticzius, *J. Chem. Soc. Faraday Trans.* **92** (1996) 2903.
- [82] O. Steinbock, Á. Tóth, K. Showalter, *Science* **267** (1995) 868.
- [83] Á. Tóth, K. Showalter, *J. Chem. Phys.* **103** (1995) 2058.
- [84] O. Steinbock, P. Kettunen, K. Showalter, *J. Phys. Chem.* **100** (1996) 18970.

Own Publications

Attila Lázár, Zoltán Noszticzius, Horst-Dieter Försterling, Zsuzsanna Nagy-Ungvárai,

“Chemical waves in modified membranes: I. Developing the technique”, *Physica D* **84** (1995) 112.

Attila Lázár, Zoltán Noszticzius, Henrik Farkas, Horst-Dieter Försterling, “Involutes: the geometry of chemical waves rotating in annular membranes”, *Chaos* **5** (1995) 443.

Attila Lázár, Horst-Dieter Försterling, András Volford, Zoltán Noszticzius, “Refraction of chemical waves propagating in modified membranes”, *J. Chem. Soc. Faraday Trans.* **92** (1996) 2903.

Attila Lázár, Horst-Dieter Försterling, Henrik Farkas, Péter Simon, András Volford, Zoltán Noszticzius, “Chemical Waves in Non-uniform Membrane Rings”, submitted to *Chaos*, (1997)

Attila Lázár, Horst-Dieter Försterling, Zoltán Noszticzius, “Reconstructing the inhomogeneity map”, in preparation to *Computers Chem.*

Acknowledgments

I would like to express my heartfelt thanks to my supervisor Prof. Dr Horst-Dieter Försterling for his very effective guidance and instructions in this work. I am especially grateful to him for his kind help during my three-year stay in Marburg.

I would like to thank Prof. Dr Zoltán Noszticzius (Department of Chemical Physics and Center for Complex and Nonlinear Systems, Technical University Budapest, Hungary) for starting me on this research field, for his fruitful suggestions, constructive ideas and for all the common research during his stays in Marburg. Moreover, I am very grateful for the correction and critical reading of the manuscript.

I extend my special thanks to Dr. Helmut Schreiber for the valuable discussions and insightful comments. I also appreciate my colleagues Ms Atchara Sirimungkala and Mrs Julia Oslonowitsch for their kind help in the kinetics experiments. Mrs Athena Knoll, Mr. Uwe Capeller, Mr. Manfred Graf, Mr. Werner Kröschel, and Mr. Julius Klaus are thanked for their helpful assistance in the laboratory.

I gratefully acknowledge the financial support by the Deutsche Forschungsgemeinschaft.

Attila Lázár
Marburg, Germany, March 1997

Lebenslauf

07. Juni 1970 geboren als Sohn von Éva Lázár, geb. Bóta und Attila Lázár in Győr, Ungarn
- 1976-1984 Grundschule Radnóti Miklós, Győr
- 1984-1988 Gymnasium Révai Miklós, Győr
- Juni 1988 Allgemeine Hochschulreife
- 1988-1989 Wehrdienst
- 1989-1994 Studium der Chemie an der Technischen Universität Budapest
- Januar-Mai 1992 Vordiplomarbeit am VISCOSA AG. in Nyergesújfalu bei Herrn Dr. L. Meiszel; Thema: "Herstellung von Ultrafiltrationsmembranen aus Polyacrylnitril"
- Juli 1992 Diplom-Vorprüfung, Ingenieur
- Sept. 1993-Mai 1994 Diplomarbeit an der Technischen Universität Budapest bei Herrn Prof. Dr. Z. Noszticzius; Thema: "Chemische Wellen in modifizierten Membranen"
- Juni 1994 Diplom-Hauptprüfung, Diplom-Ingenieur
- September 1994 Beginn der Doktorarbeit am Fachbereich Physikalische Chemie der Philipps-Universität in Marburg bei Herrn Prof. Dr. H-D. Försterling
- seit Oktober 1994 Wissenschaftlicher Angestellter am Fachbereich Physikalische Chemie, finanziert von der Deutschen Forschungsgemeinschaft.